COLOR TUNABLE AND ENERGY TRANSFER STUDIES IN SINGLE PHASE RARE EARTH DOPED CALCIUM BISMUTH ORTHOPHOSPHATE PHOSPHOR FOR ENERGY EFFICIENT OPTOELECTRONIC APPLICATIONS

Thesis

Submitted to

Delhi Technological University

in partial fulfillment of the requirement for the degree of

DOCTOR OF PHILOSOPHY

in

ENGINEERING PHYSICS

by

MUKESH KUMAR SAHU

(Reg. No. 2K17/Ph.D./AP/10)

Under the Supervision of

Dr. M. JAYASIMHADRI

DEPARTMENT OF APPLIED PHYSICS

DELHI TECHNOLOGICAL UNIVERSITY

BAWANA ROAD, DELHI-110 042, INDIA

APRIL-2023

DEDICATED TO….
MY FAMILY

Delhi Technological University

(Govt. of National Capital Territory of Delhi)
Bawana Road, Delhi-110042

CERTIFICATE

This is to certify that the thesis titled "***Color Tunable and Energy Transfer Studies in Single Phase Rare Earth Doped Calcium Bismuth Orthophosphate Phosphor for Energy Efficient Optoelectronic Applications***" is being submitted by ***Mr. Mukesh Kumar Sahu*** with registration number ***2K17/Ph.D./AP/10*** to the Delhi Technological University for the award of the degree of Doctor of Philosophy in the discipline of ***Engineering Physics***. The work embodied in this thesis is a record of bonafide research work carried out by me in the Department of Applied Physics, Delhi Technological University, Delhi under the supervision of ***Dr. M. Jayasimhadri***. It is further certified that the work embodied in this thesis has neither been partially nor fully submitted to any other university or institution for the award of any degree or diploma.

Mukesh Kumar Sahu
(Reg. No. 2K17/Ph.D./AP/10)

This is to certify that the above statement made by the candidate is correct to the best of our knowledge.

Dr. M. Jayasimhadri
Supervisor & Assistant Professor
Department of Applied Physics
Delhi Technological University
Delhi-110 042, India

Prof. A. S. Rao
Head,
Department of Applied Physics
Delhi Technological University
Delhi-110 042, India

ACKNOWLEDGEMENTS

The journey of my research is accomplished with the valuable support of many people. It is a pleasing part that I have now the opportunity to express my gratitude for all of them.

At the outset, I would like to express my profound sense of gratitude, indebtedness and reverence to my supervisor, ***Dr. M. Jayasimhadri****, Department of Applied Physics, Delhi Technological University (DTU), Delhi, who nurtured my research capabilities for a successful scientific career. It has been an honour to work under excellent, enthusiastic and distinguished supervisor. His incessant encouragement, constant help, meticulous supervision and constructive criticism throughout the course of my study for carving another milestone in my academic journey. His massive knowledge of the subject, systematic gaze and perseverance were a constant source of inspiration during this thesis work.*

I further stand ovate to ***Prof. A. S. Rao****, Head, Department of Applied Physics, DTU, for his timely advice, valuable help, suggestions and support. My deepest recognitions for* ***Prof. Suresh C. Sharma****, former Dean (Academic PG) DTU,* ***Prof. Rinku Sharma,*** *Dean (Academic PG) DTU and my SRC & DRC committee members for their enduring support.*

I express my sincere gratitude to ***Prof. D. Haranath****, National Institute of Technology, Warangal,* ***Dr. J. Suresh Kumar****, University of Aveiro, Portugal for availing the lab equipment and their continuous support. My deepest regards to* ***Dr. Anil Kumar****, Deputy Registrar, DTU. It is my pleasure to express my sincere thanks to all the faculty members of DTU. I am also grateful to* ***Advanced Instrumentation Centre****, technical staff for their timely support and cooperation whenever required.*

I sincerely thank my dear former and present lab mates whose support helped in accomplishing my work. It is my pleasure to thank my seniors ***Dr. Amit K. Vishwakarma, Dr. Kaushal Jha, Dr. Sumandeep Kaur, Dr. Harpreet Kaur*** *and present lab mates* ***Ms.***

Deepali, Mr. Vikas, Mr. Indrajeet Maurya, Ms. Vertika Siwach *for their support. It's my pleasure to thank my seniors* ***Dr. Vinay Kumar, Dr. Nisha Deopa.*** *I would like to thank* ***Mr. Mohit Tyagi****,* ***Mr. Rajat Bajaj*** *and lab members from MASR lab. I wish to acknowledge the enjoyable company and suitable help rendered by my dear friends****, Dr. Mrityunjay Kumar Singh, Dr. Prateek Sharma Ms. Suman Dahiya, Ms. Ritika Khatri, Ms. Ritika Ranga, Mr. Abhishek Bhardwaj, Dr. Vineet Sharma and Mr. Gaurav*** *for their help and support during this tenure. I would also like to thank all the other research scholars of DTU, Delhi for their help and advice. I wish to acknowledge the gratifying company and suitable help by* ***Dr. Savvi Mishra****,* ***Dr. Swati Bishnoi, Dr. G. Swati*** *and* ***Dr. Vishnu Vikesh Jaiswal*** *during this tenure.*

Finally, I thank my family for their support and motivation, at every moment of my research period. With heartful gratitude and love, I express my gratefulness to my father ***Shri Babulal Sahu*** *and mother* ***Smt. Shakuntla Sahu*** *for their continual love and encouragement over the entire course of my life. I am thankful to my loving wife* ***Mrs. Priyanka Sahu*** *for the valuable suggestions, care, love and faith in me throughout my existence. I am thankful to my Mausi* ***Ms. Ambika Sahu****, younger brother* ***Mr. Rajesh Sahu*** *and family members for helping me maintain a positive attitude throughout my studies.*

I gratefully acknowledge the financial assistance provided by ***SERB-DST*** *project (No. SB/FTP/PS-082/2014), dt. 02/03/2015,* ***DTU*** *and* ***CSIR*** *in the form of JRF and SRF during the period of my research. I extend my gratitude to DTU and staff in Administration, Accounts, Store & Purchase, Library and Computer Centre for their help and services.*

I thank one and all for helping me to accomplish the successful realization of the thesis.

Thank you all!!! ***(Mukesh Kumar Sahu)***

LIST OF PUBLICATIONS

1. **Mukesh K. Sahu**, M. Jayasimhadri "Conversion of blue emitting thermally stable $Ca_3Bi(PO_4)_3$ host as a color tunable phosphor via energy transfer for luminescent devices" ***Journal of Luminescence*** 227 (2020) 117570. ***(IF: .3.6)***
2. **Mukesh K. Sahu,** M. Jayasimhadri "White light emitting thermally stable bismuth phosphate phosphor $Ca_3Bi(PO_4)_3:Dy^{3+}$ for solid-state lighting applications" ***Journal of the American Ceramic Society*** 102 (2019) 6087-6099. ***(IF: 4.186)***
3. **Mukesh K Sahu**, M Jayasimhadri "Structural and color tunable properties in Sm^{3+}/Eu^{3+}-doped $Ca_3Bi(PO_4)_3$ phosphor for solar cell and w-LED applications" ***Journal of Materials Science: Materials in Electronics*** 33 (2022) 5201-5213. ***(IF: 2.8)***
4. **Mukesh K Sahu**, M Jayasimhadri, D. Haranath "Temperature-dependent photoluminescence and optical thermometry performance in $Ca_3Bi(PO_4)_3:Er^{3+}$ phosphors " ***Solid State Sciences*** 131 (2022) 106956. ***(IF: 3.5)***

Not Included in thesis

1. B.V. Ratnam, **Mukesh K. Sahu**, Amit K. Vishwakarma, Kaushal Jha, Hyun-Joo Woo, Kiwan Jang, M. Jayasimhadri, **"**Optimization of synthesis technique and luminescent properties in Eu^{3+}-activated $NaCaPO_4$ phosphor for solid state lighting applications" ***Journal of Luminescence*** 185 (2017) 99-105. ***(IF: 3.6)***
2. Swati Bishnoi, G. Swati, Paramjeet Singh, V. V. Jaiswal**, Mukesh K. Sahu**, Vinay Gupta, N. Vijayan and D. Haranath "Appearance of efficient luminescence energy transfer in doped orthovanadate nanocrystals" ***Journal of Applied Crystallography*** 50(3) (2017) 787-794**.** ***(IF: 6.1)***
3. **Mukesh K. Sahu**, M. Jayasimhadri, Kaushal Jha, B. Sivaiah, A.S. Rao, D. Haranath "Synthesis and enhancement of photoluminescent properties in spherical shaped Sm^{3+}/Eu^{3+} co-doped $NaCaPO_4$ phosphor particles for w-LEDs" ***Journal of Luminescence*** 202 (2018) 475–483. ***(IF: 3.6)***
4. **Mukesh K. Sahu,** Harpreet Kaur, B.V. Ratnam, J. Suresh Kumar, M. Jayasimhadri "Structural and spectroscopic characteristics of thermally stable Eu^{3+} activated barium zinc orthophosphate phosphor for white LEDs" ***Ceramics International,*** 46 (2020) 26410-

26415. ***(IF: 5.2)***

5. Harpreet Kaur, M. Jayasimhadri, **Mukesh K. Sahu**, P. Koteswara Rao, N.S. Reddy, "Synthesis of orange emitting Sm^{3+} doped sodium calcium silicate phosphor by sol-gel method for photonic device applications" ***Ceramics International,*** 46 (2020) 26434-26439. ***(IF: 5.2)***
6. Rakshit Jain, Rachna Sinha, **Mukesh K. Sahu**, M. Jayasimhadri, "Synthesis and optimization of photoluminescence properties in potential reddish orange emitting niobate phosphor for photonic device applications" ***Luminescence*** 36 (6) (2021) 1444-1451. ***(IF: 2.6)***
7. Dipti Bidwai, Yatish R Parauha, **Mukesh K Sahu**, Sanjay J Dhoble, M Jayasimhadri, G Swati, "Synthesis and luminescence characterization of aqueous stable $Sr_3MgSi_2O_8$: Eu^{2+}, Dy^{3+} long afterglow nanophosphor for low light illumination" ***Journal of Solid-State Chemistry***, 310 (2022) 123089. ***(IF: 3.3)***
8. **Mukesh K. Sahu**, S Bishnoi, G Swati, M Jayasimhadri, D Haranath "Thermally stable Mn^{2+} activated zinc silicate nanophosphor for speedy recognition of high contrast latent fingermarks" ***International Journal of Applied Ceramic Technology*** 19 (2022) 488-497 ***(IF: 2.3)***

RESEARCH WORK PRESENTED AT CONFERENCES

1. **Mukesh K. Sahu**, M. Jayasimhadri *"**Structural and spectroscopic studies of rare earth free deep red emitting lithium aluminate phosphor for optoelectronic applications**"* presented in International Conference on Atomic, Molecular, Optical & Nano Physics with Applications **(CAMNP-2019)** at Delhi Technological University Delhi, during 18-20th December 2019.
2. **Mukesh K. Sahu**, M. Jayasimhadri "***Structural and spectroscopic properties of thermally stable Eu^{3+} doped barium zinc orthophosphate phosphor for w-LEDs"*** presented in 8th International Workshop on Photoluminescence in Rare Earths: Photonic Materials and Devices **(PRE-2019)** at Université Côte d'Azur, CNRS, Nice, France during 4th – 6th September 2019.
3. **Mukesh K. Sahu**, M. Jayasimhadri "***Synthesis and photoluminescence properties of Dy^{3+} doped pyro-phosphate phosphor for white LEDs**"* presented in International Conference on Luminescence and its Applications **(ICLA-2019)** at Pt. Ravishankar Shukla University, Raipur, during 07th- 10th January 2019.
4. **Mukesh K. Sahu**, M. Jayasimhadri "***Synthesis and photoluminescent studies of Eu^{3+} activated $Ca_3Bi(PO_4)_3$ phosphors for white LEDs**"* presented in National Conference on Luminescence and its Applications **(NCLA-2018)** at National Institute for Interdisciplinary Science and Technology, Trivandrum, during 14th- 16th February 2018.
5. **Mukesh K. Sahu**, M. Jayasimhadri *"**Intense white light emission from Dy^{3+}doped $Ca_3Bi(PO_4)_3$ phosphor for w-LEDs application**"* presented in International Conference on Advanced Production and Industrial Engineering **(ICAPIE-2017)** at Delhi Technological University Delhi, during 6th-7th October 2017.

ABSTRACT

COLOR TUNABLE AND ENERGY TRANSFER STUDIES IN SINGLE PHASE RARE EARTH DOPED CALCIUM BISMUTH ORTHOPHOSPHATE PHOSPHOR FOR ENERGY EFFICIENT OPTOELECTRONIC APPLICATIONS

In the current scenario, successively increasing global electricity demand, consumption and energy saving strategies are prime subjects captivating ample attention. This electricity demand and consumption can resolve by opting two practical approaches, i.e., by energy-saving strategy and enhancing the power generation efficiency of green renewable energy sources. One of the important practical approaches is advanced artificial lighting sources based on phosphor-converted white light emitting diodes (pc-WLEDs), which reduce the world's energy consumption. The pc-WLEDs have been considered as a next-generation indoor and outdoor light sources. All over the place around the globe, artificial lighting has inclusive influences on environmental surroundings, biotic societies, and human development as they have superior advantages such as high efficiency, environmental friendly, huge amount of energy saving, compact size as compared to fluorescent and outdoor illumination devices. The second practical approach is solar cells, one of the potential green renewable technologies to accomplish the worldwide energy crises, which could possibly reduce the dependency on traditional fossil fuel-based power generation. As the solar spectrum is an abundant and valuable green renewable energy resource that is freely accessible in every part of the earth.

These two practical approaches have some shortcomings such as commercially available pc-WLEDs illuminate the bluish-white light with high correlated color temperature due to the deficiency of the red color component with less thermal stability and the silicon-based solar cell operated with limited conversion efficiency as most of the spectrum was unexploited, i.e., spectral mismatch. Several scientists and researchers have been

uninterruptedly working on this area and try to formulate methods to overcome the shortcomings in pc-WLEDs and enhance solar cell energy conversion efficiency by utilizing the unused part of the solar spectrum. The commercially available sulfide and nitride-based near-ultraviolet/blue pumped red phosphors have some disadvantages, such as low chemical stability and efficiency compared with other primary colors. Furthermore, phosphors used in lighting devices require high thermal stability as the UV/blue LED chips generate temperature around 120 to 150 °C while operating time, which affects the luminescent properties of phosphor and degrades emission intensity as well as the performance of the pc-WLEDs.

Phosphors based devices have emerged as an alternative to conventional energy sources. They offer to save huge amounts of electrical energy and reduce carbon emissions globally. Furthermore, phosphors have been found in an extensive range of applications in our daily life, including solid-state lighting, advanced optical displays, optical waveguides, solar cells and many more. As a result, tremendous effort has been made to date to investigate novel phosphor materials. The desire for new phosphor materials has driven scientific and technological attempts to enhance luminous materials' current properties. The current research work is mainly focused on the color tunable and energy transfer studies in single-phase rare earth-doped calcium bismuth orthophosphate phosphor for energy-efficient optoelectronic applications. Rare earth-doped orthophosphate phosphors have attracted much attention for light emitting diode and display applications. The eulytite type orthophosphate with the general formula $A_3B(PO_4)_3$ (A = divalent alkaline earth & B = trivalent Bi or RE ion) has gained attention due to their excellent optical, magnetic, and dielectric property, along with thermal and chemical stability. Among all the eulytite structures, calcium-based eulytite type orthophosphate [$Ca_3Bi(PO_4)_3$] phosphor can be synthesized at a moderate temperature. Eulytite-type materials doped with rare earth ion exhibit promising luminescence properties due to the disordered

structure. Based on the literature survey, it was recognized that eulytite-type materials may perform as significant host matrices for efficient optoelectronic applications.

The current research work has been deeply focused on the synthesis of strategic luminescent materials to explore their morphology, structural optical characterizations and enhancement of luminescent properties for optoelectronic applications. Therefore, the main objectives of the present proposal are to produce the most efficient phosphor with improved luminescent properties by scaling up the process for comfortable industrial acclimatization. The results of the research effort have been divided into seven chapters in order to achieve the research goals of the current work. Here is a quick overview of each chapter:

Research usually initiates with self-motivation and recognition of a contemporary problem and then followed by strategies to perform and prove the methodology for resolving it. Here, **chapter 1** states the motivation, outline of the problem, literature survey and origin of research objectives for the development of efficient visible light emitting phosphors. It includes the basics of photoluminescence and comprehensive studies about luminescent crystalline materials (phosphors). Furthermore, the role of phosphor in the advancement of smart optoelectronic devices has been discussed. Finally, every step to accomplish the present research work, such as the selection of the host material ($Ca_3Bi(PO_4)_3$), activator, sensitizer and optimization of emission and thermal stability for direct utility in a variety of optoelectronic devices such as lighting, solar cell and optical sensors have been included in this chapter.

Chapter 2 focuses on the experimental work and characterization techniques required for the preparation of an efficient phosphor with excellent PL characteristics. The preparation of efficient multifunctional material needs appropriate acquaintance of numerous synthesis procedures along with the proper characterization techniques for the potential utility of the selected RE ions activated $Ca_3Bi(PO_4)_3$ phosphor in optoelectronic devices. The characteristics

of RE ions doped phosphors were scrutinized by employing the numerous characterization techniques used to explore their structural, vibrational, morphological and spectroscopic characteristics for their utility in advanced optoelectronic devices. To understand the instruments better, working principles, device descriptions, and operational controls of characterization tools used in the present research work are described in the current chapter.

Chapter 3 covers the luminescence properties of eulytite-type crystalline structure of Eu^{3+} activated $Ca_3Bi(PO_4)_3$ phosphors synthesized via a solid-state reaction method in an ambient atmosphere. The diffraction pattern of the synthesized phosphor confirmed the formation of pure and single-phase crystalline with a cubic structure of $Ca_3Bi(PO_4)_3$ microparticles. The SEM image of $Ca_3Bi(PO_4)_3$ illustrates the growth of heterogeneous microstructures with some agglomeration. The $Ca_3Bi(PO_4)_3$ host shows the broad emission peak at 434 nm (blue region) under the excitation wavelength of 326 nm ascribing to $^3P_1 \rightarrow {}^1S_0$ electronic transition of Bi^{3+} ions. The Eu^{3+} activated $Ca_3Bi(PO_4)_3$ phosphors exhibit an intense red emission band centered at λ_{em} = 612 nm ($^5D_0 \rightarrow {}^7F_2$) at excitation wavelengths of 393 & 465 nm and perceived that the optimized Eu^{3+} ion concentration is 8.0 mol%. The host blue emission intensity diminished with increasing Eu^{3+} engagement, whereas the intensity enhanced for the characteristic peaks of Eu^{3+} ions are located in the 550-725 nm range under the host excitation wavelength (λ_{ex} = 326 nm). This suggests that part of the host emission energy was transferred to the activator when the host was doped with Eu^{3+} activator ions. The CIE color coordinates for the $Ca_3Bi(PO_4)_3$ host lie in the blue region, which has been modulated towards the red part with increasing Eu^{3+} ions concentration. However, the CIE coordinate values for Eu^{3+} doped $Ca_3Bi(PO_4)_3$ phosphor fall in the red region at λ_{ex} = 393 & 465 nm with high color purity. The average decay time of the optimized phosphor was in the range of milliseconds at λ_{ex} = 393 nm λ_{em} = 612 nm. The PL intensity persists up to 75.45% at 200 °C of ambient temperature,

assuring the excellent thermal stability of phosphor. The combination of the above-revealed results recommends that $Ca_3Bi(PO_4)_3$: Eu^{3+} phosphor can be a probable contestant in near-UV/blue excited luminescent devices. [Part of this work has been published in the ***Journal of Luminescence*** 227 (2020) 117570] **(IF: 3.6)**

Chapter 4 depicts the structural, vibrational, morphological luminescent properties of white light emitting dysprosium doped $Ca_3Bi(PO_4)_3$ phosphor for solid-state lighting applications. The X-ray diffraction (XRD) and structural refinement studies reveal that the synthesized phosphors consist of a single phase with a cubic structure. The field emission scanning electron microscopy images reveal that the as-synthesized phosphor has a micron size with an irregular shape. Under near ultraviolet (n-UV) and blue excitation, the phosphor exhibits white light emission via a combination of blue (~451 nm) and yellow (~575 nm) emission bands. The optimized concentration of Dy^{3+} ions is 6.0 mol%, after which the concertation quenching occurs. The energy transfer process between Dy^{3+} ions is due to dipole-dipole interaction, which was confirmed by applying Dexter and Reisfeld's Energy Transfer (ET) formula. The CIE chromaticity coordinates for the optimized phosphor were (0.329, 0.377), which lie in the white light region. The emission intensity remains at 83.41% at 373 K to that at room temperature, which indicates good thermal stability. The results mentioned above demonstrate that $Ca_3Bi(PO_4)_3$ is a potential phosphor for solid-state lighting applications. [Part of this work has been published in the ***Journal of the American Ceramic Society*** 102 (2019) 6087-6099] **(IF: 4.186)**

Chapter 5 describes about the numerous characteristics of eulytite type $Ca_3Bi(PO_4)_3$ (CBP) phosphors activated with Sm^{3+} and co-activated with Sm^{3+} & Eu^{3+} ions for solar cell, pc-w-LEDs and photonic devices. Phase and crystal structure have been recognized using X-ray diffraction analysis and Rietveld refinement. The Sm^{3+} doped CBP phosphor exhibit three

emission peaks at 562, 598 and 644 nm under 400 nm excitation and the highest emission intensity has been observed for 5.0 mol% Sm^{3+} doped CBP phosphor. The co-doping of Sm^{3+} and Eu^{3+} ions in CBP phosphor has expanded the excitation as well as emission spectra. The ET between sensitizer ions (Sm^{3+}) to activator ions (Eu^{3+}) in CBP phosphor has been studied based on the photoluminescence (PL) and decay curves using the Dexter ET formula and Reisfeld's theory. The PL quantum yield was obtained as high as 86.64%, indicating a potential red constituent to use in photonic devices. The CBP:Sm^{3+}/Eu^{3+} emission intensity persisted at 81.27% at 150 °C compared to the emission intensity at room temperature, confirming the excellent thermal stability. Moreover, the color coordinates and decay curves have enhanced the suitability of CBP:Sm^{3+}, Eu^{3+} for accomplishing spectral conversion in solar cells, pc-w-LEDs and other photonic devices. [Part of this work has been published in the ***Journal of Materials Science: Materials in Electronics***, 33 (2022) 5201-5213] **(IF: 2.8)**

Chapter 6 focuses on the structural, optical, morphological, luminescent characteristics of the CBP:Er^{3+} phosphors for optical thermometry and optoelectronic applications. The diffraction patterns of the samples are matched well with the standard data of single-phase cubic CBP structure and did not change after doping. The reflectance spectrum shows the various absorption peaks owing to Er^{3+} ions. The field emission scanning electron microscopy images disclose that the sample particles have asymmetrical spherical particles with some aggregation. Elemental analysis and mapping confirm the existence of various compositional elements. The PL spectra specify that the phosphor can be effectively excited by near-ultraviolet (n-UV) LED, which was well-observed from the excitation spectrum. As synthesized phosphor emits the visible emission at 523 ($^2H_{11/2} \rightarrow {}^4I_{15/2}$), 552 ($^4S_{3/2} \rightarrow {}^4I_{15/2}$) and 662 nm ($^4F_{9/2} \rightarrow {}^4I_{15/2}$) under n-UV excitation (376 nm). The calculated color coordinates reveal the green emission from the phosphor under 376 nm excitation with high purity. PL variation and fluorescence intensity

ratio from the thermally coupled $^4S_{3/2}$ and $^2H_{11/2}$ levels of Er^{3+} ions can be utilized to explore applications in optical thermometry and found good thermal sensitivity in the range of 300-473 K. Hence, the mentioned structural and optical characteristics of the prepared CBP: *x*Er^{3+} phosphors will find fascinating applicability in optical thermometry and other optoelectronic devices. [Part of this work has been published in ***Solid State Sciences***, 131 (2022) 106956] **(IF: 3.5)**

Chapter 7 summarizes the outcomes of all the working research chapters from 3 to 6. The revolutionary scope of the research work has also been explained based on the probable optoelectronic device applications of these phosphors in numerous fields of science and technology.

LIST OF FIGURES

LIST OF TABLES

TABLE OF CONTENTS

Table of content **Page number**

CHAPTER 1

Introduction and Motivation of the Research Work

Research usually initiates with self-motivation, recognition of a contemporary problem and then followed by strategies to perform and prove the methodology for resolving it. The present chapter focused on the motivation, outline of the problem, literature survey, and systematic research work to develop efficient visible light emitting phosphors for optoelectronic applications. It includes the basics of photoluminescence, comprehensive studies about luminescent crystalline materials (phosphors) and appropriate activator ions. Furthermore, the role of phosphor in the advancement of smart optoelectronic devices has been discussed. The significance of particular $Ca_3Bi(PO_4)_3$ host material is also indicated in this chapter. Finally, every step to accomplish the research work, such as selection of the activator and sensitizer and optimization of emission and thermal stability for direct utility in a variety of optoelectronic devices such as WLED, solar cells and optical sensors have been contained within this section.

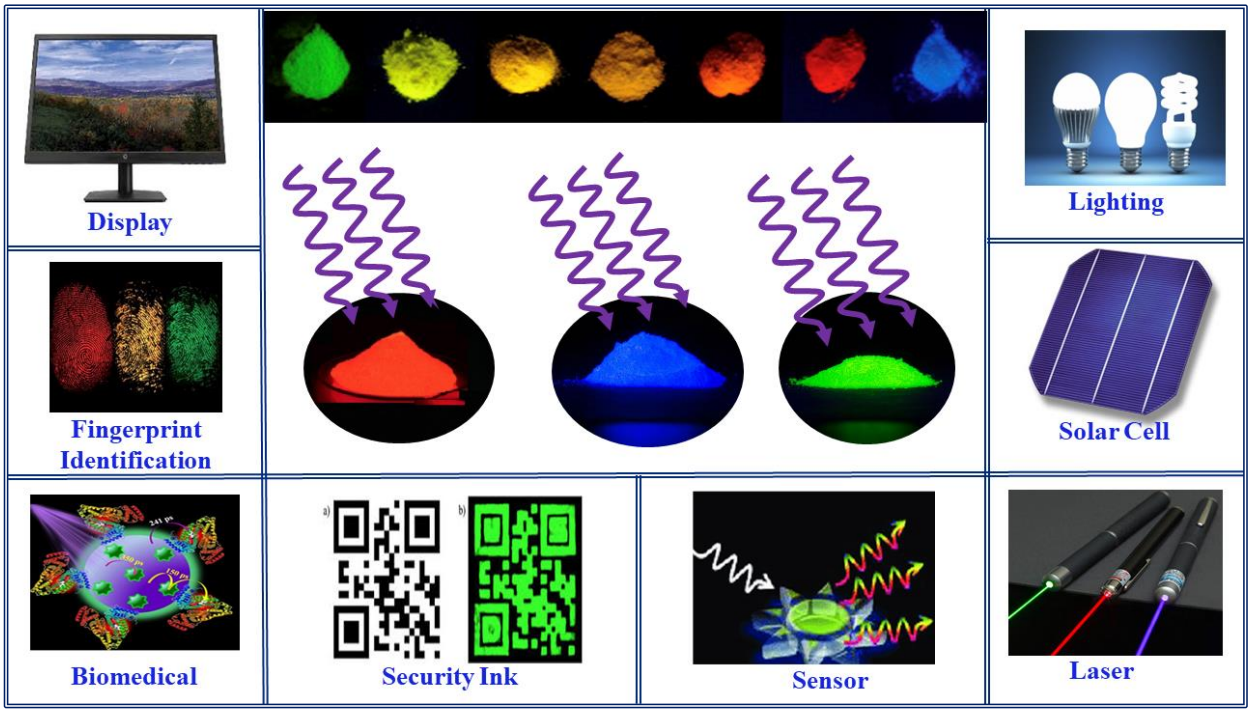

1.1. Introduction and Motivation

Energy plays a vital role in any country's technological, social and economic development. Worldwide, the energy demand has enlarged swiftly in current times, owing to the ever-growing population and people yearning for a luxurious life [1–3]. Energy demand is the term used to designate the energy consumption by human activity. The Indian government has made outstanding strides toward granting hundreds of millions of its citizen's accesses to power connections. Since 2000, energy consumption has doubled, and primary sources based on fossil fuels like coal, oil, and gas still provide 80% of the energy needed to meet demand [4]. Approximately, all power generation methods can affect the environment and the impact will be depend on how and where the electricity is generated and distributed. The burn fossil fuels are one of the critical sources of greenhouse gases and also increases the atmospheric temperature [5,6]. Due to increment in atmospheric temperature, biological, physical, ecosystems will affect and causes the extinction of species along with adversely effect on everyone's health [1,7,8]. Hence, many scientists and researchers have been working on energy-efficient technologies, which can reduce dependence on fossil resources and also to decrease energy consumption.

The rapidly increasing demand for energy can resolve by choosing powerful strategies, i.e., energy saving approach and retaining green renewable power generation techniques. There are three energy saving approaches such as: (i) energy saving by technology (ii) energy saving by management, (iii) energy saving by policies/regulations [9]. Advanced energy saving technologies have tremendous potential to save an enormous amount of energy worldwide. One of the advanced energy saving technology is solid-state lighting (SSL) devices. SSL devices are used in every area to illuminate indoors as well as outdoors from industries to domestic

fields. As lighting alone consumes more than 20% of total energy demand [10]. In recent times, SSL productions perceived tremendous progression due to the fact that this technology can diminish the electricity used for lighting by more than 33% in the upcoming decades [11]. It is owing to the exceptional features of SSL devices, which is a phosphor-converted white light emitting diodes (w-LEDs). Phosphor-converted w-LEDs have exceptional features such as huge amount of energy saving, environment friendly, longer lifetime, highly reliable, and less manufacturing charges when compared with fluorescent/incandescent lamps [12–15]. In the current scenario, there are numerous approaches to acquire the white light. Currently, the adopted and most utilized approach contains a blue emitting InGaN chip as a source of excitation and coated over YAG: Ce^{3+} yellow emitting phosphor with organic binder [16–18]. But the above-mentioned approach has shortcomings like low color rendering index, halo effect and high correlated color temperature owing to the deficiency of red emitting constituent [19–21]. Another way to generate white light is the combination of ultraviolet (UV) /near-UV chip coated with mixer of red, green and blue (RGB) emitting luminescent materials [13,22]. This approach offers improved CRI and appropriate CCT, but upsurges the preparation duration and production cost. Additionally, this technique has also some downsides such as poor RGB color mixing, reabsorption of blue light by green and red emitting luminescent materials, phase separation and low color stability attributed to the different color emitting luminescent materials [23–25]. Therefore, white light emission from a single-phase phosphor has gained momentous consideration compared to RGB emitting luminescent materials [26–28].

Second powerful strategy is the green renewable power generation techniques, which can reduce dependency on fossil based resources simultaneously lessening emission of greenhouse gases and their effects. As a point of interest, green renewable power generation

technology is solar cells, which can be considered as a potential approach to fulfill the demand of household and industry [29,30]. Solar energy harvesting is a promising and clean source of energy generation, which can reduce the use of traditional polluting technology for energy generation, such as coal power and oil-based plants. A solar cell can be able to convert solar radiation into electrical energy, which is probable, auspicious tactics for renewable energy and has already been an enormous consideration of numerous scientific as well as industrial groups [2]. The sun's UV to IR (280–2500 nm) energy touches the surface of the Earth. Yet, only a small fraction of the solar spectrum is converted into electrical energy by crystalline silicon solar cells. The single junction silicon solar cell typically has a bandgap of 1.1 eV and a 30% efficiency. While a spectral mismatch between the solar cell response and sun spectrum is responsible for 70% of energy losses [2]. Therefore, one of the big challenges for researchers is, how to boost the efficiency of existing C-Si solar cell?

Many researchers have uninterruptedly worked and formulated many approaches, which can boost energy conversion efficiency of solar cell by employing the unexploited fragment of the solar radiation [31–34]. An important strategy is the luminous material coating on the upper and lower substrate of the solar cell, which can improve the efficiency of energy conversion. The solar cell upper/lower substrate can be directly coated with n-UV pumped effective green to red emitting phosphor, which increases the efficiency of solar radiation conversion. Such phosphor is considered as a potential candidate to resolve the spectral mismatch issue and also to enhance the efficiency of existing C-Si solar cell. Further, luminescent materials can be appropriate in an extensive range of applications such as efficient lighting devices including advanced optical displays, sensors, lasers and many more. Therefore, massive efforts have been enthusiastic for exploring an efficient luminescent material so far.

Luminescent materials have been appeared as an alternative to conventional energy sources and directly applicable in many fields. They offer to save enormous amounts of electrical energy and diminishes the carbon emissions, globally [11,22]. Also, the luminescent materials are essential for commercially used phosphor-converted w-LEDs, which can overcome the inadequacies such as halo effect, less thermal stability, deficiency of color rendering index (R_a< 65~70) and inappropriate correlated color temperature [35–38]. Therefore, it is very essential to synthesize an efficient n-UV/blue light excitable red emitting, chemically stable and environmental friendly single-phase phosphor, which can be used effectively in advanced solar cell and w-LEDs [39–42]. Also, luminescent materials have found an extensive range of applications in day-to-day life, including advanced optical displays, scintillation, bioimaging, sensing, security ink and many more. The unique characteristics and extensive range of utilities recommend impactful research to be carried out for the application of luminescent materials in the field of optoelectronics especially light emitting devices and solar cells.

1.2. Luminescence

The Latin word "lumen," which meaning "light," is the root of the "luminescence." In the year 1888, one of the historians and physicist Eilhardt Wiedemann has first thought up the word as luminescenz [43]. Emitting electromagnetic radiation by luminescent material is known as luminescence. Luminescent material can absorb the specific invisible radiation or external energy and give emission preferably in the visible or near infrared red (NIR) regions. Luminescence is often considered as cold body radiation as compared to the incandescence process, which gives the hot light. Luminescence is one of the common phenomena in day-to-day lives, for instance, the numerous fluorescent lightings, television/display devices and many

more. There are several ways to excite materials and depending on the excitation source it can be classified into different types as illustrated in table 1.1.

Table 1.1: The types of luminescence, their excitation source and applications.

Classification	**Excitation Source**	**Applications**
Photoluminescence (PL)	Photon	➢ Lighting sources ➢ Solar cells ➢ Display devices ➢ Lasers ➢ Sensors ➢ Highlighting paints ➢ Security ink
Electroluminescent (EL)	Electric field	➢ LEDs ➢ Laser diodes ➢ EL displays ➢ EL sensors
Thermoluminescence (TL)	Heat	➢ Environmental monitoring ➢ Geological dating ➢ Dosimetry of ionizing radiation
Chemiluminescence	Chemical reaction	➢ Chemical analysis
Cathodoluminescence	Electron beam	➢ Cathode ray oscilloscope ➢ TV screen ➢ Field emission display
Bioluminescence	Bio-chemical reaction	➢ Analytical chemistry
Radioluminescence	X-rays	➢ X-ray display ➢ X-ray scintillators

Among above mentioned various classifications of luminescence, the prime focus of current thesis/research work is based on the photoluminescence mechanism.

1.2.1. Photoluminescence (PL)

The phenomena which involve the emission of light from the luminescent materials after absorption of particular photons is usually recognized as photoluminescence. Incident photon on the luminescent materials, gives the energy to electrons within the material. Subsequently the electron transfers from ground to the permissible excited sate. After that the excited electrons come back to their lower energy and the part of energy is released in the form of non-radiative (lattice vibrations of solid, phonon) as well as radiative emission [44]. The released energy of non-radiative and radiative light was analogous with the energy variance between transition states involved in the process. Based on immediate and delayed emission process, the PL is categorized into fluorescence and phosphorescence [45].

(a) Fluorescence

In this category of PL, the emission takes place in a very minute time span (within 10^{-8} s) after removal of excitation source. Emission of visible light in a very fast manner as the excited ions returns to lowest excited state and finally to the specific ground state.

(b) Phosphorescence

In this PL process, delayed emission takes place after removing the source of excitation and emission keep on continuing for an extensive interval from milliseconds to ~10 seconds to several hours also known as afterglow luminescence [45]. The excited ions return to the ground state slowly as the phosphorescence materials glow for extended periods of time. In phosphorescence, material after absorbing excitation energy, ions reach excited state having dissimilar spin, returned after sometimes to the ground state and gives the radiative emission.

1.2.2. PL processes

(i) ***Absorption:*** When a particular radiation incident on the materials and part of the radiation is taken by the ions in a material, it is known as absorption as presented in Fig. 1.01 (a). Absorption is a process by which ions soak up the part of radiation in the ground energy level to reach higher energy level. Owing to absorption, the incident radiation is attenuated after passing through a material [46].

(ii) ***Excitation:*** A part of the absorbed radiation by ions can stimulate to move them from the ground energy level to the higher energy levels named as excitation in Fig. 1.01 (b). Thus, excitation is the addition of the part of energy to an ions, that results in its alteration, ordinarily from the ground state to one of the excited state [47].

(iii) ***Non-radiative relaxation:*** When a stimulated ion at a higher excited state moves towards the lower excited state and releases very trivial amounts of energy through molecular vibrations or atomic collisions is acknowledged as non-radiative relaxation process as illustrated in Fig. 1.01 (c). Non-radiative, radiative, or a combination of the two processes may be used in the relaxation to the ground state. A phonon (heat or lattice vibration) results from the nonradiative process [46].

(iv) ***Emission:*** It is a spontaneous transition of stimulated electron from lowest excited state to certain lower energy levels that resulted in releasing of photons equivalent with the energy difference between the involved energy levels can be pronounced as emission or radiative transitions as established in Fig. 1.01 (d) [44].

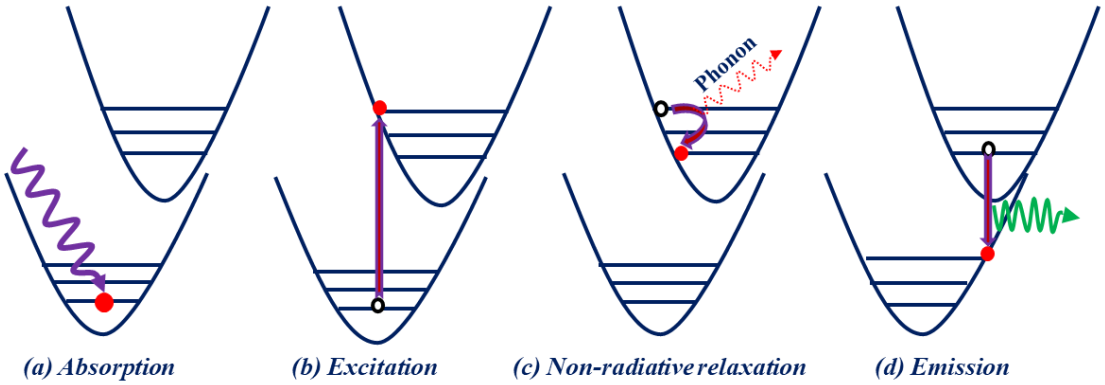

Fig.1.01: *PL processes: (a) absorption, (b) excitation, (c) non-radiative relaxation and (d) emission.*

1.2.3. Phosphor

Phosphors exhibit luminescence characteristics and are termed as luminescent materials. Phosphor is a special kind of material which emit light preferably in UV, visible or infrared region, when excited by any kind of external energy source or radiation. Phosphor converts the absorbed (invisible UV, β, X-rays) energies into visible light. Phosphors consist of a high bandgap inorganic host matrix in which some impurity ions are intentionally added called dopants (activator, sensitizer) [14, 48, 49].

(i) ***Host matrix:*** Generally, a compound with high optical bandgap act as a host matrix for any crystalline phosphor. The inorganic host matrix holds the activator ions strongly as well has the role of sensitizing their luminescence characteristics. Sometimes host matrix may efficiently absorb the high energy ($h\nu_1$) photons and emits radiation in the visible regions with lesser energy ($h\nu_2 < h\nu_1$) as represented in Fig. 1.02 (a) known as self-luminescent materials. A portion of the absorbed energy is released as phonons as a result of atomic collisions or molecular vibrations as illustrated in Fig. 1.02 (b).

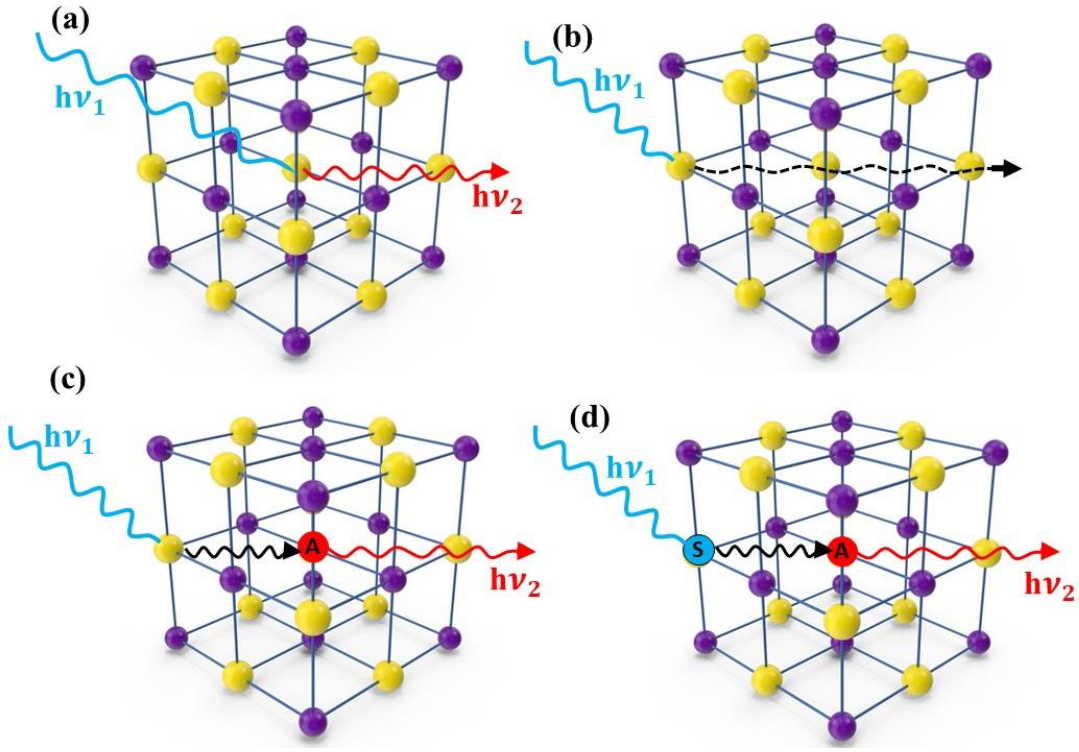

Fig.1.01: *Luminescence processes connecting host, sensitizer and activator.*

(ii) ***Activator:*** Generally, inorganic phosphor host materials are doped with small quantity of impurities or additives or quencher called as activator/dopant ions. When an ion from an activator element leaps to the excited state after absorbing excitation energy and releases the energy as radiation while transitioning back to the ground state [44,50]. As displayed in Fig. 1.02 (c), the high energy $(h\nu_1)$ radiation is absorbed by host lattice, subsequently transfer the energy to activator ions and emission takes place from the activator ions. Activator ions exhibit a variety of responses within different host lattices based on their electrical configuration, structure, and solubility in the glass/phosphor host lattices.

(iii) ***Sensitizers:*** In some cases, there is a very weak absorption by activator ions, then another kind of impurities could be added, termed as sensitizer ions. It enhances the

capacity for absorption and then transfers the received energy to activator ions. Fig 1.02 (d) signifies the mechanism of luminescence involving the absorption of energy by sensitizer and transfer the part of absorbed energy to activator ions. Depending on their electronic configuration, structure, and neighboring atoms in the host lattices, the sensitizer ions behaved in a multitude of manners in the different host lattices [44].

In general, there is a critical activator ion concentration beyond which emission intensity goes down due to concentration quenching, which is caused by cross-relaxation or energy transfer between the nearest ions [51]. Apart from the optimum activator ions concentration, there are so many various factors that affect luminescence characteristics. The other factors such as the synthesis technique, host material, sensitizer ions, environmental conditions affect the luminescence characteristics of the phosphor.

1.3. Fundamentals of RE Ions

In the periodic table, the elements $^{139}_{57}$La to $^{174}_{71}$Lu are designated as lanthanides. All these elements are called rare earth (RE) elements owing to their intermittent distribution in nature, disseminated and not accessible as dense minerals. They have become important due to their distinct characteristics [47]. Due to the distinctive characteristics, they possess, RE ions have been used in practically any field of research and manufacturing, including physics, chemistry and material science. The RE ions includes 14 lanthanides having excellent optical characteristics attributed to the existence of their incompletely filled $4f$ shells shielded by 5s and 5p shells [47,52]. Although the physical characteristics of these elements, such as color, luminescence action, and nuclear magnetic properties, are special, they exhibit identical chemical behavior. However, because the Lu and La elements lack 4f electrons, they are unable to reveal the characteristics of optical absorption, excitation, and emission. RE ions have three

different uses: activator, co-activator, and sensitizer. RE ions incorporated in host crystals are of prodigious attention for diversified applications. Owing to the crystal field of the host material, the energy levels of the RE ions fragmented into numerous Stark levels. The subsequent expansion of the spectral profiles of transitions among those levels regulates the luminescence phenomena, exclusively under broad-spectrum illumination, which are appropriate for solar cell applications. RE ions have exclusive electronic transitions as discussed in the following sections [47].

1.3.1. Electronic Transitions of RE Ions

The RE ions exhibit analogous chemical characteristics, still their physical features are inimitable such as luminescence characteristics and color. The RE elements have a wide range of oxidation states and valency, while the sesquioxide's RE_2O_3 is typically the most prevalent form. RE ions often exist as divalent (RE^{2+}) or trivalent (RE^{3+}) cations, with electronic configurations of $4f^{n-1}\ 5d\ 5s^2\ 5p^6$ or $4f^n\ 5s^2\ 5p^6$. obviously, the particular electrical configuration gives rise to a variety of exciting optical properties that are successfully exploited in commercial applications, and substantial effort is still put into the development of novel materials and the study of physical processes. The atomic number of RE elements, ground state, electronic configuration and ionic radius of the trivalent RE ions are given in Table 1.2. An optical absorption profile of these RE ions in liquid or solid discloses the sharp lines of intra $4f$ transitions. As a result of its optical absorption in the numerous spectral ranges, RE ions emit light in the visible to infrared spectrum, allowing for the recognition of optically active materials for use in photonic and optoelectronic applications. The RE ions activated luminescent materials exhibits various electronic transitions between $^{2S+1}L_J$ to free ion level or J-manifolds in 4f subshell as shown in the Dieke's energy level diagram at Fig. 1.03 [47,53].

Table 1.2: Atomic number of RE elements, ground state, electronic configuration and ionic radius of the trivalent RE ions.

Atomic Number	Trivalent RE^{3+} ions	Ionic radius (RE^{3+}) (Å)	Electronic configuration (RE^{3+})	Ground state
57	La^{3+}	1.032	$[Xe]4f^{0}$	$^{1}S_{0}$
58	Ce^{3+}	1.010	$[Xe]4f^{1}$	$^{2}F_{9/2}$
59	Pr^{3+}	0.990	$[Xe]4f^{2}$	$^{3}H_{4}$
60	Nd^{3+}	0.995	$[Xe]4f^{3}$	$^{4}I_{9/2}$
61	Pm^{3+}	0.983	$[Xe]4f^{4}$	$^{5}I_{4}$
62	Sm^{3+}	0.958	$[Xe]4f^{5}$	$^{6}H_{5/2}$
63	Eu^{3+}	0.947	$[Xe]4f^{6}$	$^{7}F_{0}$
64	Gd^{3+}	0.938	$[Xe]4f^{7}$	$^{8}S_{7/2}$
65	Tb^{3+}	0.923	$[Xe]4f^{8}$	$^{7}F_{6}$
66	Dy^{3+}	0.912	$[Xe]4f^{9}$	$^{6}H_{15/2}$
67	Ho^{3+}	0.901	$[Xe]4f^{10}$	$^{5}I_{8}$
68	Er^{3+}	0.890	$[Xe]4f^{11}$	$^{4}I_{15/2}$
69	Tm^{3+}	0.880	$[Xe]4f^{12}$	$^{3}H_{6}$
70	Yb^{3+}	0.868	$[Xe]4f^{13}$	$^{2}F_{7/2}$
71	Lu^{3+}	0.861	$[Xe]4f^{14}$	$^{1}S_{0}$

The RE ions exhibit stokes shift which is one of the criteria for developing any luminescent material. Due to the presence of a partially filled 4f shell in RE doped materials, photoluminescence is observed. This phenomenon can be attributed to charge transfer transitions, intra-configurationa$4f^{n}$ transitions, or transitions between $4f^{n}$-$4f^{n}$-$5d^{1}$ states.

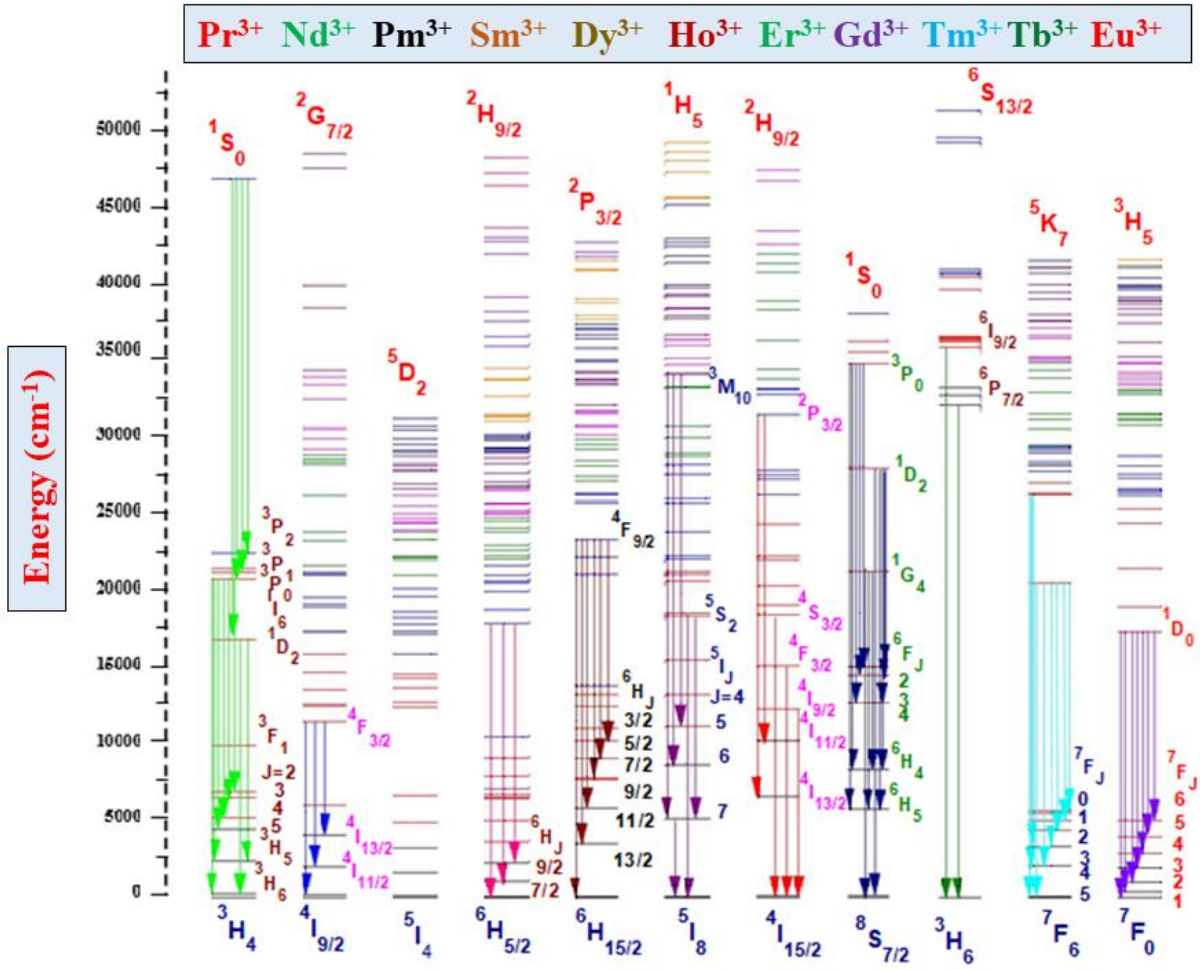

Fig. 1.03: *Energy levels and specific transitions of trivalent RE ions.*

The PL characteristics of RE ions activated phosphor is well understood based on their degenerate energy levels. Generally, the interaction among various levels is categorized on the basis of $f - f$ transitions [54].

(i) *Intra-configurational $4f^n$– $4f^n$* interaction

Excitation and emission energies in $4f^n$– $4f^n$ transitions remain unaffected by the host into which the doping ions are introduced considering that they eventually get shielded from 5s and 5p electrons. That's why the RE ions induced spectra exhibit fine linewidth. The transitions within $4f$ shells are sternly forbidden for the reason that the parity haven't change as per the

Laporte's rule. The fact that the interaction of the RE ion with the crystal field or lattice vibrations can mix states of various parities into $4f$ states or that such transitions are permitted when the spin-orbit interaction occurs made the forbidden transitions evident. The PL lifetime related to $4f - 4f$ transitions is in milliseconds range because of the forbidden character of the PL transition. There are three categories of $4f - 4f$ transitions in the RE ions as follows [47,55]:

a) Electric quadrupole transition
b) Electric dipole/Induced electric dipole transition
c) Magnetic dipole transitions

a) Electric quadrupole transitions

Electric quadrupole transition emerges when a charge has zero dipole moment and quadrupole nature. Electric quadrupole transitions were followed by even parity and noticeably weaker than magnetic dipole as well as induced electric dipole transitions. At that moment, not much research evidence for the electric quadrupole transitions of RE activator ions is present. The quadrupole transitions selection rules can be used for specific definite transitions known as hypersensitive transitions. Electric quadrupole transition is considered as a hypersensitive transition and also recognized as pseudo-quadrupole transitions [47].

b) Electric dipole/Induced electric dipole transition

Incoming light source of excitation has both electric as well magnetic field vector parts. Electric dipole transitions occur when the RE activator ions and the electric field component of the light source interact. On the basis of published literature, it is perceived that the maximum number of the transitions in RE ions are originated as a induced electric dipole. The electric dipole transition is typically arises owing to the linear movement of charges. These kinds of

transitions are forbidden by Laporte's selection rule, but non-centrosymmetric interactions cause electronic states with opposite parity and are referred to as induced electric dipole transitions. The $\Delta l = \pm 1$; $\Delta \tau = 0$; $\Delta S = 0$; $|\Delta L| \leq 6$; $|\Delta J| \leq 6$, $|\Delta J| = 2$, 4 and 6, if J= 0 (or) J′=0 are selection rules for induced electric dipole transitions. The electric dipole transition shows the opposite parity is permitted owing to non-centro symmetric interactions [14,47].

c) Magnetic dipole transitions

A transition known as a magnetic dipole transition occurs when the light source's magnetic field vector component interacts with the activator ions. The magnitude of the total spin angular momentum stays the same throughout the transition of the magnetic dipole. The remaining selection rules such as $\Delta J = 0, \pm 1$; follow most straightforwardly from the requirement that the departing photon has unit angular momentum. Magnetic dipole transition is authorized by the Laporte's selection rule. The magnetic dipole transition is well understood to have a less intense rotational displacement of charge compared to the electric dipole transition. As a result, the transition of the magnetic dipole exhibits even transformation properties under inversion and follows the transitions with equal parity [56,57].

(ii) $4f^{n-1} - 5d$ transitions

The $4f$ and $5d$ subshells can transmit electrons with parity. The intensity of $4f^{n-1} - 5d$ transitions is very sensitive to the proximity of RE ions and their energy is high because d orbitals are significantly influenced by the ligand field effect. This ligand field effect has the outcome of splitting the $5d$ level into a number of levels. The spectral position of the absorption bands related to a specific $4f - 5d$ transition also varies significantly from one host lattice to the next because of the noticeable differences in crystal field splitting. Contrary to this, the

splitting of the $5d$ orbitals and the $4f-5d$ de-excitation do not always affect the emission bands. The emission ranges diverge from n-UV to red region, which is mainly depending on host crystals field [50,58].

1.3.2. Energy Transfer in RE Ions

If resonance exists in the energy difference between their ground and excited states, energy transfer between the nearby RE ions takes place. Either the phosphor host materials or the sensitizer ions absorb the specific excitation source [59]. But radiative emission materializes only due to presence of an activator ions. Thus, the sensitizer ions have taken up the invisible excitation source and that was transferred a part of its energy to the activator, which then releases light, preferably in the form of visible light. In some cases, the small part of the excitation energy of activator can be transferred to other nearest activator ions. In luminescent materials, the absorbed energy in the excited states can released in the following ways [47,60]:

- Direct stimulation of the activator to emit visible light as revealed in Fig. 1.4 (a)

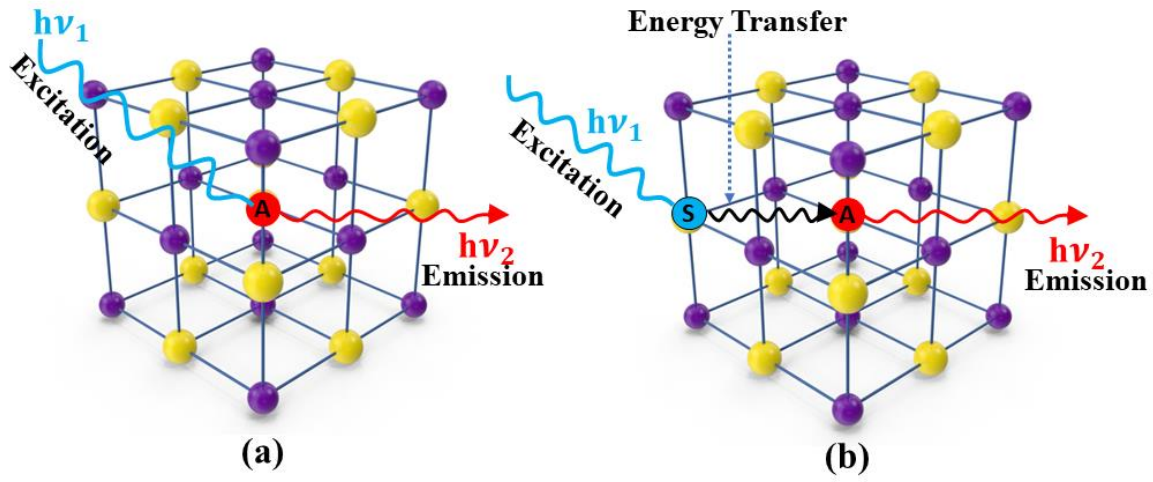

- ***Fig. 1.04:*** *Schematic illustration of (a) excitation and emission by activator ions; (b) excitation, energy transfer and emission process among the sensitizer and activator ions in phosphor.*

- Visible light emission from the activator ions via absorbed energy transfer from the sensitizer to the activator as showing in Fig. 1.4 (b).

In luminescent materials, mostly Stokes emission takes places in down conversion luminescence process. As per Stokes emission, the emitted photons energy is always less than the incident photon i.e., $(h\nu_1 < h\nu_2)$.

Four fundamental mechanisms make up energy transfer (ET) processes among RE ions after photon or radiation absorption:

(i) Resonant radiative ET from emission of sensitizer and re-absorption by activator ions.

(ii) Non-radiative energy transfer linked with resonance among sensitizer and activator.

(iii) Multi-photon assisted energy transfer.

(iv) Cross-relaxation (CR) in intermediate energy levels of two identical ions.

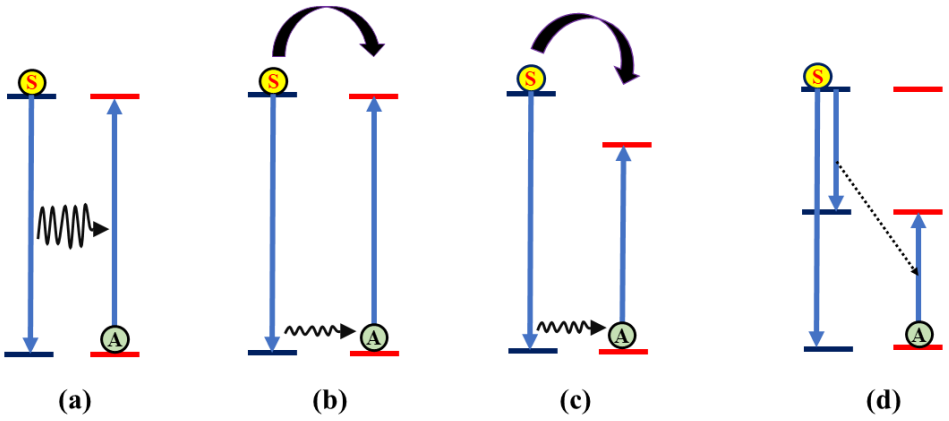

Fig.1.05: *ET processes (a) resonant radiative energy transfer between sensitizer and activator ions; (b) non-radiative energy transfer with resonance between sensitizer and activator; (c) multiphonon-assisted ET; and (d) CR between two RE ions.*

For better energy transfer one of the important pre-conditions is overlap between the excitation spectrum of the activator with the emission spectrum of the sensitizer for possible

interaction and characteristic transitions between them. The radiative energy transfer efficiency is mostly depending upon excitation of activator ions via sensitizer emission as epitomized in Fig. 1.05 (a). In first case, if radiative energy transfer takes place between the activator and sensitizer, decay time of the sensitizer does not vary with activator ion concentration. In second case, for the energy transfer mechanism, there should be an identical energy difference between the excited states of the sensitizer to the activator as illustrated in Fig. 1.05 (b). In this instance, the non-radiative energy transfer is indicated by the decay time of a sensitizer drastically decreasing with increasing activator concentration. If energy variation between the excited state energy level of sensitizer and activator ions is large then, the ET probability is negligible which is named as phonon-assisted non-radiative transitions as revealed in Fig. 1.05 (c). If the two ions have dissimilar excited states, then the cross-relaxation process rises and ET between identical two adjacent doping ions. Fig. 1.05 (d) demonstrated the excited state energy levels in relation to the cross-relaxation process, where the first ion, which is primarily in an excited state, exchanges energy with the second ion, which is initially at ground state, causing both ions to simultaneously lie to some intermediate states within the energy between the two initial states [61–63].

1.3.3. Concentration Quenching Mechanism

In RE doped materials, the intensity of luminescence increases up to certain concentration of RE ions doped in them and decreases beyond it. This process is called concentration quenching. The enhancement in luminescent intensity takes place because of increase in absorption efficiency and remains highest up to a particular concentration of doping ions named as critical concentration. The prime cause for concentration quenching in any RE ions doped phosphor host lattice is energy transfer among activator ions. At a certain

concentration, the distance between acceptor and donor atoms decreases in such a way that the energy transfer between the atoms leads to concentration quenching. The process of concentration quenching can be explained in two different ways.

(i) In first type of mechanism, the excitation energy can be distributed into various luminescent centers before being emitted due to dominating energy transfer. These excited luminescent centers relax to their ground state by multi phonon relaxation. These centers can also act as energy sinks within the transfer chain and outcomes in quenching of emission intensity [64].

(ii) In second category of mechanism, the excitation energy will be consumed from the emitted state via cross-relaxation process, which took place by resonant energy transfer among the two adjacent activator ions.

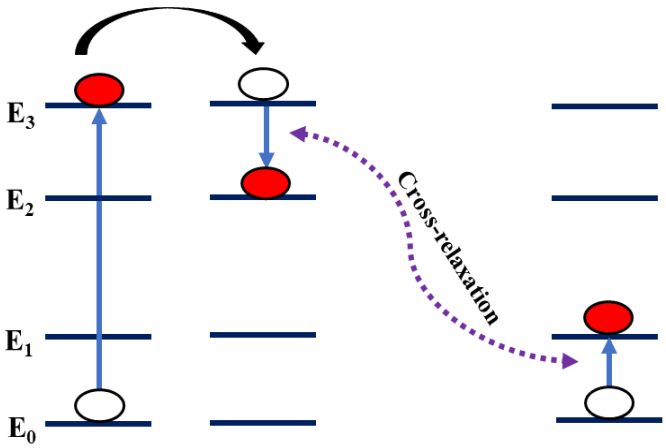

Fig. 1.06: *Cross-relaxation between pairs of centers.*

The energy level diagram having cross-relaxation is depicted in Fig 1.06. If the energy difference (E_3-E_2) of one luminescent center (donor) is equal to energy difference (E_0-E_1) of another nearby center (acceptor), resonance energy transfer takes place which strongly depends

upon the nature of energy levels. In a cross-relaxation process, the excited electron falls from E_3 to E_2 act as a donor center, and release the energy, which was absorbed by another electron at E_0 and move from E_0 to E_1 levels act as acceptor. Due to the non-radiative energy transfer among the nearest activator ions leads to quenching of emission intensity.

The concentration quenching resulting in a decline in emission intensity may be caused by an increase in the rate of non-radiative ET among doped RE ions. Generally, the probability of non-radiative ET depends on the critical distance between two closest doped RE ions. The critical distance is estimated via employing the expression given by Blasse [63]:

$$R_c = 2\left(\frac{3V}{4\pi C_{\circ} N}\right)^{1/3} \tag{1.01}$$

where R_c is the critical distance, V is the unit cell volume, C_o is doping ion concentration (mol), and N is the number of the cation sites in the host unit cell. R_c value define the types of interaction among the doped ions. If the R_c value more than 5 Å, than the electric multipole moment interaction is the prime cause of concentration quenching [65].

Furthermore, Dexter defined the luminescence intensity I and doping ion concentration x relation as below [64, 66, 67]

$$\frac{I}{x} = K[1 + \beta(x)^{Q/3}]^{-1} \tag{1.02}$$

here, K and β are constants for the same excitation of a given host lattice. The value of Q explains the type of multipolar interaction presented in luminescent materials having the values of Q = 6, 8, and 10 for dipole-dipole, dipole-quadrupole, quadrupole-quadrupole, respectively [68]. Assuming that $\beta(x)^{Q/3} >> 1$, the equation (1.02) can be approximately reduced as follows:

$$log\frac{I}{x} = K' - \frac{Qlog(x)}{3};\ (K' = logk - log\beta) \tag{1.03}$$

The value of Q has been assessed using the slope of the plotted graph among $log(I/x)$ and $log\ (x)$. The estimated value of Q confirms the type of energy transfer among the two closest doping ions.

1.4. Colorimetry Properties

An abundant visible peak with a range of intensities is present in the emission spectra of phosphors doped with RE ions, and this peak's link to the susceptibility of human vision is a crucial component of luminescence. The actual color of light emission spectrum is confirmed by its wavelength and corresponding chromaticity coordinates. The Commission Internationale de l'Eclairage (CIE) color coordinates are utilized to examine actual color of emission spectrum of luminescent materials. The different colors in the visible region can be analyzed by comparing CIE color coordinates estimated by PL spectra and standard equal energy points. To find the CIE color coordinates, first step is to evaluate the tristimulus values (X, Y and Z) on the basis of power spectral density as follows [69]:

$$X = \int \bar{x}(\lambda)P(\lambda)d\lambda \tag{1.04}$$

$$Y = \int \bar{y}(\lambda)P(\lambda)d\lambda \tag{1.05}$$

$$Z = \int \bar{z}(\lambda)P(\lambda)d\lambda \tag{1.06}$$

in the above equations, $\bar{x}$, $\bar{y}$ and $\bar{z}$ signifies the matching functions well-defined in the CIE diagram as revealed in Fig. 1.07. CIE color coordinates were assessed with help of calculated X, Y and Z values via employing the following expression:

$$x = \frac{X}{X+Y+Z} \tag{1.07}$$

$$y = \frac{Y}{X+Y+Z} \tag{1.08}$$

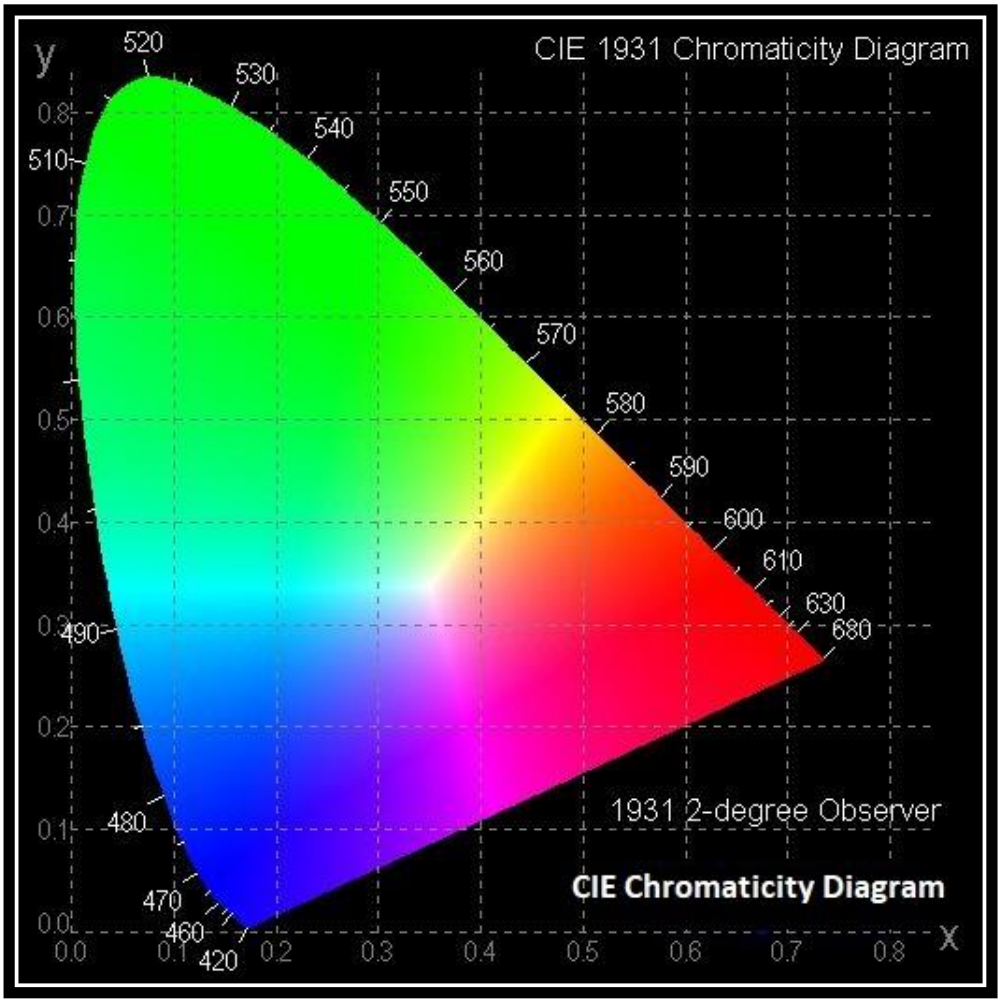

Fig. 1.07: *CIE chromaticity diagram.*

The temperature of the utmost analogous to blackbody radiator is entitled as correlated color temperature (CCT) of the light emitting source. A black body is a perfect physical substance that absorbs all inward radiation, regardless of incident angle or wavelength and without any emission of radiations at 0 K. As a result, the CCT is defined as the absolute temperature of a blackbody whose chromaticity is close to that of the light source. The CCT is an important parameter for the identification of cool or warm white lighting devices. A lamp with a low value of CCT (<5000 K) shows the warm appearance of emitted light. While the lighting devices with high value of (>5000 K) CCT signifies the cool nature of emitted light. In

short, the CCT is the color of the light emitted from the lamp and the color appearance itself. The CCT can be estimated expression established by McCamy [70]:

$$CCT = -449n^3 + 3525n^2 - 6823.2n + 5520.3 \quad (1.09)$$

here, $n = \frac{x-x_e}{y-y_e}$, $x_e = 0.332, y_e = 0.186$, which denotes the coordinates for epicenters. Higher the CCT, better will be the visual acuity with higher brightness perception.

1.5. Importance of the Present Proposal

Green technology is defined as technology that is ecofriendly to our planet's environment. In recent years, demand for energy efficient green technology and environment-friendly energy sources has rapidly increased. In this technology, special attention has been paid to the production and consumption of clean energy sources, which are not harmful to our environment, unlike the traditionally used fossil fuel energy sources and secretion of greenhouse gases. Therefore, it is a big challenge for researchers to develop environmental friendly green technology. Solid-state artificial lighting is an example of a green technology that incorporates biotic cultures, human development, and the environment while significantly reducing greenhouse gas emissions. The prepared phosphor may have the capability to reduce greenhouse gas emissions and can be a potential candidate for solid-state artificial lighting, which overcomes drawbacks of commercial phosphor such as the halo effect, low color rendering index and high correlated color temperature due to the lack of red color [26–28]. However, the lack of red light in the PL spectral profile of such commercial w-LEDs results in a low CRI and a high CCT. Fig.1.08 (a) illustrated the pc-w-LED uses YAG: Ce phosphor coated on InGaN blue LED chip and gives the bluish white light. To overcome these

shortcoming via prepared UV/near-UV/blue pumped efficient visible light emitting phosphor and gives proper white light.

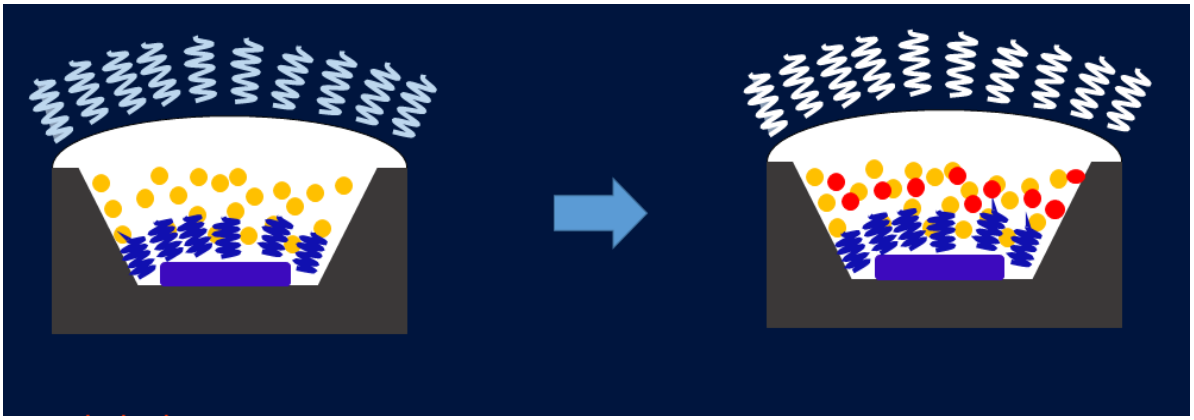

Fig. 1.08: *Improvement of shortcomings in commercially used phosphor converted w-LEDs.*

The current research work has a goal to reduce the power consumption and enhance the power generation via utilizing the versatile phosphors in the energy efficient optoelectronic devices. Phosphors have great potential for optoelectronic device applications, which are capable to enhance the efficiency of existing silicon solar cells via converting the unabsorbed portion of the solar radiation into useful counterpart.

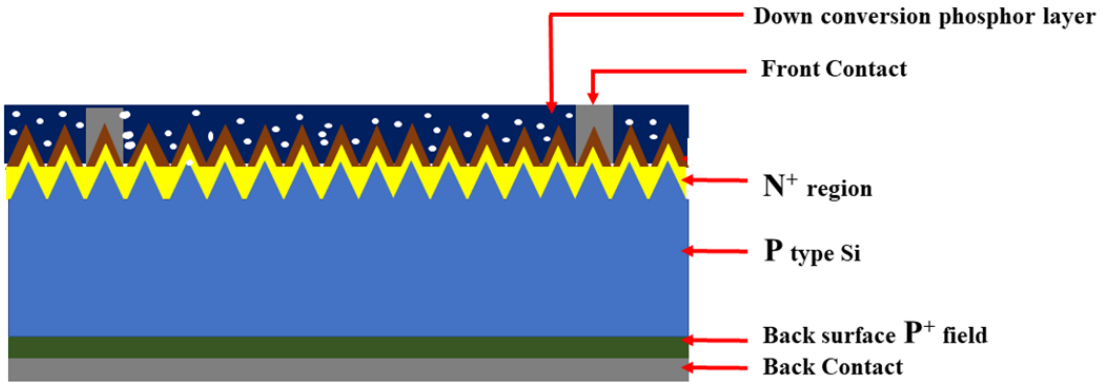

Fig. 1.09: *Enhancement of solar cell conversion efficiency through the down-converting phosphor.*

The investigators strongly believe that the efficiency of photovoltaic cells will improve further when they are combined with prepared rare earth phosphor as illustrated in Fig 1.09. Up or down conversion luminescence studies of RE doped crystalline phosphor in association with photovoltaic solar cells with improved efficiency can raise a curtain for a new era in the field of renewable energy sector [71,72].

Additionally, phosphors have lots of applications in a wide range of fields, including scintillation, X-ray intensification, and advanced optical displays. As a result, significant effort has been made to date in the exploration of useful phosphor materials. Furthermore, RE doped phosphor has gained extra consideration due to their high photo-stability. The parameters, PL intensity, PL lifetime and PL intensity ratio have utilized to monitor the real time temperature of substances [73–75]. On the other hand, a photonic based thermometer using the fluorescence intensity ratio (FIR) approach is seen as an advantageous method for measuring temperature because it has inherent protection from some external conflicts and high sensitivity as demonstrated in Fig. 1.10 [76–78].

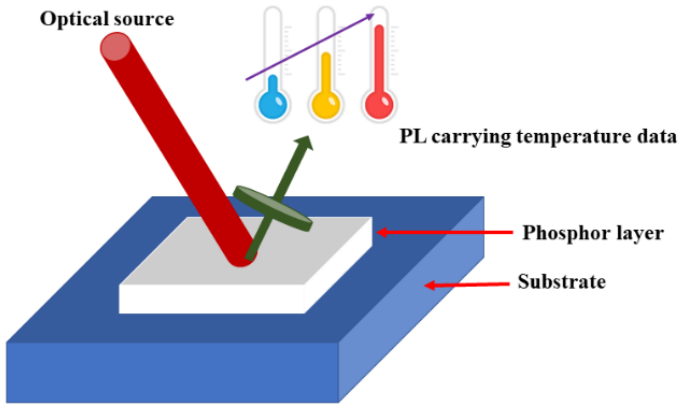

Fig. 1.10: *Strategy to utility of phosphor for temperature sensing application.*

Also, photonic based optical sensors have attracted a lot of attention among the many

temperature sensing schemes because they have many advantages: small sensor size, which means quick response, non-contact, high precision, electromagnetic resistance, and in-situ capabilities [79–81].

1.6. Selection and Importance of Host

An advanced optoelectronic device based on versatile phosphor with numerous advantages can fulfil the demand and consumption of power requirement and can approach the theoretical limits of energy efficient photonic devices. In the current decades, a number of luminescent materials have been prepared and reported in support of energy efficient photonic devices. There are challenges to prepare a versatile efficient phosphor that meet the prerequisite of optoelectronic devices [82–85]. Hence, the major challenges that can be explicate from the necessities in energy efficient optoelectronic devices as: i) High bandgap host with high RE ions doping capability. ii) Efficiently absorb n-UV/blue light and emits in the desirable visible region. iii) Excellent thermal and chemical stability as anticipated for optoelectronic devices applications. iv) high quantum efficiency with less effect of temperature on luminescence characteristics. Hence, the selection of luminescence host lattice is one of the crucial steps for the development of energy efficient versatile phosphor.

Numerous luminescent host materials such as oxides, nitrides, fluorides, niobates etc. have been explored for many applications in the field of science and technology. Phosphate-based phosphors are the most popular choice among all inorganic phosphor hosts for optoelectronic device applications because of their excellent chemical and thermal stability, low sintering temperature, low cost, high luminous efficiency, strong UV absorption, and low phonon energy materials [86,87]. Phosphate compounds are known as multifunctional materials. The prepared phosphate-based phosphors are used in a wide range of domestic and

commercial applications, including SSL, high-tech optical displays, optical waveguides, and lasers, among others. Additionally, RE doped orthophosphate phosphors have received a lot of attention for use in displays and light-emitting diodes [88,89]. The exceptional optical, magnetic, and dielectric properties of the eulytite type orthophosphate, with the general formula $A_3B(PO_4)_3$ (A = divalent alkaline earth & B = trivalent Bi or RE ion), as well as their thermal and chemical durability, have received attention [90,91]. All eulytite structures can be synthesized at a reasonable temperature, although calcium-based eulytite type orthophosphate [$Ca_3Bi(PO_4)_3$] phosphor is the easiest to do so [92]. Owing to their disordered structure, eulytite-type materials doped with rare earth ions display fascinating luminescence capabilities [93]. It was found from the literature review that eulytite-type materials can serve as important host matrices for lighting applications [91]. Recently, a number of phosphor have been reports related to RE ion activated eulytite-type orthophosphate phosphors, like $Ba_3Y(PO_4)_3$, $Sr_3Y(PO_4)_3$, $Ba_3Lu(PO_4)_3$, $Sr_3La(PO_4)_3$, etc. [94–97]. A comparison study of the luminous characteristics of $Ca_3Bi(PO_4)_3:Eu^{3+}$ phosphor synthesized using three distinct methods was published by Yu et al. [98].

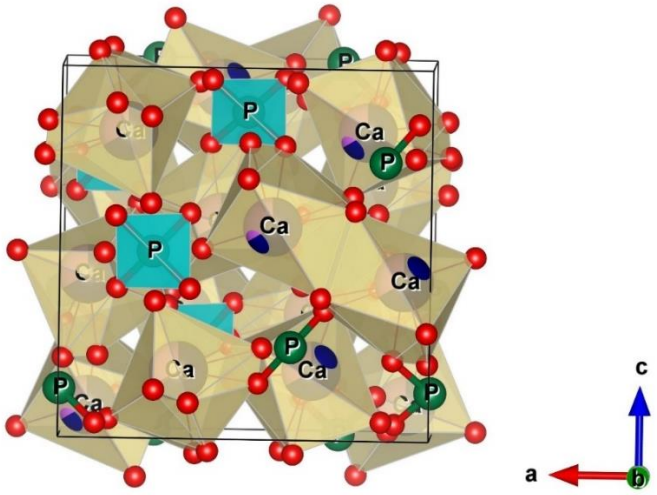

Fig. 1.11: *Cubic structure of the proposed $Ca_3Bi(PO_4)_3$ phosphor host lattice.*

The cubic unit cell structure of $Ca_3Bi(PO_4)_3$ host lattice is presented as Fig. 1.11. For easy adaptation of the synthesis method of phosphors by any industry, the focus will be laid on scaling-up of the processing parameters to a certain extent.

1.7. Outline of the Problem and Objectives

Solid inorganic phosphor plays an important role in the development of various advanced optoelectronic devices. Nowadays, a large number of inorganic phosphors have been synthesized via various solid state or chemical routes [39,99,100]. The foremost role of phosphor is to convert the source of excitation energy into visible or infrared light. According to the wavelength conversion, phosphor can be classified into two groups: (i) Down converters absorb high energy/shorter wavelength of light (UV or n-UV) and emit into lower energy/longer wavelength of light. (ii) Up converters do the opposite, which absorb two or more photons of lower energy (NIR or IR photons) convert them into higher energy photons [10,101,102]. The wavelength of the emitted light depends on the doped rare earth or transition metal ion. Therefore, rare earth or transition metal ions play crucial role in phosphor.

RE or transition metal ions doped phosphors have received a lot of attention from researchers in recent years due to their potential uses in sensors, dosimeters, solid state lasers, field emission displays, light converters, scintillators, and other optoelectronic devices. [48,103,104]. Apart from these applications, the spectral mismatch energy losses can be minimized by using phosphors. Phosphors can transform high- or low-energy photons into a spectrum range that silicon-based solar cells can use to increase their conversion efficiency [105]. Consequently, there is a need for effective phosphors that can efficiently absorb the sun's spectrum's unabsorbed portions and transform them into wavelengths that the solar cell is able to utilize in order to generate an electron-hole pair.

Rare earth or transition metal ions doped DC phosphor can be utilized in 4th generation solid state lighting (SSL) devices to save the huge amount of power consumption. Thus, there is a need of efficient down conversation approach to SSL, which uses near-UV or blue LEDs, combined with phosphor to produce various colors in the visible spectrum. To overcome the halo effect, poor color rendering index and high correlated color temperature value in SSL, development of efficient single-phase phosphor has become an essential task. Therefore, white light emission from a single-phase phosphor has gained significant attention in comparison to RGB phosphors [106]. Major challenges are to synthesize phosphor having properties of high luminous efficacy, high chromatic stability, brilliant color-rending properties and price competitiveness.

Current research focuses primarily on the synthesis of strategic luminous materials, their morphology/microstructural characterizations, enhancement of luminescent properties, fabrication of phosphor-based devices, and its optoelectronic applications. Therefore, the below mentioned objectives of the present proposal for producing most efficient phosphor with improved luminescent properties by scaling-up the process for comfortable industrial acclimatization.

- Rigorous literature survey on the material proposed will be carried out from time to time.
- To synthesize proposed phosphate-based host lattices using solid-state reaction and co-precipitation methods.
- Identification and effective incorporation of dopants, co-dopants, fluxes, sensitizers, etc. to optimize the synthesis parameters.
- To study in detail, the luminescent and various colorimetric/photometric properties of the optimized phosphor for optoelectronic devices applications

- To analyze energy transfer properties of rare earth doped and co-doped micro and nanostructured calcium bismuth phosphate phosphor.
- Comparative study of structural, optical and luminescent properties of the phosphors prepared by various routes.
- For w-LEDs applications:
    - This will be achieved by making appropriate choice of rare-earth dopants in phosphate-based host. Single or multiple rare-earth will be doped in the host matrix to optimize white light emission.
- For solar cell applications:
    - To synthesize down-conversion phosphors to explore as the solar spectral convertors for solar cell applications.
- For optical thermometry:
    - To synthesize phosphor to explore as the advanced temperature sensor.
- Finally, to design color tunable phosphor for its utilization in various optoelectronic applications.

CHAPTER 2

Experimental Work and Characterization Techniques

This chapter is focused on the synthesis and characterization techniques required for the development of an efficient phosphor with excellent PL characteristics. The efficient multifunctional material needs appropriate acquaintance of numerous synthesis procedures along with the proper characterization techniques for the potential utility of the appropriate RE ions activated $Ca_3Bi(PO_4)_3$ phosphor in optoelectronic devices. The characteristics of RE ions doped phosphors were scrutinized via employing the numerous characterization techniques used to explore their structural, vibrational, morphological and optical characteristics for the utility in advanced optoelectronic devices. To understand the instruments better, working principles, device descriptions and operational controls of characterization tools used in the present research work are described in the current chapter.

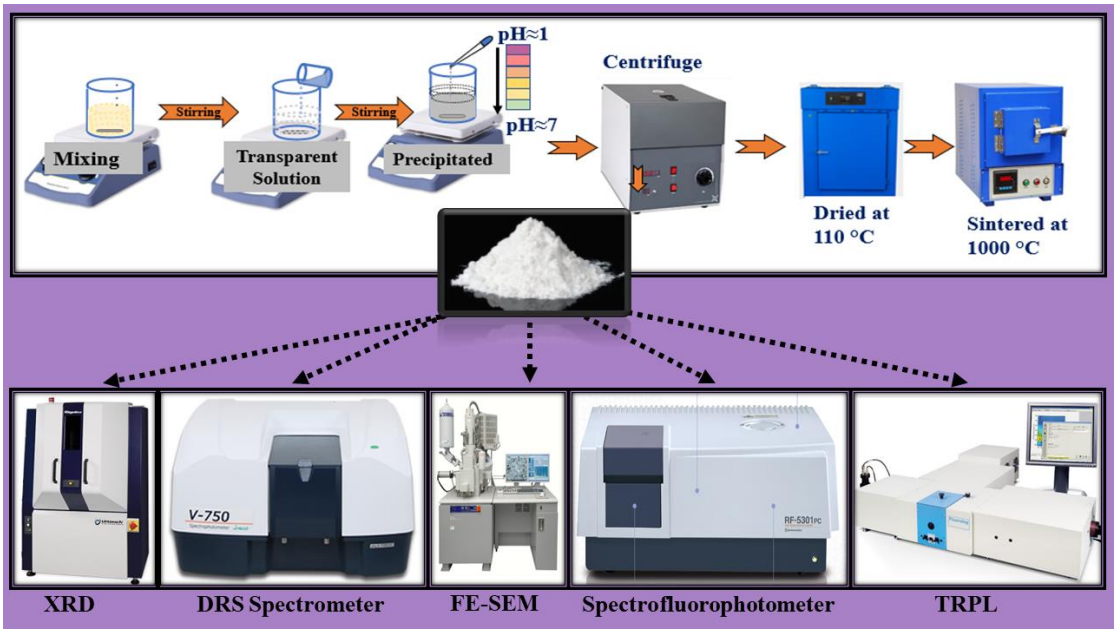

2.1. Experimental Work

The preparation of efficient multifunctional material needs appropriate acquaintance of numerous synthesis procedures along with the proper characterization techniques. This chapter deals with the detailed experimental procedure and characterization techniques used throughout the thesis work. Synthesis of RE ions doped phosphor along with the characterization techniques is described in flowchart Fig. 2.01 for its utility in advanced optoelectronic devices. The fundamentals of optimizing the experimental procedures learned and the statistical method employed for analysis are covered in this chapter.

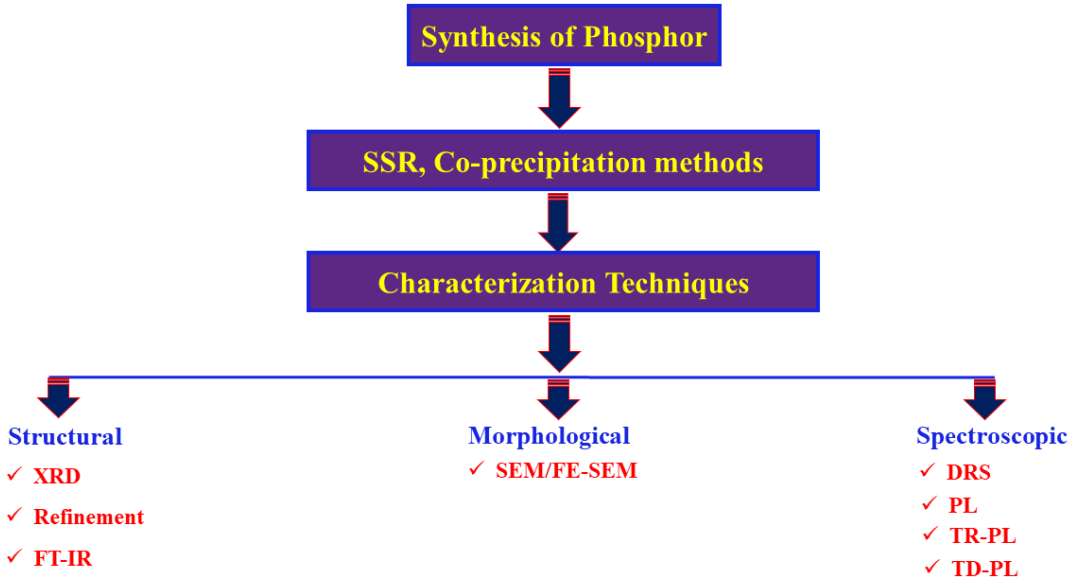

Fig. 2.01: *Schematic representation of phosphor synthesis and used characterization techniques.*

The structural, vibrational and morphological features of the synthesized phosphor have been scrutinized via employing X-ray diffractometer, Fourier transform infrared spectroscopy (FT-IR), scanning electron microscopy (SEM). The spectroscopic characteristics of a phosphor was recorded by equipment like diffuse reflectance spectroscopy and spectrofluorophotometer etc. For a better understanding of the instruments, the ray diagrams of the characterization

techniques are supplied along with descriptions of how they operate, device descriptions, and operational controls.

2.2. Synthesis of Phosphors

Phosphor sample synthesis is an important step in material analysis process. Various synthesis methods such as molten salt, solid-state reaction (SSR), co-precipitation, sol-gel, combustion, hydrothermal, and solvothermal have been used to synthesize phosphors [107–109]. To create a variety of powder materials and phosphors, the SSR process is one of the most straightforward and widely used method [110].

2.2.1. Solid State Reaction (SSR) Method

SSR method is one of the standard and common technique for the preparation of crystalline ceramic powders of phosphor. In SSR method, the dry media reaction was taking place. The SSR process is widely used for developing phosphors for industrial usage, where quick turnaround times, cheap costs, and high-volume production are required [111]. This approach involves weighing high purity chemicals in a stoichiometric ratio and dispersing them in acetone. To ensure the precursors are ground uniformly, the ingredients are then ground for a long duration. It is necessary to heat the uniformly grounded ingredients at high temperatures because these solid materials in powder form do not react at room temperature, even when maintained for hours. After being poured into an alumina crucible, the ground samples were held in a programmed muffle furnace for high temperature sintering. The resulting phosphor is ground to guarantee homogeneous sintering of the samples after allowing samples to naturally cool to room temperature.

Eulytite type Eu^{3+} activated $Ca_3Bi(PO_4)_3$ phosphors have been prepared employing SSR method as described in flowchart Fig 2.02. The highly pure $CaCO_3$, Bi_2O_3, $NH_4H_2PO_4$ and

Eu_2O_3 were used as precursor materials for synthesis of the phosphor. The stoichiometric ratio of the precursor materials was weighed using an electric weighing balance and taken in an agate mortar for one hour grinding. Ethanol used as a dispersing medium for grounding. Finally, the well-grounded mixture was kept in a crucible (alumina) and placed in the programmable electric furnaces. The two-stage heating profile was applied as, 700 °C for 1 h and 1200 °C for 4 h in the air medium. At last, the prepared sample was permitted to naturally cool to room temperature (RT) and crushed again for further characterizations.

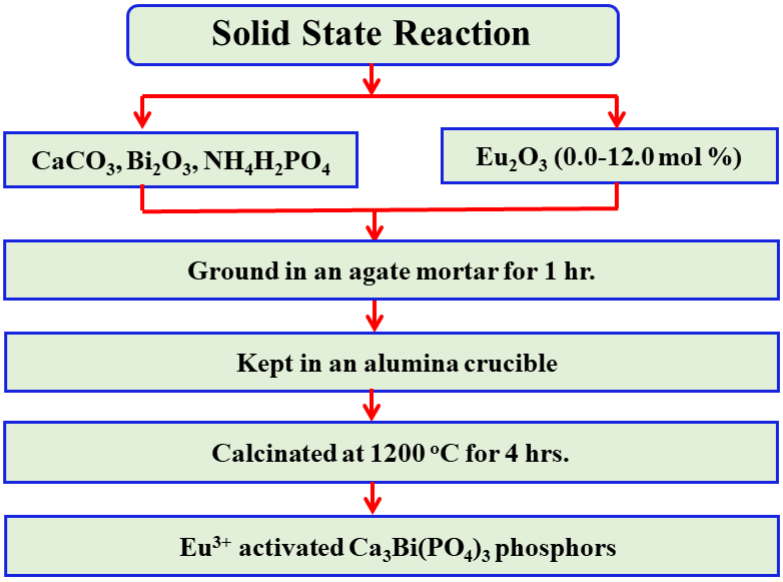

Fig. 2.02: *Flowchart of Eu^{3+} activated $Ca_3Bi(PO_4)_3$ phosphors preparation via SSR method.*

The luminescent properties of the phosphor get influenced by synthesis technique, since it affects the particle morphology, size, homogeneity and calcination temperature etc. Apparently, SSR process consumes more energy and also has contamination of impurities. Moreover, resulting in inhomogeneous composition and morphology of the final products. Thus, SSR process is especially unsuitable for phosphor with controllable morphologies and non-agglomerated regular particles. Hence the chemical routes preferred for the preparation of

efficient homogeneous phosphor particles. Among the various chemical routes, co-precipitation method has been preferred for further phosphor preparation, due to its advantages such as easy process, homogeneous mixing of reactant, high yield, inexpensive equipment, less-reaction time and the reaction takes place at normal atmospheric conditions [112,113]. Yu et al. reported a comparative study of luminescent properties of $Ca_3Bi(PO_4)_3$ phosphor synthesized via three different routes, which revealed that the $Ca_3Bi(PO_4)_3$ phosphor prepared via co-precipitation method has better luminescent characteristics as compared with proposed phosphor prepared via SSR and sol-gel methods [98]. Hence, the co-precipitation method has been used for the preparation of RE activated $Ca_3Bi(PO_4)_3$ phosphor.

2.2.2. Co-precipitation Method

Co-precipitation is the simple, industrially viable, cost-effective and fast synthesis routes that can be used for the preparation of oxide-based phosphor/nanophosphor. In the chemical process of co-precipitation, solid particles are precipitated from a solution that contains precursor molecules or ions. By adsorption on the surfaces of the developing particles and physical frame-up in the pore spaces, these ions are integrated into the solid. One of the main mechanisms of the co-precipitation approach is adsorption. The solid species, or adsorbent, is introduced to a solution that also contains other ions, known as adsorbates, in this process. In this instance, physical or chemical interactions between one adsorbate and the adsorbent bind the adsorbates to the surface of the solid. The main advantages of the co-precipitation method are the high product purity, high yield, low cost and easily reproducible.

A systematic procedure was demonstrated in Fig. 2.03 to prepare CBP doped with rare earth (Dy^{3+}, Er^{3+}, Sm^{3+}/Eu^{3+}) phosphor via employing chemical co-precipitation routes. The

stoichiometric amount of chemicals $Ca(NO_3)_2 \cdot 4H_2O$, Bi_2O_3, H_3PO_4 and rare earth oxides were used as precursors.

At the start, the required amount of $Ca(NO_3)_2 \cdot 4H_2O$ was dissolved in the deionized water. Required amount of Bi_2O_3 and rare earth oxides were dissolved in a minimum amount of HNO_3. After that, precursor solutions have been mixed all together, followed by dropwise adding a required amount of H_3PO_4 and thoroughly stirred for 1hr. After that transparent solution was obtained, then add 2 grams of PEG-4000 and DI water solution.

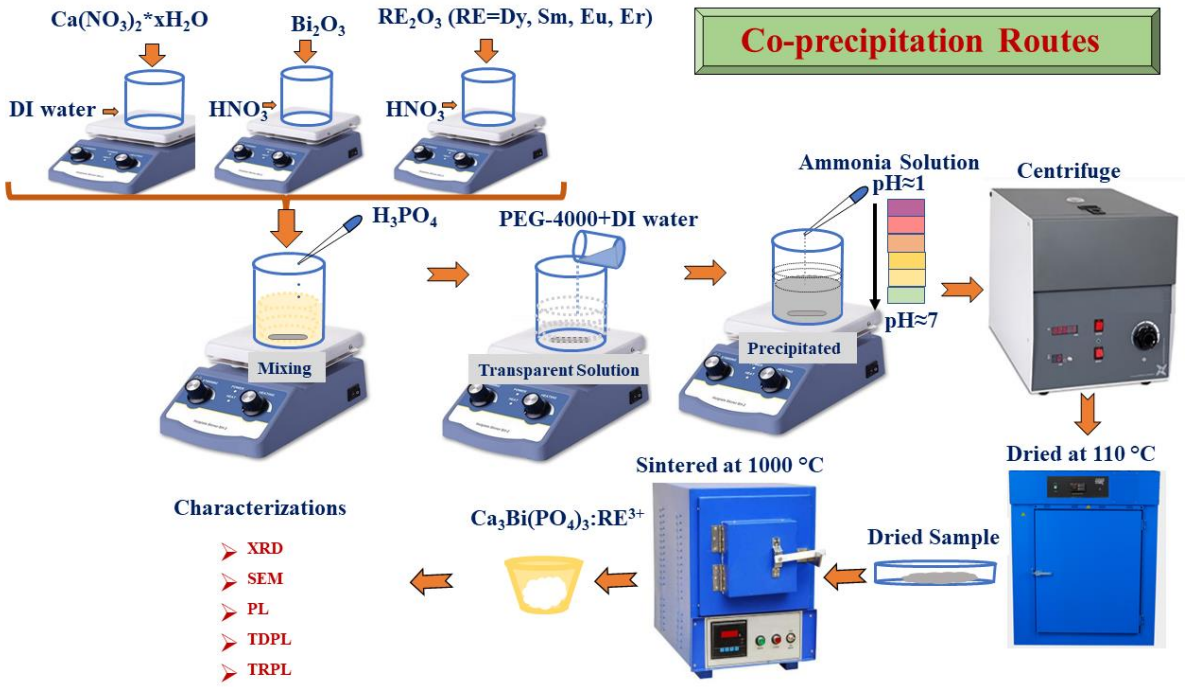

Fig. 2.03: *Schematic representation of samples synthesis procedure via co-precipitation routes.*

The resultant solution was transparent and clear with pH~1. Further then, the pH value was adjusted from 1 to 7 using an ammonia solution, which transforms the clear solution into white precipitate. Later the white precipitate solution was aged for 2 hrs. The white precipitate was separated using centrifuge the solution followed by washing several times with deionized water and ethanol, which removes the residual chemicals. The resultant white precipitate material was dried at 110 ˚C for 12 hrs and sintered at 1000 ˚C for 2 hrs in an air medium to

form the crystalline sample. Subsequently, the sintered sample was cooled to RT and ground using agate mortar pestle for further investigations.

2.3. Characterization Techniques

The material characterization tools were very imperative part of research, which empower investigators to identify the structural characteristics, how this characteristic related with other electrical, optical, mechanical properties, and how these properties were applied in technological applications. Characterization and results are very important for the preparation and optimization of efficient phosphor for distinctive applications in the field of science and technology as well as daily life. In order to study various structural, vibrational, morphological and luminescence characteristics of the prepared phosphor, sophisticated analytical characterization techniques were essential. Hence, the current section deeply explained about the characterization techniques and their working principle. Utilizing tools that are industry standard, synthesized phosphors have been evaluated to determine their structure, morphology, and luminous characteristics. The following sections of this chapter go into extensive details about the experimental methods used to characterize the phosphors as they were synthesized.

2.3.1. X-ray Diffraction (XRD)

In the field of materials synthesis, one of the primary attentions is the phase identification of the prepared compounds with proper crystalline structure or amorphous nature. The phase identification of the materials analyses via XRD techniques, which is an important instrument in materials science for quantifying, identifying and illustrating single/polycrystal's or any compounds. XRD patterns reveals the various crystalline structural properties such as single/multiphase, defects, purity, stress, strain, crystallite size, etc. XRD technique is based on Bragg's law, which causes monochromatic X-rays to constructive interference when they strike

crystalline materials and comply with the diffraction rules. When incident X-ray wavelength and sample atomic spacing are equivalent, Bragg's law-based constructive interference results in the perception of a diffraction peak. In surface of the sample, X-ray radiation was incident with different angle θ and scattered from different lattice planes of samples. These scattered X-ray radiations form constructive interference, when the travelled path of each wave having comparable to an integer multiple of the wavelength as per the by Bragg's law [114]:

$$n\lambda = 2d\ sin\theta \tag{2.01}$$

In the Braggs equation, n denotes integer, λ denotes X-ray wavelength, which is around 1.54 Å for $CuK\alpha$ source, θ denotes the glancing angle and d denotes spacing between planes. Schematic representation of X-ray diffractometer can be seen in Fig 2.04.

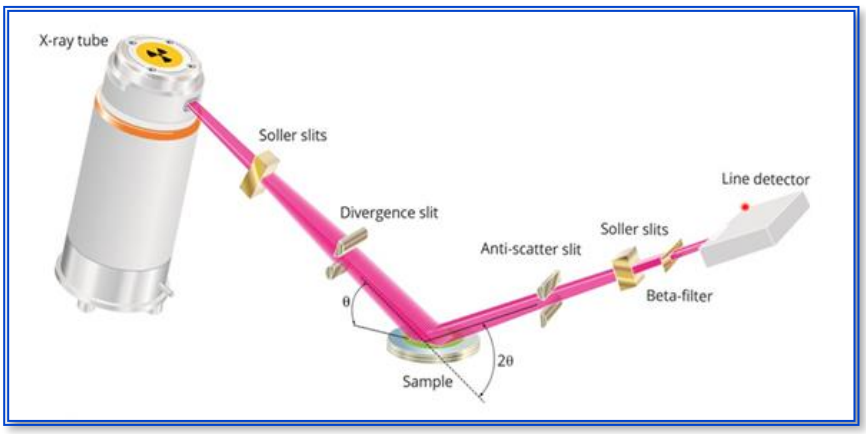

Fig. 2.04: *Schematic representation of X-ray diffractometer.*

X-ray diffractometer equipped with movable X-ray tube, different types of slits, sample holder, goniometer and a rotating X-ray line detector. XRD, working procedure started from the generation of X-rays followed by striking on sample and finally detection of diffracted X-rays by detector. X-ray generation takes place by high energy electrons were strike on the rotating metal anode target (Cu), which emits the different rays including X-rays. X-rays departure from the tube through Be windows, which provide transparent medium for generated X-ray.

Characteristically, the K_α line is selected and filtered out other lines via thin metal foil made up of nickel. X-ray incident on the placed sample, which rotates at an angle θ with path of incident X-ray beam. Goniometer can manage the rotating angle of sample as well as detector. When the incident X-ray subsequently striking on surface of the sample and satisfies Bragg's equation, which makes the constructive interference. The detector rotates at 2θ with respect to the path of incident X-ray beam, which can detect the incident diffracted X-rays beam and converts the signal to count rate. Finally, detected X-rays counts were directly fed to the computer, which can plot a graph between X-rays counts with respect to angle 2θ and recorded for further process. Rigaku Ultima IV and Bruker D8 advance X-ray diffractometer were used to record XRD profile for the prepared crystalline powder samples as shown in Fig 2.05 (a & b), respectively.

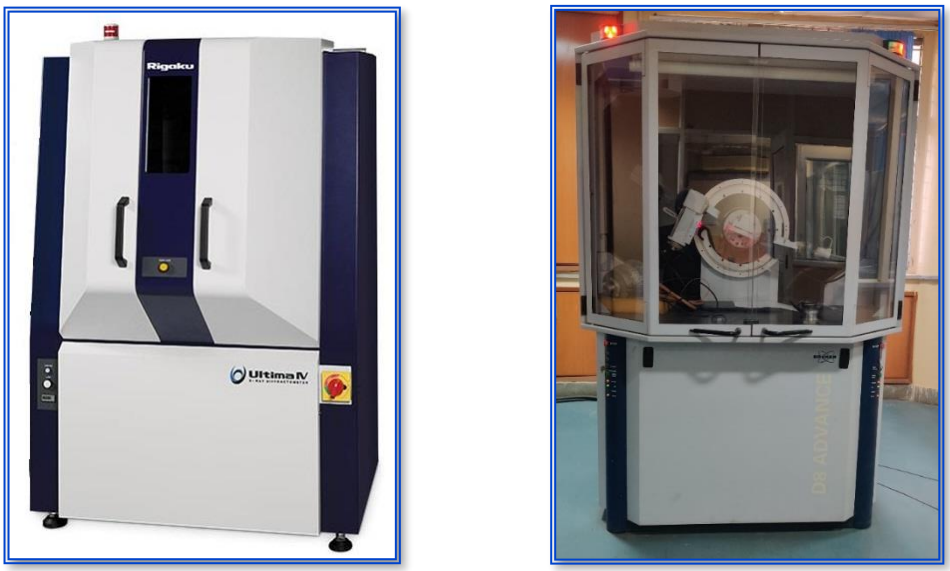

Fig. 2.05: *(a) Rigaku Ultima IV and (b) Bruker D8 Advance X-ray diffraction machine.*

The recorded XRD crystalline patterns were compared with the available standard data JCPDS (Joint Committee on Powder Diffraction Standards) and find out the best appropriate matched patterns. The matched standard data gives the information about crystal structure and

their unit cell parameters, Wyckoff positions, space groups etc. Using this information, various structural studies like Rietveld refinement, has been performed. Also, with the help of XRD crystalline peaks position and peak broadening (full width at half maxima: FWHM) of the patterns, the crystallite size of the material sample can be estimated using the Debye Scherrer's formula and Williamson Hall (W-H) equation as follows [115,116]:

$$D = \frac{K\lambda}{\beta Cos\theta} \tag{2.02}$$

$$\beta Cos\theta = \frac{K\lambda}{D} + 4\varepsilon Sin\theta \tag{2.03}$$

where D is the average crystallite size, K is shape factor (typically~0.94), λ is the X-ray wavelength (1.540 Å, for CuK_α radiation), ε is the microstrain, β is the FWHM and θ is the Braggs diffraction angle. Since, the FWHM is mainly influenced by small crystallite size as well as microstrain present in the sample. The average crystallite size and lattice strain were estimated using the plot of $\beta Cos\theta/\lambda$ versus $Sin\theta/\lambda$. In this plot, slope represents the microstrain present in the prepared powder sample and reciprocal of y-axis intercept estimate the average crystallite size *(D)* of the material sample.

2.3.2. Rietveld Refinement Study

A number of phase analysis, quantitative methods have been existing based on XRD data. The Rietveld refinement is one of them proposed by Hugo M. Rietveld. It is extensively accepted owing to its whole-pattern fitting tactic in its place of single-peak analysis. Rietveld refinement analysis technique shows the various advantages as it can effectually lessen or abolish the inaccuracies arising from preferred particle statistics, orientation, peaks overlapping, and detection of trace phases. Under "n" iterations, the Rietveld technique

performs a least square fitting analysis to adjust a hypothetical line profile to match the measured profile. A Rietveld refinement software like Full Prof Suite may refine refinement parameters like background, peak form, and lattice parameters. The pseudo-voigt function and the mode of linear interpolation between a set of background points established the peak shape and the backdrop, respectively. The Rietveld refinement is advantageous for quantifiable phase analysis, space group symmetry, residual stress, crystal structure and microstructural analysis.

2.3.3. Fourier Transform Infrared (FT-IR) Spectroscopy

Infrared spectroscopy is an extremely important non-destructive technique for the determination of various existing functional groups in any crystalline or amorphous materials. In any material, the molecular total internal energy is sum of vibrational, rotational and electronic energy levels. In FT-IR spectroscopy, a range of infrared radiations were conceded on a sample. A part of the incident infrared (IR) radiation was absorbed by the sample, while the other part of radiation was transmitted through the sample. The absorbed part of the radiation spectrum mainly depends on the frequencies of vibrations between the bonds of the atoms making up of the sample. Finally, the absorbed/transmitted IR radiation was detected by detector, which producing a unique molecular fingerprint of the sample. Thus, the FT-IR spectroscopy can be used to recognize unknown kind of sample materials. Also, the quantity of functional groups present in sample can be evaluated using the size of the peaks in recorded spectra [117].

The normal FT-IR instrument consist an IR source, interferometer, sample holder, detector, which are connected and commanded by software on a dedicated computer.

Fig. 2.06: *The FT-IR Spectrometer (Perkin Elmer).*

The FT-IR apparatus operates on the basis of the Michelson interferometer technique. [118]. The interferometer is made up of two mirrors that are placed across the beam splitter at an angle to one another. The output beam is the consequence of interference between the reflected beams from both mirrors when one of the mirrors is fixed and moves a set distance from its position. After that, the fast Fourier transform technique is employed to get the material's IR spectrum once the beam has passed through the sample resulting in an interferogram. FT-IR spectra were recorded from FT-IR spectrometers manufactured by Perkin Elmer as demonstrated in Fig 2.06.

2.3.4. Diffuse Reflectance Spectroscopy (DRS)

The DRS is one of the most unique characterization techniques to study the optical phenomenon of powder sample. DRS profile gives the molecular spectroscopic information such absorption, reflectance band of powder sample in the UV to IR regions. Mainly, two kinds of reflection can transpire; first one is specular/regular reflection from smooth, polished surfaces and second one is diffuse reflection from dull or mat surfaces like powders. These kind of external or total internal reflection will provides the spectroscopic information of materials.

Fig. 2.07: *UV-VIS spectrophotometer made by Jasco, model V770*

Opaque sample having nonuniform surface and scattered the incident light in different directions can be characterized using DRS techniques. The DRS profile was recorded by employing spectrophotometer made by Jasco, model V770 as shown in Fig 2.07. The spectrophotometer can be made up of a light source, monochromators, standard reference sample ($BaSO_4$), UV-Vis NIR detector, amplifier and computer with proper software as a recording device. The most widely utilized light sources, spanning the UV to visible radiation range, are tungsten and deuterium lamps. Prisms and slits, which can disperse the primary light source and emit two monochromatic radiation beams with the requisite same wavelength to the sample and reference cell, are typically included in monochromators. The reference solution and the sample solution were both exposed to these two monochromatic radiation beams. The beam from both the sample cell and the reference sample cell can be detected by the two-photocell kind of detector. Since the photocells' signal intensity is so low, the amplifier may magnify the signals many times and provide crisp, recordable data. Computers can serve as recording devices, storing all the data and visualizing the captured spectrum when the appropriate software is used [119].

DRS profile shows the various absorption peaks in different ranges such as UV, visible and near IR, which is depending on the sample host and activator ions. On the basis of recorded spectrum, optical bandgap can be estimated via employing the Kubelka-Munk function. The optical (E_g) bandgap was estimated with the support of the following equation [120,121].

$$F(R)h\nu = C\left(h\nu - E_g\right)^n \tag{2.04}$$

where *hν* signifies the incident photon and C is a constant. The *n* defines the type of transition, having values of 1/2 and 2 for direct and indirect allowed transitions, respectively. The Kubelka-Munk function *F(R)* was evaluated [37,122]:

$$F(R) = \frac{(1-R)^2}{2R} = \frac{\alpha}{S} \tag{2.05}$$

In the above equation, α is the absorption coefficient, R taken as reflectance and S is a scattering coefficient. *F(R)* is directly proportional to the absorption coefficient, and *S* is independent of wavelength. A graph plotted between $[F(R)h\nu]^2$ and incident energy $h\nu$ gives the *x* axis intercept via extrapolating the slope to $\alpha = 0$. Then *x* axis intercept is the optical bandgap of the sample.

2.3.5. Scanning Electron Microscope (SEM)

SEM is one of the important electron microscopes used to observe morphology (particles shape, size and arrangement), topography (surface appearance), elemental composition and their degree of disorder of the solid specimen. SEM produces the high-resolution images of a sample by scanning the surface with a focused beam of electrons. The electron signals that originate from electron-sample interactions reveal information about the specimen including crystalline structure, external morphology, and elemental composition of the solid materials [123]. The SEM contains an electron gun as a source of electron, electron

lenses, a sample stage, detectors (secondary electrons, backscattered electrons X-ray detector), vacuum system, and scanning coil as shown in Fig 2.08.

Electrons beam is generated by field emission or thermionic emission process using an electron gun situated at the top of microscope. A generated electron beam is accelerating down in a vacuum with a high electrical field potential gradient and passing through an anode creating a focused beam. These primary electrons beam is deflected and focused by a series of electronic lenses, which produce a fine directional electron beam. The sample is situated on a

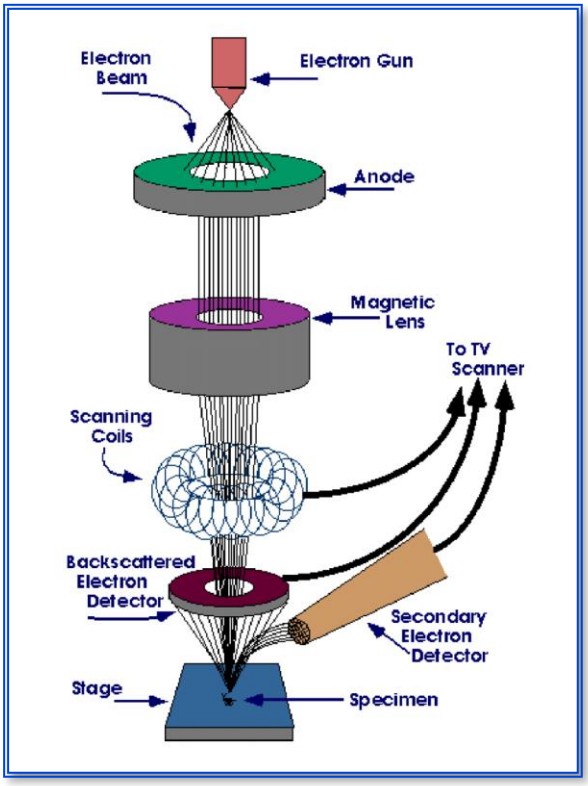

Fig. 2.08: *Schematic diagram for SEM* ***Fig. 2.09:*** *SEM, Zeiss EVO MA-10*

stage in the chamber of the microscope before a vacuum is created in the chamber via vacuum pumps. The position of the electron beam above the objective lens is controlled by scan coils. These coils enable the beam to scan across the sample's surface while collecting data for a specific spot. A variety of signals, including secondary electrons, backscattered electrons, and

distinctive X-rays, are produced as a result of the interaction between electron, and sample. These signals are then collected by detectors and converted into an electrical signal. Imaging can be visualized using an electronic signal in one of two ways: the first uses a secondary electron signal that has been detected, and the second uses backscattered electrons. On the cathode ray tube, electronic signal data was gathered and presented on a computer monitor. Computers with appropriate software can serve as recording devices, saving all the information and displaying the specimen's microscopic image [124].

2.3.6. Photoluminescence Spectroscopy

Any light-sensitive substance, such as powder, liquid, glass, or thin-film samples, can have its photoexcitation and emission measured using the versatile, non-destructive, and contact-free PL spectroscopy approach. PL studies have been recognized as one of the most sensitive and commonly employed tactics of exploring the optical properties of materials, such as luminescence of impurities, band structures, absorption, and point defects with high accuracy. The sample is typically exposed to a range of light beams, some of which are absorbed, excited the samples' ions and de-excited by releasing radiative emission, preferably in the visible region, along with some non-radiative relaxations [125,126]. PL spectroscopy is a powerful technique to examine transition and radiative/non-radiative recombination's of carrier ions in light influenced materials. PL spectroscopy can offer applicability in the fields of molecular electronics, environmental sciences, medical diagnostics, industries, day to day life devices and cell biology.

The PL spectrofluorophotometer comprises an excitation light source, monochromator, sample cell, a number of lenses, photodetector, amplifier etc. and connected with computer, which operates and records the experiential spectrum as demonstrated in Fig 2.10. The source

of excitation employed should give continuum spectrum in the desired wavelength range. Xenon lamp can provide a moderately continuous light output and used as light source, which emits light in 220-800 nm range. The emitted light beam is passing through the monochromator. The Most common type of monochromators employs a diffraction grating. Monochromator employs diffraction grating i.e., collimated light illuminates a grating and leave with a different angle depending on the wavelength. The monochromator can then be adjusted to select which wavelengths to transmit. Excitation monochromator is to select the particular wavelength of light from the incident beam. A portion of incident light is absorbed by the sample, and emits light in all directions. Angle of 90° is chosen for emitted light and some of the light passes through the emission monochromator and reaches detector. The emitted light sensed by the photomultiplier tube as a detector. Detector can be a single-channel (senses only one wavelength at a time) or multichannel (detects all emitted wavelengths). All the components were handled and commanded with the help of dedicated software in a computer system. Finally, the detected spectrum was amplified using the photomultiplier tube, and then converted in a signal form and recorded by the computer for further investigation. The computer screen displays the recorded spectrum in terms of intensity as a function of the wavelength of emitted light.

PL is the physical phenomena in which emission of light from material under the excitation of various wavelength of light sources. The PL characteristics were recorded by Shimadzu, RF-5301PC spectrofluorophotometer equipped with 150-watt Xenon lamp as a source of excitation as depicted in Fig 2.11. To record the PL characteristics, initially sample holder is completely filled with prepared phosphor, placed at appropriate position in the path of incident source of excitation beam. The excitation and emission spectra were measured by

selecting the appropriate emission/excitation wavelength with scan mode at a medium scan rate, slit width at 0.1 nm and high voltage PMT setup.

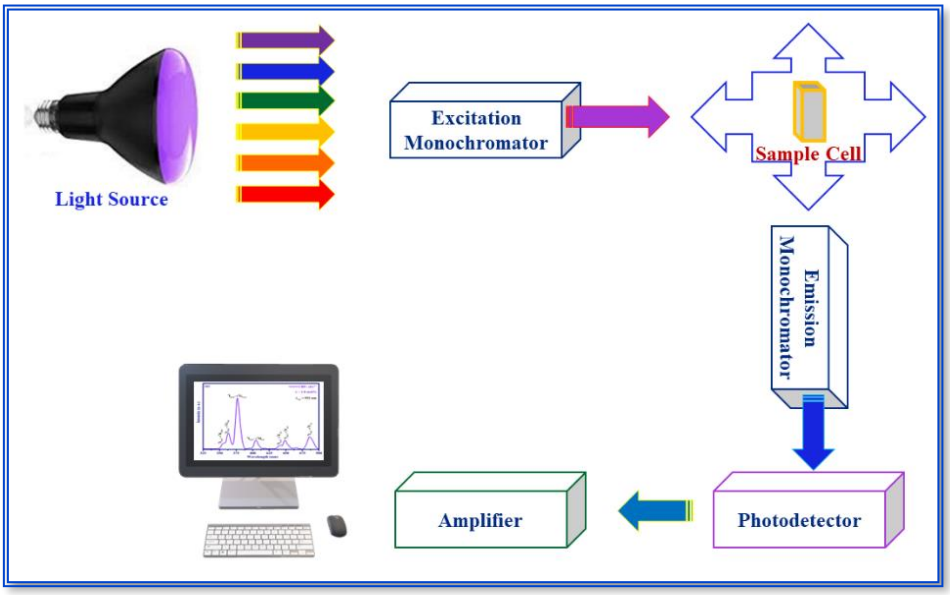

Fig. 2.10: *Schematic representation of PL spectrofluorophotometer.*

Fig. 2.11: *Shimadzu, RF-5301PC spectrofluorophotometer connected with computer.*

The excitation profile is obtained by scanning a certain range of wavelengths while monitoring a definite and fixed emission wavelength. The emission spectra will also be recorded using the bands that were seen in the excitation spectrum. Finally, software displays the spectrum with plot between the intensity of emitted light and wavelength.

2.3.7. Time-Resolved Photoluminescence (TRPL) Spectroscopy

TRPL is one of the most preferable tools for studying fast/slow electronic deactivation processes that result in the emission of photons from particular energy levels in the luminescent materials under certain source of excitation, a process called PL decay time or lifetime. The PL lifetime is an intrinsic property of a luminescent material, which provides the clear understanding of the material excited state dynamics. The PL lifetime of any luminescent materials can be influenced by the molecular environment such as presence of ions, solvent, temperature, quenchers as well as interactions with other molecules. PL lifetime variations can therefore provide evidence about the local chemical environment of the materials.

The important components of TRPL are the pulsed light source (Xenon flash lamp, pulsed laser), an excitation and emission monochromators, single-photon sensitive detector, handled by computer with the dedicated software. A fast photodetector is used for recording the emission of a sample as a function of time while it is being excited by a specific pulse light source. This technique can be used to keep track of the quality of the material, identify spectral emissions with distinct emissive states, or investigate how energy is transferred from one constituent to another in mixed composites and samples. The recorded lifetime is an intrinsic characteristic of PL properties that can provide insight into the excited state dynamics [127,128].

The PL lifetime curve was recorded at room temperature by Edinburgh FLSP920 and Horiba Scientific-FluoroLog3 as seen in Fig 2.12. Microsecond Xenon flash lamp source and single photon count photomultiplier tube detector were attached with the instrument.

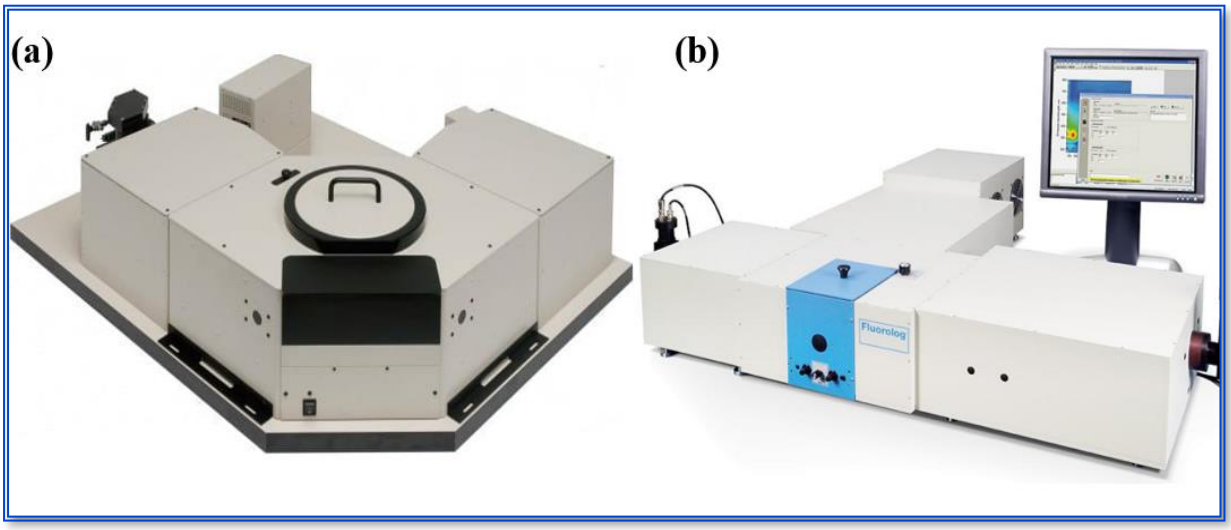

Fig. 2.12: *TRPL spectrofluorophotometer (a) Edinburgh FLSP920 and (b)Horiba Scientific-FluoroLog3.*

The PL lifetime curves were fitted with different exponential equations. It can be observed that all the decay curves were fitted biexponentially with the following equation [129,130]:

$$I(t) = I_o + A_1 exp\left(-\frac{t}{\tau_1}\right) + A_2\, exp\left(-\frac{t}{\tau_2}\right) \quad (2.06)$$

where $I(t)$ and I_o signify the luminescence intensities at time t and 0, respectively. A_1 and A_2 are fitting constant. τ_1 and τ_2 represent the rapid and slow decay lifetimes for exponential mechanisms. The average value of the decay time for samples was evaluated from the given formula [131]:

$$\tau_{avg} = \frac{A_1\tau_1^2 + A_2\tau_2^2}{A_1\tau_1 + A_2\tau_2} \quad (2.07)$$

The PL lifetime for the RE ions doped luminescent materials usually ranges from a few microseconds up to milliseconds.

2.3.8. Temperature Dependent Photoluminescence (TDPL) Spectroscopy

TDPL is one of the most effective, fundamental and influential optical feature investigation tools, extensively used to examine localized states, thermal stability and carrier transport in semiconductor or luminescent materials. In TDPL spectroscopy, PL spectra of the prepared luminescent materials have been caried out at different temperatures and find out the change in PL characteristics with rise or fall in temperature. Based on the PL spectra caried out at different temperatures, a methodological theory has been established to examine the thermal stability, defects related to nonradiative transitions and carrier transport dynamics.

The important components of TDPL spectrofluorophotometer are the light source (Xenon lamp, laser), monochromator, temperature-controlled sample holder, photodetector and computers with the dedicated software as represented in Fig 2.13. A Xenon lamp is used as a light source, which emits light in 200-800 nm range. The emitted beam of light is passes through the monochromator, which can select the desired wavelength of light used for excitation. The selected wavelength incident on the temperature-controlled sample holder via optical fiber. Luminescent sample emits light under particular excitation wavelength, which can be passed through another optical fiber and detected by photodetector. Finally, the detected spectrum was recorded by computer for further process. In the current research work, the TDPL features of the prepared phosphors are recorded by employing Ocean Optics FLAME-S-XR1-ES spectrofluorophotometer as demonstrated in Fig 2.14.

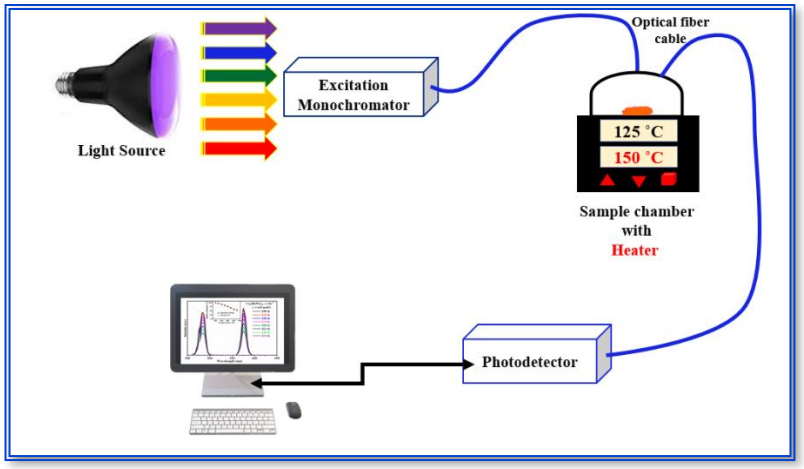

Fig. 2.13: *Schematic representation of TDPL spectrofluorophotometer.*

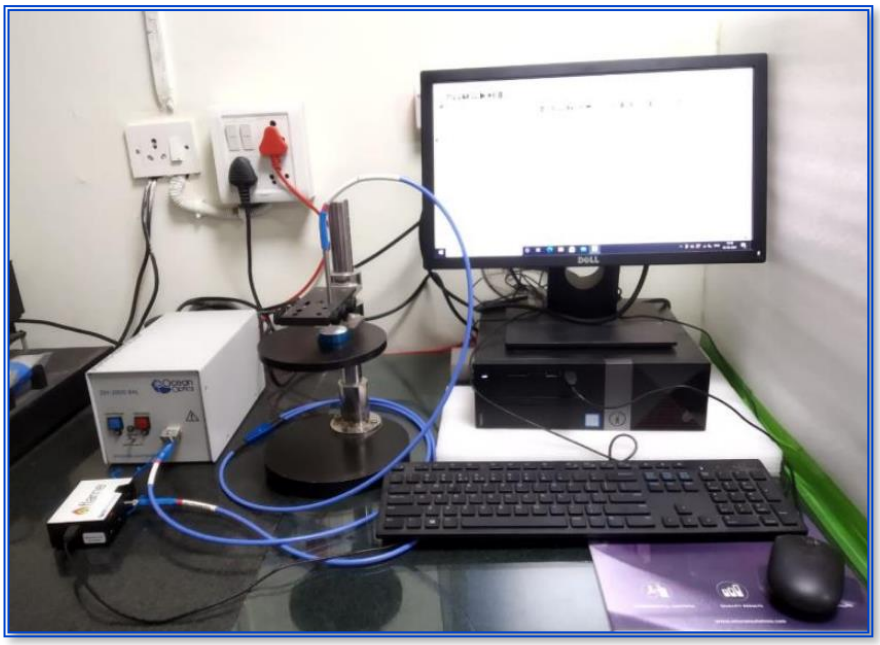

Fig. 2.14: *TDPL characterization setup with ocean Optics spectrofluorophotometer*

In TDPL data, the emission intensity of luminescent materials under certain source of excitation wavelength can be increased/decreased with elevated temperatures. The effect of temperature on the photoluminescence properties of phosphor materials is one of the significant features of the applicability of phosphor in many photonic applications. Typically, phosphors are used in lighting devices require high thermal stability as the UV/blue LED chips generate

temperature around 120 to 150 °C while operating time. Also, the thermal quenching features of the phosphor can be used as temperature sensor.

Based on TDPL spectra recorded at elevated temperatures, a methodological theory has been established to examine the thermal stability of luminescent materials. The activation energy (ΔE) is one of the crucial parameters for the phosphor to identify the thermal stability of luminescent materials, which was reckoned using the Arrhenius equation as [132]:

$$I_T = \frac{I_o}{1+C\ exp\left(-\frac{\Delta E}{k_B T}\right)} \tag{2.08}$$

here I_0 and I_T represents the PL intensity at initial or room temperature and at a specific temperature *T (K),* respectively. C and k_B signify an arbitrary constants and the Boltzmann constant, respectively. As per the Arrhenius equation, the activation energy (ΔE) was assessed on the basis of linear fitted slope among $ln((I_o/I_T)-1)$ and $1/K_BT$ [121, 133, 134].

CHAPTER 3

Conversion of Blue Emitting $Ca_3Bi(PO_4)_3$ Host as a Color Tunable Phosphor for Luminescent Devices

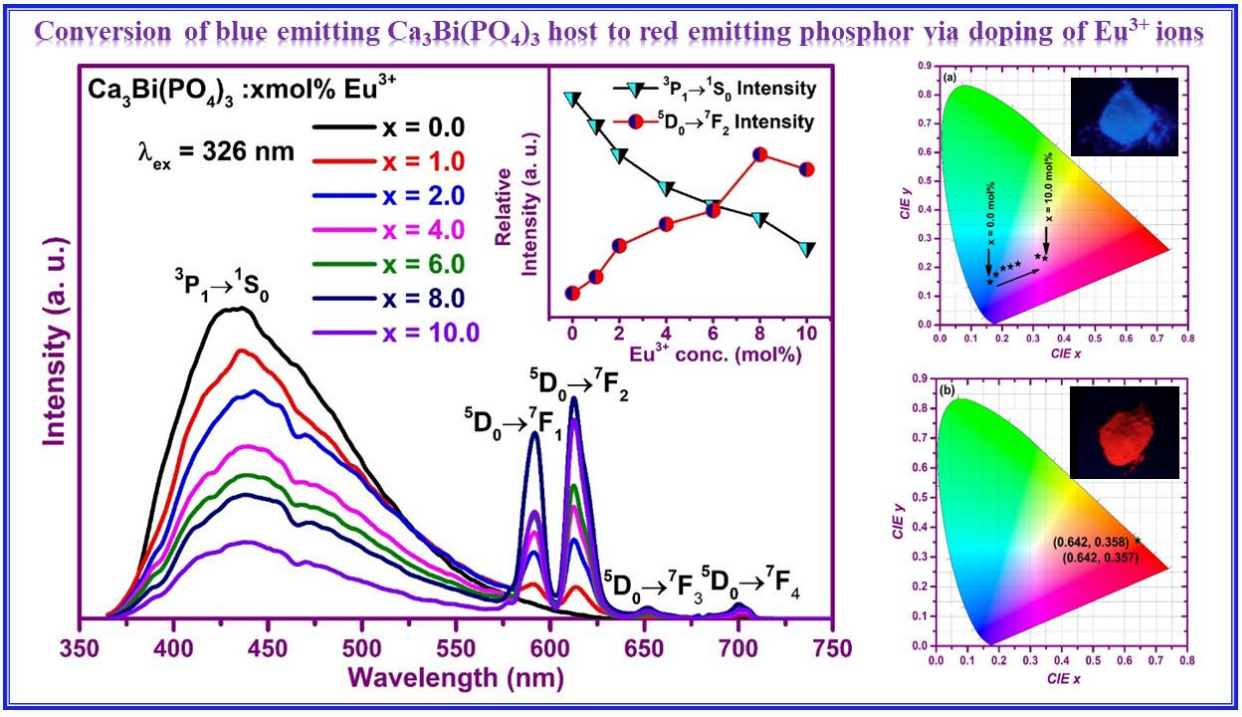

Part of this work has been published in
Journal of Luminescence 227 (2020) 117570 (IF: 4.171)

3.1. Introduction

RE doped crystalline materials have been fascinated with extensive attention among researchers due to the direct usage of these materials in the field of photonic and optoelectronic devices. Nowadays, in the field of lighting, the phosphor-converted white-light-emitting diode (pc-WLED) has become the most essential illuminating device for the next-generation SSL source. The pc-WLED is presently experiencing fast advancement and will soon replace the longstanding incandescent and fluorescent lamps because of the extraordinary merits i.e., more brightness, less energy consumption, high luminous efficiency, small volume, fast switching, robustness, long durability, and environmental friendliness [135–139]. The commercially available pc-WLEDs used as a lighting source, illuminate the bluish-white light with high CCT due to the deficiency of the red color component. Hence, it becomes essential to combine a red phosphor to acquire warm white light for more sophisticated lighting applications [106,140]. Moreover, red emitting phosphor plays a very crucial role in obtaining proper CCT and improving color rendering index value towards attaining the perfect white light source [141]. The commercially available sulfide and nitride based n-UV/blue pumped red phosphors have some disadvantages such as low chemical stability and efficiency as compared with other primary colors [142–144]. Furthermore, LED chips for exciting phosphor generates heat, which affect the luminescent properties of phosphor and degrade emission intensity as well as the performance of the pc-WLEDs [145,146]. Hence, the thermal stability of the luminescent material is one of the most significant factors for assessing the performance of WLEDs. Therefore, it is very much essential to explore and develop a new efficient red illuminating phosphor with better chemical and thermal stability.

Emission and thermally stable characteristics of the phosphor especially depend on the selection of appropriate host materials as well as dopants (RE ions or transition metal ions).

However, the host material chosen to synthesize phosphor may not only acts as a host crystal to hold the dopant ions closely but also has the function of sensitizing their luminescence. Owing to the extreme necessity of the red emitting phosphors for developing SSL devices, especially for WLEDs, various diverse categories of host lattices have been prepared so far. Among all the inorganic host materials, oxide-based host lattices are an excellent choice for numerous applications. Phosphate that possesses numerous crystal structures has been demonstrated to be the potential candidate for the luminescent host, some of which expose exceptional PL properties once doped with activator ions [56,87,147–149]. Among the various phosphate hosts, eulytite-type orthophosphate is considered to be the suitable host lattice, having general formula $A_3B(PO_4)_3$, where A is divalent alkaline earth and B is trivalent ions (typically Bi, Y, In or RE ions). Eulytite-type orthophosphate possesses a large bandgap, high thermal and chemical stability with high solubility of RE ions [90,140,150]. Scientists across the world pay more attention to explore the optical properties of the eulytite-type orthophosphate due to its low phonon energy, stable crystal structure, water-resistant property, and excellent optical properties [91,151,152]. Calcium-based eulytite-type phosphate [$Ca_3Bi(PO_4)_3$] is one of the potential phosphor hosts used in display devices, mercury-free lighting and laser materials [86,92]. $Ca_3Bi(PO_4)_3$ is proposed as an admirable host for luminescent materials and various RE ions doped $Ca_3Bi(PO_4)_3$ phosphor have been synthesized via different routes for luminescent devices applications [91,92].

RE ions usually exist in a trivalent/divalent state and demonstrated with a series of excitation and emission bands due to their definite $(f - f)$ energy levels having an excellent radiative recombination rate. RE ions usually exist in trivalent/divalent state. Among all the RE ions, Eu^{3+}/Eu^{2+} play as one of the most important activators for tremendous applications in

photoluminescence, electroluminescence, biomedical applications and optical storage due to its high luminescence efficiency and various energy levels [153–155].

In this chapter, $Ca_3Bi(PO_4)_3$ activated with Eu^{3+} ions have been prepared through a SSR method. The crystallinity, structural properties, particle size and morphology and PL characteristics were explored in detail. The optical bandgap of $Ca_3Bi(PO_4)_3$ has been examined with the help of a diffuse reflectance spectrum using the Kubelka-Munk function. A broad host excitation as well as emission bands in $Ca_3Bi(PO_4)_3$ were spotted and are corresponding to the transition of Bi^{3+} ions. The color tunability was accomplished in the host via doping of Eu^{3+} ion concentrations. The time resolved PL, CIE chromaticity coordinates, color purity and thermal stability properties of Eu^{3+}activated $Ca_3Bi(PO_4)_3$ phosphor have been explored for the application of near-UV/blue excited lighting devices.

3.2. Experimental Procedure and Characterizations

Eulytite type Eu^{3+} activated $Ca_3Bi(PO_4)_3$ phosphors have been prepared employing SSR method as described in the section 2.2.1. in chapter 2 and detailed flowchart is presented in Fig. 2.02. The highly pure $CaCO_3$, Bi_2O_3, $NH_4H_2PO_4$ and Eu_2O_3 were used as precursor materials for the synthesis of the phosphor. Finally, the prepared Eu^{3+} activated $Ca_3Bi(PO_4)_3$ phosphors have been characterized and analyzed using various tools.

3.3. Results and Discussion

3.3.1. Crystallinity and Structural Analysis

The crystalline phase purity and structure of un-doped and doped samples were examined by XRD patterns. Fig. 3.01 (a-d) illustrates the XRD patterns of standard JCPDS data, un-doped and Eu^{3+} doped $Ca_3Bi(PO_4)_3$ powders. It was found that all the peaks were indexed and well-matched with the patterns of JCPDS card No. 085-2447. A comparison between the as-

synthesized sample and standard data has been revealed that $Ca_3Bi(PO_4)_3$ has a cubic structure with $I\bar{4}3d$ (220) space group. Four highest peaks were indexed as (310), (321), (442) and (431) crystallographic planes, which were detected at 2θ values of 28.2°, 33.5°, 44.4° and 46.3°, respectively. The diffraction patterns of the Eu^{3+} doped $Ca_3Bi(PO_4)_3$ sample are also in good agreement with the JCPDS data, without any impurity peaks, which confirms that Eu^{3+} ion successfully incorporated in the host lattice. In $Ca_3Bi(PO_4)_3$ host lattice, Eu^{3+} ions occupied the Bi^{3+} sites due to the fact that the effective ionic radii of Eu^{3+} ions (r = 0.94 Å for VI coordination number) are slightly smaller than the ionic radii of Bi^{3+} (r = 1.03 Å for VI coordination number) ions and also the valence states of both ions are the same [91].

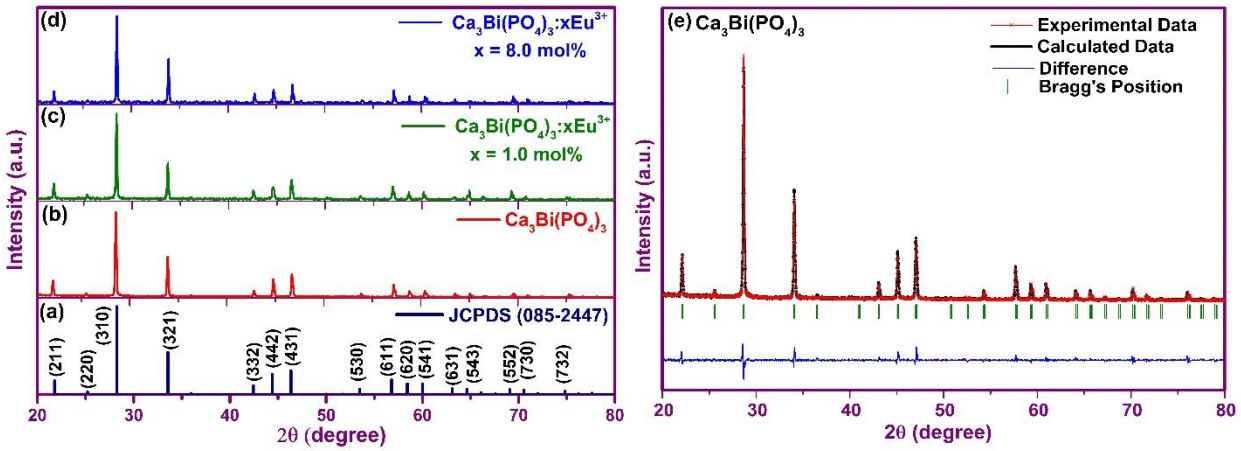

Fig. 3.01: *Diffraction patterns of (a) standard JCPDS (85-2447) data (b) undoped $Ca_3Bi(PO_4)_3$ sample (c) x = 1.0 mol% (d) x = 8.0 mol% Eu^{3+} doped $Ca_3Bi(PO_4)_3$ powder samples and (e) Rietveld refinement plot of un-doped $Ca_3Bi(PO_4)_3$ sample.*

The average crystallite size (D) for $Ca_3Bi(PO_4)_3$ and Eu^{3+} activated $Ca_3Bi(PO_4)_3$ were calculated with the help of the Debye-Scherer equation. The Debye-Scherer equation is as depicted in equation number 2.02 in section 2.3.1 [115]. The crystallite size is in the range of 55 to 60 nm for the un-doped and Eu^{3+} (x= 1.0 & 8.0 mol%) doped $Ca_3Bi(PO_4)_3$ samples.

To examine the phase and crystal structure of the as-synthesized $Ca_3Bi(PO_4)_3$ compound, the Rietveld refinement has been performed as represented in Fig. 1 (e). The essential unit cell parameters for the Rietveld refinement, the structure data of $Ca_3Bi(PO_4)_3$ (Pearson's Crystal Data, Powder pattern: 1630538) have been employed in the refinement process. The red solid with cross and black line with a dot refers to the experimental and calculated data patterns, respectively. The green short vertical lines express the Bragg angles (2θ) for $Ca_3Bi(PO_4)_3$. The blue line represents the difference between calculated and experimental patterns. Finally, the crystal structure parameters have been refined. The calculated refined lattice parameters $\alpha = \beta = \gamma$ and a = b = c were 90° and 9.873 Å, which are matched well with the standard data [90]. The structural refinement pattern approves the pure phase formation of cubic structured $Ca_3Bi(PO_4)_3$ samples without any secondary phase and the obtained goodness of fit (χ^2) was found to be 1.93.

3.3.2. Morphological Study

The exterior morphology of $Ca_3Bi(PO_4)_3$ was shown in Fig. 3.02. The SEM micrograph implies the irregular morphology of $Ca_3Bi(PO_4)_3$ powder sample. The particle size was found to be in the μm range. The micron-size phosphor particles have been considered as more convenient for the use in phosphor converted WLEDs [156].

3.3.3. Optical Bandgap Measurement

The diffuse reflectance spectrum of $Ca_3Bi(PO_4)_3$ was recorded at RT as illustrated in Fig. 3.03. The sample $Ca_3Bi(PO_4)_3$ exhibit peak at 326 nm due to characteristic transitions from $^4I_{15/2}$ level to various higher energy levels of Bi^{3+} ions. The optical (E_g) bandgap of $Ca_3Bi(PO_4)_3$ was estimated with the support of the equation as described in equation number 2.04 and 2.05 in section 2.3.4 [120,121].

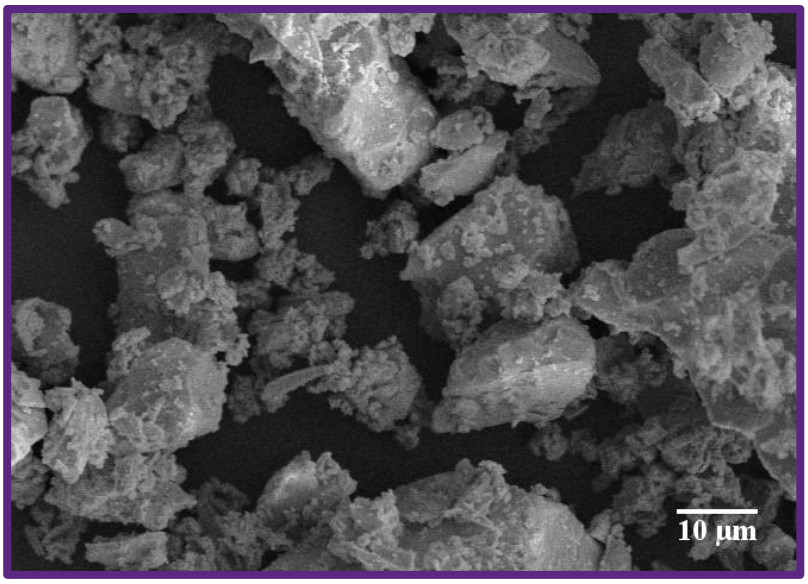

Fig. 3.02: *SEM micrograph of un-doped $Ca_3Bi(PO_4)_3$ sample*

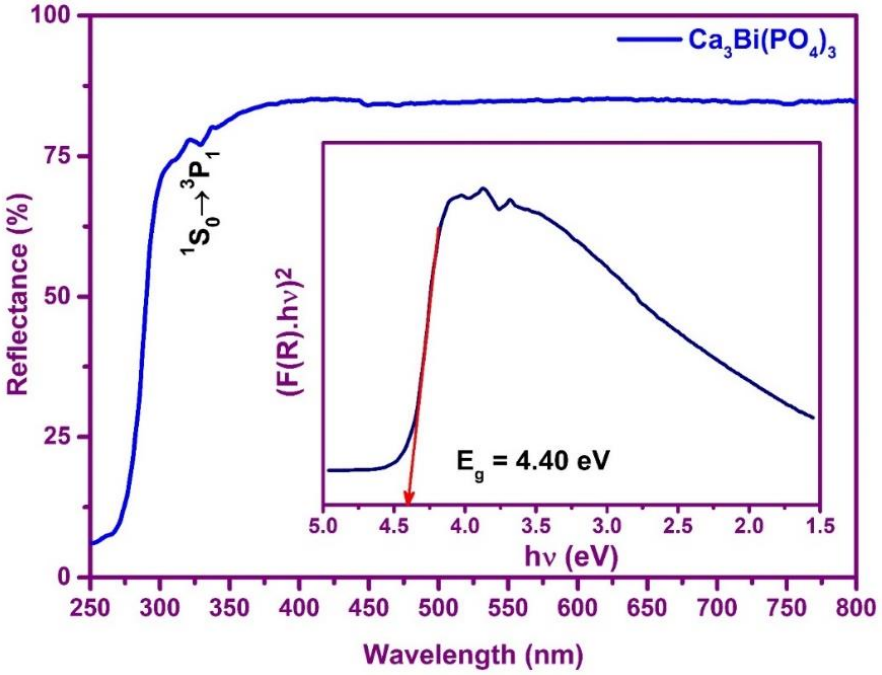

Fig. 3.03: *Diffuse reflectance spectrum of $Ca_3Bi(PO_4)_3$ sample. Inset image displays the assessment of the direct optical band gap using Kubelka-Munk plot of $Ca_3Bi(PO_4)_3$ sample.*

A graph plotted between $[F(R)h\nu]^2$ and incident energy $h\nu$ as shown in the inset of Fig. 3.03. The direct E_g of $Ca_3Bi(PO_4)_3$ was calculated via extrapolating the slope to $\alpha = 0$, which is found to be about 4.40 eV.

3.3.4. PL Properties of $Ca_3Bi(PO_4)_3$ Host and Eu^{3+} Doped $Ca_3Bi(PO_4)_3$ Phosphor

To investigate the PL properties of luminescent materials, it is crucial to recognize the excitation as well as emission wavelength. The excitation spectrum of $Ca_3Bi(PO_4)_3$ was recorded at RT by monitoring the emission at λ_{em} = 434 nm. As illustrated in Fig. 3.04, single broad excitation peak centered at 326 nm was allocated to the $^1S_0 \rightarrow {}^3P_1$ transition of Bi^{3+} ions, which exist in the host lattice [157]. The broad emission spectra of $Ca_3Bi(PO_4)_3$ host under the excitation λ_{ex} =326 nm was observed as shown in Fig. 3.04. This host emission band was in the 350 to 620 nm wavelength range, centered at 434 nm ascribed to the $^3P_1 \rightarrow {}^1S_0$ electronic transition of Bi^{3+} ions [158].

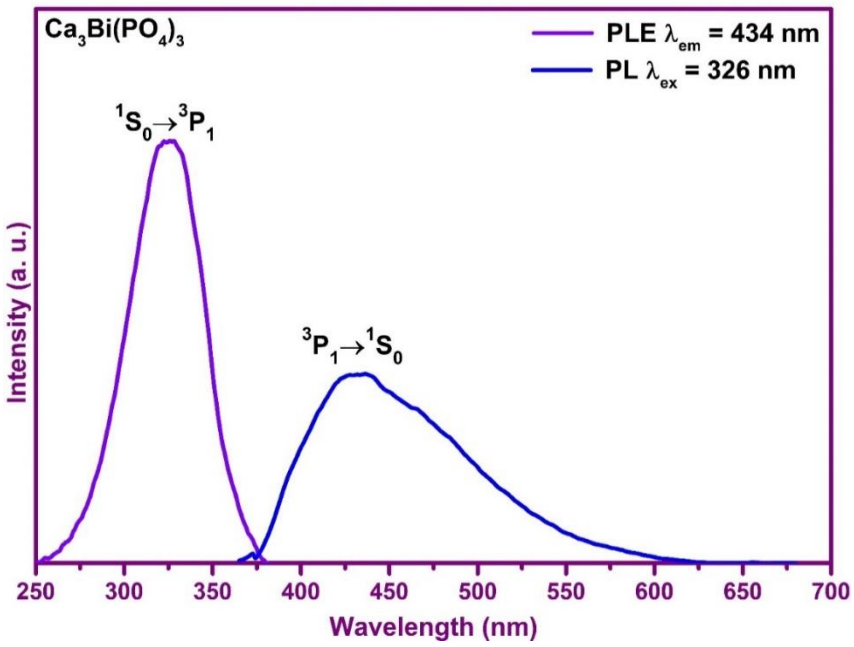

Fig. 3.04: *PLE spectrum of $Ca_3Bi(PO_4)_3$ host at λ_{em} = 434 nm emission and PL spectrum of $Ca_3Bi(PO_4)_3$ host at λ_{ex} = 326 nm excitation wavelength.*

PL excitation spectrum for the as-synthesized Eu^{3+} (x = 1.0 to 10.0 mol%) doped $Ca_3Bi(PO_4)_3$ phosphor has been recorded at RT. For the identification of the excitation peak, PLE spectrum was scanned in 350-500 nm wavelength range. During the excitation spectrum recording process, the emission wavelength was fixed at 612 nm as illustrated in Fig. 3.05 (a). The spectra consist of numerous peaks placed at 317, 362, 382, 393, 416 and 465 nm attributed to the transition from $^7F_0$ ground state to different excited states $^5H_6$, $^5D_4$, $^5L_7$, $^5L_6$, $^5D_3$ and $^5D_2$ of the Eu^{3+} ions, respectively. Among these peaks, two intense peaks were observed in n-UV at 393 nm and blue light at 465 nm, ascribed to ($^7F_0 \rightarrow {}^5L_6$) and ($^7F_0 \rightarrow {}^5D_2$) distinct transitions of Eu^{3+} ions. The PLE spectrum confirms that the Eu^{3+} doped $Ca_3Bi(PO_4)_3$ phosphor can be efficiently excited using n-UV (393 nm)/blue light (465 nm).

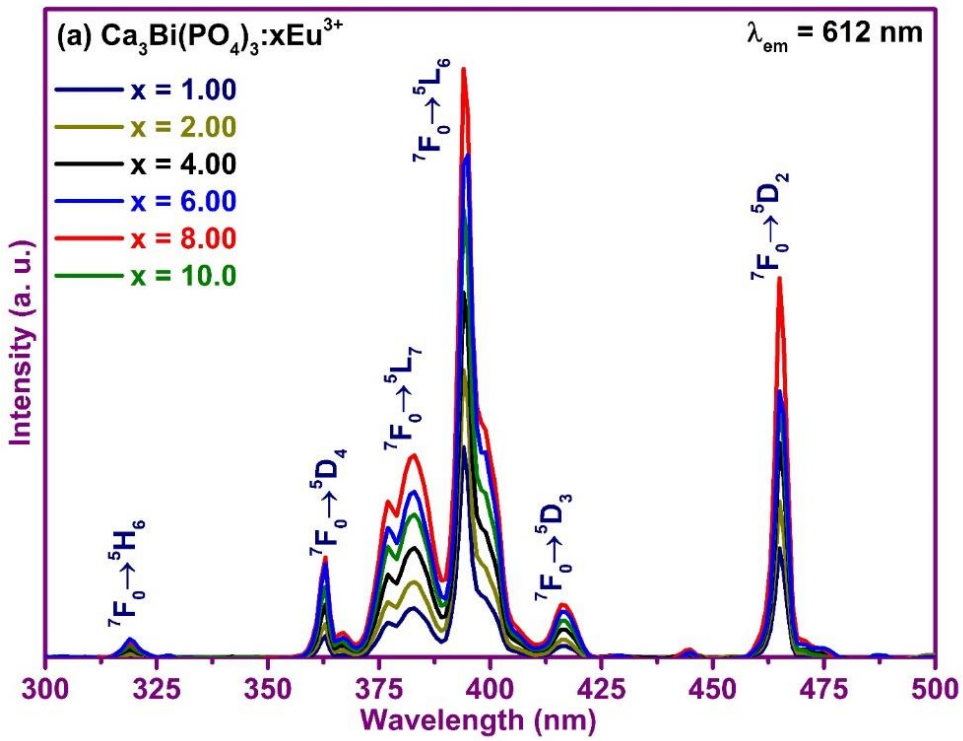

Fig. 3.05: *(a) PLE spectra of doped $Ca_3Bi(PO_4)_3$: x Eu^{3+} (1.0 to 10.0 mol%) phosphors recorded at λ_{em} = 612 nm.*

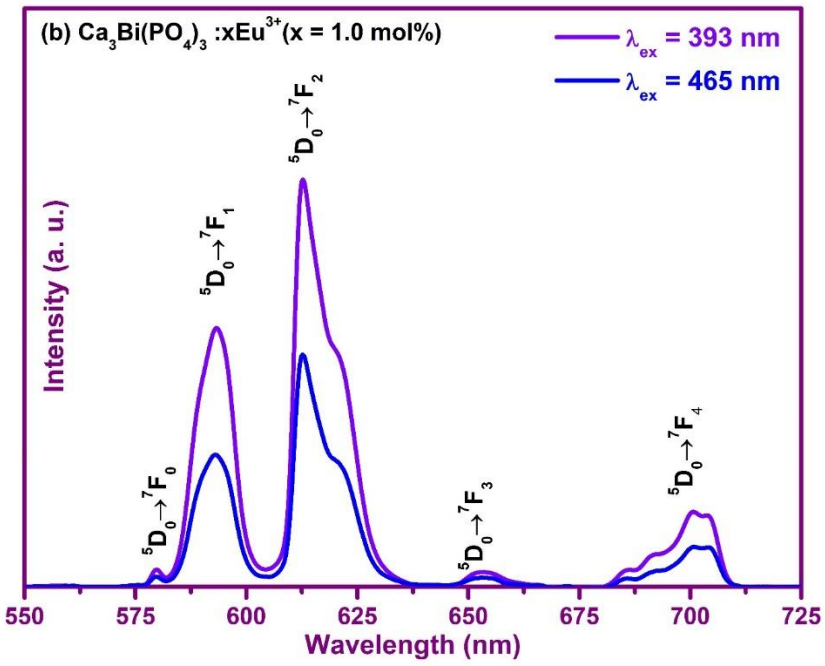

Fig. 3.05: *(b) PL spectra of $Ca_3Bi(PO_4)_3$: x Eu^{3+} (x= 1.0 mol%) phosphors recorded at λ_{ex} = 393 & 465 nm.*

PL spectra have been recorded for Eu^{3+} (x = 1.0 mol%) doped $Ca_3Bi(PO_4)_3$ phosphor at excitation wavelengths (λ_{ex}) = 393 and 465 nm as presented in Fig. 3.05 (b). The PL spectra comprise of five main emission peaks from 550 to 725 nm wavelength range. The detected peaks arise due to the transitions from the lowest energy level $^5D_0$ to different excited ^7F_J (J =*0, 1, 2, 3* and *4*) levels of Eu^{3+} ions [156]. The dominant peak was detected in the range 604-640 nm centered at 612 nm ascribed to $^5D_0 \rightarrow {}^7F_2$ transition of Eu^{3+} ion. Transition, $^5D_0 \rightarrow {}^7F_2$ is owing to the forced electric dipole (ED) transition. On the other hand, peak at 593 nm ($^5D_0 \rightarrow {}^7F_1$) is owing to the magnetic dipole (MD) transition of Eu^{3+} ion. The forced ED i.e. $^5D_0 \rightarrow {}^7F_2$ transition was hypersensitive, which is efficiently influenced by the surrounding ions. The ratio of integrated red to orange emission intensity (ED/MD) is noted as the asymmetric ratio (R_{21}) and identifies the site symmetry of activator (Eu^{3+}) ions. The R_{21} was signified as [130]:

$$R_{21} = \frac{\int_{604}^{640} R_2 d\lambda}{\int_{582}^{604} R_1 d\lambda} \quad (3.01)$$

The R_{21} ratios for the phosphor are 1.711 and 1.831 at λ_{ex} = 393 and 465 nm, respectively. The high R_{21} value indicates high asymmetric around Eu^{3+} ions and red emission intensity is leading over orange red emission intensity. It may be due to the Eu^{3+} ions are placed at a low symmetry site with no inversion center.

Fig. 3.06 demonstrated the PL spectra of host and Eu^{3+} (x = 1.0 to 10.0 mol%) doped $Ca_3Bi(PO_4)_3$ phosphor under the 326 nm excitation wavelength. When Eu^{3+} doped in $Ca_3Bi(PO_4)_3$, the PL intensity at 434 nm is reduced as compared to the pure host emission and several emission peaks arouse at 591, 612, 653 and 701 nm due to the ($^5D_0 \rightarrow {}^7F_1$), ($^5D_0 \rightarrow {}^7F_2$), ($^5D_0 \rightarrow {}^7F_3$) and ($^5D_0 \rightarrow {}^7F_4$) characteristic transitions of Eu^{3+} ion. [38]. Host PL intensity ($^3P_1 \rightarrow {}^1S_0$) was reduced with an increase in the Eu^{3+} ion doping concentration from 1.0 to 10.0 mol%. At the same time, the PL intensity of the bands originated due to Eu^{3+} ions were enhanced with an increase in Eu^{3+} ion doping concentration and it reaches maximum intensity at 8.0 mol% and further decreases. Inset image displays the change in relative intensities of $^3P_1 \rightarrow {}^1S_0$ and $^5D_0 \rightarrow {}^7F_2$ transitions with Eu^{3+} ion doping concentration. The emission intensity of $^3P_1 \rightarrow {}^1S_0$ transition is reduced with increase in doping concentration of Eu^{3+} ion, whereas $^5D_0 \rightarrow {}^7F_2$ transition intensity is enhanced in $Ca_3Bi(PO_4)_3$ phosphor. Based on the above result, it is suggested that the part of host emission energy was transferred to activator (Eu^{3+}) ions [159].

The PL properties of luminescent materials are very much influenced by the doping concentration of RE ions and it is very crucial to regulate the optimum concentration for application purposes. Hence, a series of Eu^{3+} doped $Ca_3Bi(PO_4)_3$ phosphors with different doping concentrations (1.0-10.0 mol%) have been synthesized and luminescent properties

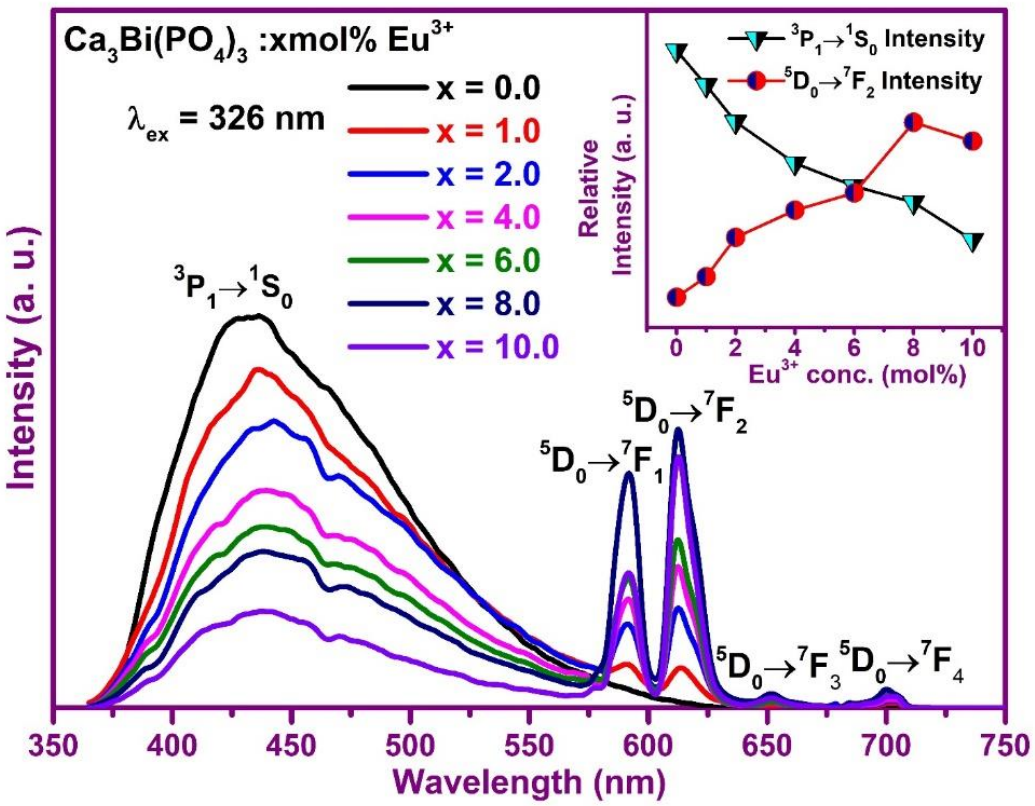

Fig. 3.06: *PL spectra of un-doped and Eu^{3+} (1.0 to 10.0 mol%) doped $Ca_3Bi(PO_4)_3$ phosphor at λ_{ex} = 326 nm. Inset plot shows change in relative intensity of $^3P_1 \rightarrow {}^1S_0$ and $^5D_0 \rightarrow {}^7F_2$ transition with increase in Eu^{3+} ion concentration in $Ca_3Bi(PO_4)_3$ phosphor at λ_{ex} = 326 nm.*

were investigated. Fig. 3.07 (a & b) demonstrated the PL spectra excited at 393 and 465 nm wavelengths. The PL intensity for Eu^{3+} doped $Ca_3Bi(PO_4)_3$ phosphor significantly increases with the doping concentration up to x = 8.0 mol% subsequently, after which the PL intensity was quenched. Inset image of Fig. 3.07 (a & b) confirms the change in PL intensity of $^5D_0 \rightarrow {}^7F_2$ (612 nm) with activator ion concentrations and also shows the quenching of emission. Concentration quenching may arise due to the non-radiative.

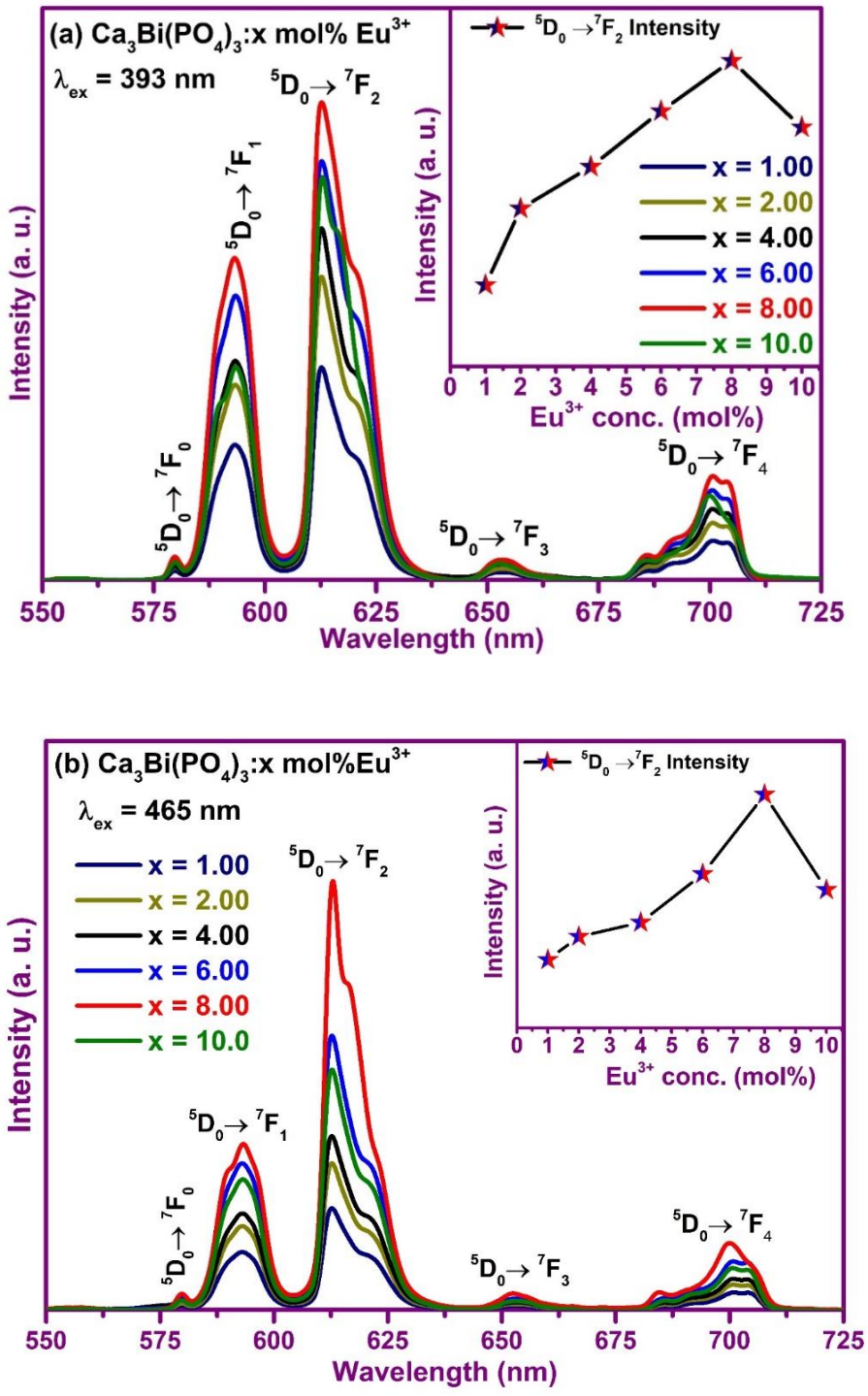

Fig. 3.07: *PL spectra of varying Eu^{3+} ions (1.0, 2.0, 4.0, 6.0, 8.0 and 10.0 mol%) in $Ca_3Bi(PO_4)_3$ phosphors under excitations wavelength (a) λ_{ex} = 393 and (b) λ_{ex} = 465 nm.*

In any host lattice, the distance between the activator ions reduces from certain value is known as critical distance (R_c) when the activator concentration increases over the specific limit, which is the main cause of non-radiative energy transfer among them. The R_c for the Eu^{3+} doped $Ca_3Bi(PO_4)_3$ phosphor was estimated by the following expression formulated by Blasse as described in equation number 1.01, section 1.3.3 of chapter 1 [63]. The R_c for Eu^{3+} doped $Ca_3Bi(PO_4)_3$ phosphor was found to be 19.64 Å, which is higher than 5 Å for exchange interaction. Thus, electric multipolar interaction is the cause of the non-radiative energy transfer between the closest activator ions. Further, the electric multipolar interaction is categorized in three ways, dipole-dipole, dipole-quadrupole and quadrupole-quadrupole. The way in which multipolar can be examined is given by Dexter's theory, which relates PL intensity ***I*** with the mole fraction of activator ion concentration ***x***, formulized and reduced as defined in equation number 1.02, section 1.3.3 of chapter 1 [67,68].

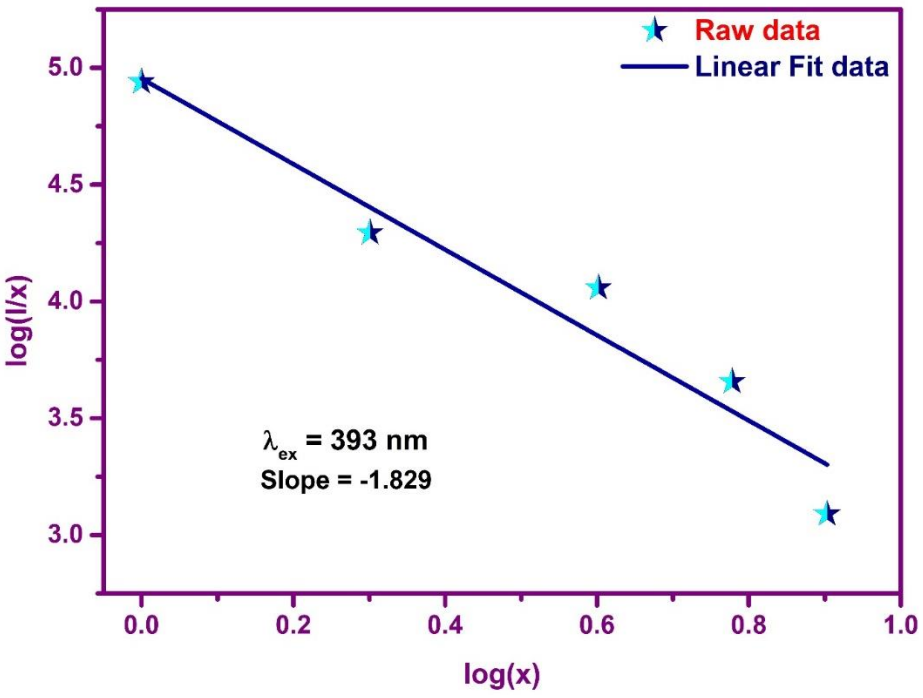

Fig. 3.08: *Dexter plot graph between log (I/x) with log(x).*

The Q value has been predicted by with the help of slope from linear fitted graph between $log(I/x)$ and $log\ (x)$. Fig. 3.08 illustrated $log(I/x)$ verses $log\ (x)$ graph having slope of -1.829, which is equal to $-Q/3$ value. Hence, Q value is found to be 5.487 that is nearby to 6. The Q value in the present work supports that the non-radiative energy transfer between the nearest Eu^{3+}activator ions is due to the dipole-dipole type of interaction.

3.3.5. CIE Calculations and Analysis

PL spectra recorded for un-doped and Eu^{3+} doped $Ca_3Bi(PO_4)_3$ phosphor under excitations of 326, 393 and 465 nm have been used to calculate CIE coordinates, as listed in Table 3.1. The CIE coordinate values for un-doped $Ca_3Bi(PO_4)_3$ at λ_{ex} = 326 nm was lie in the blue region and shifted towards the red region with an increase in Eu^{3+} ion doping concentration, as presented in Fig. 3.09 (a). The result confirms that the CIE color coordinates were tuned via doping of Eu^{3+} ion in $Ca_3Bi(PO_4)_3$ phosphor at λ_{ex} = 326 nm excitation wavelength. The CIE coordinate values for 8.0 mol% Eu^{3+} doped $Ca_3Bi(PO_4)_3$ phosphor at 393 and 465 nm excitation are (0.642, 0.358) and (0.642, 0.357), respectively as presented in Fig. 3.09 (b), which is in proximity with red emitting Y_2O_2S: Eu^{3+} phosphor (0.622, 0.351) and NTSC (0.670, 0.330).

Table 3.1: CIE color coordinates, CCT values of un-doped and Eu^{3+} doped $Ca_3Bi(PO_4)_3$ phosphors.

$Ca_3Bi(PO_4)_3$:xEu^{3+}	CIE (x, y) at λ_{ex} =			CCT (K) at λ_{ex} =	
	326 nm	393 nm	465 nm	393 nm	465 nm
x = 0.0 mol%	0.161, 0.150	-	-	-	-
x = 1.0 mol%	0.180, 0.175	0.642, 0.357	0.633, 0.365	2311	2094
x = 2.0 mol%	0.203, 0.197	0.642, 0.358	0.644, 0.355	2283	2377
x = 4.0 mol%	0.227, 0.202	0.644, 0.356	0.644, 0.357	2367	2338
x = 6.0 mol%	0.251, 0.213	0.641, 0.358	0.640, 0.359	2277	2256

x = 8.0 mol%	0.315, 0.238	0.642, 0.358	0.642, 0.357	2289	2318
x = 10.0 mol%	0.318, 0.232	0.644, 0.355	0.637, 0.362	2374	2170

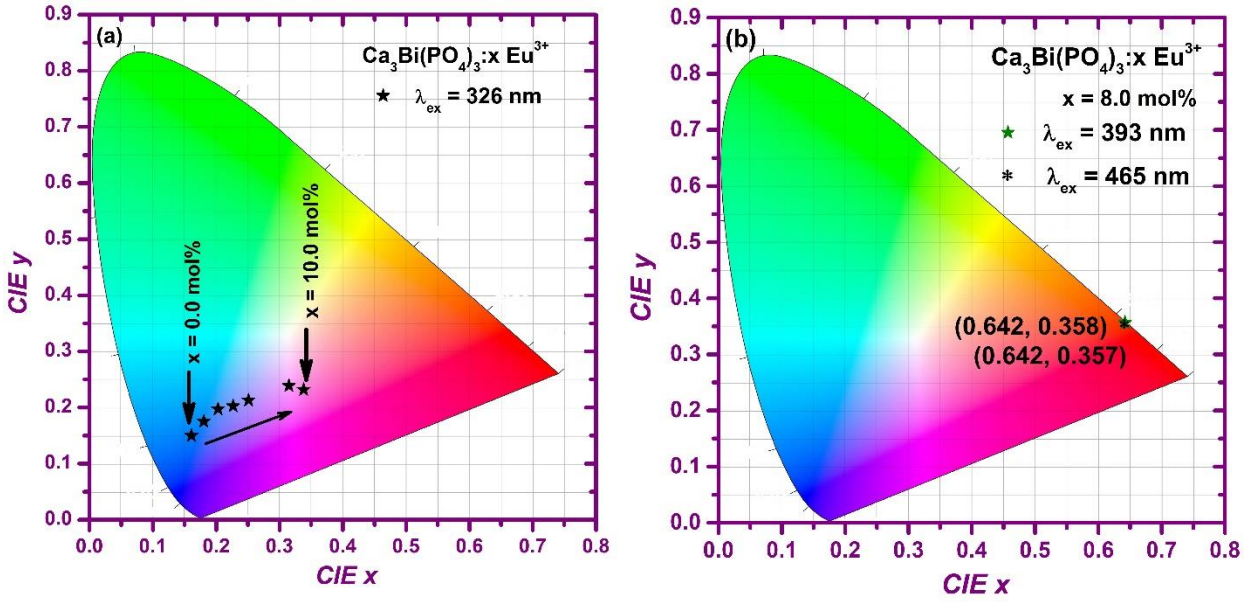

Fig. 3.09: *(a) CIE chromaticity diagram for Eu^{3+} (0.0, 1.0, 2.0, 4.0, 6.0, 8.0 and 10.0 mol%) doped $Ca_3Bi(PO_4)_3$ phosphor at λ_{ex} = 326 nm. (b) CIE chromaticity diagram of 8.0 mol% Eu^{3+} doped $Ca_3Bi(PO_4)_3$ phosphor at λ_{ex} = 393 & 465 nm.*

The CCT values for Eu^{3+} (1.0-10.0 mol%) doped $Ca_3Bi(PO_4)_3$ phosphors have been calculated by employing the McCamy's polynomial formula, which are listed in Table 3.1 [70,160]. The results recommended that Eu^{3+} doped $Ca_3Bi(PO_4)_3$ phosphor can be utilized as a red constituent in warm white LEDs. The color purity was calculated by formula as given bellow [147]:

$$Color\ Purity = \sqrt{\frac{(x-x_{ee})^2+(y-y_{ee})^2}{(x_d-x_{ee})^2+(y_d-y_{ee})^2}} \qquad (3.02)$$

from the above equation, (x, y) signifies the CIE coordinates for Eu^{3+} (x= 8.0 mol%) doped $Ca_3Bi(PO_4)_3$ phosphor, (x_{ee}, y_{ee}) denote the CIE color coordinates for standard white point

and (x_d, y_d) are denotes the CIE coordinates for the dominant wavelength point. The color purity for Eu^{3+} (x= 8.0 mol%) doped $Ca_3Bi(PO_4)_3$ phosphor is found to be 99.03% under 393 nm excitation wavelength. The high percentage of color purity indicates that the Eu^{3+} (x= 8.0 mol%) doped $Ca_3Bi(PO_4)_3$ phosphor can be utilized as a probable red emitting component in WLEDs under the n-UV/blue excitations.

3.3.6. PL Decay Study

PL decay curve has been recorded for the Eu^{3+} (x= 8.0 mol%) doped $Ca_3Bi(PO_4)_3$ phosphor under λ_{em} = 612 nm and λ_{ex} = 393 nm at RT as shown in Fig. 3.10.

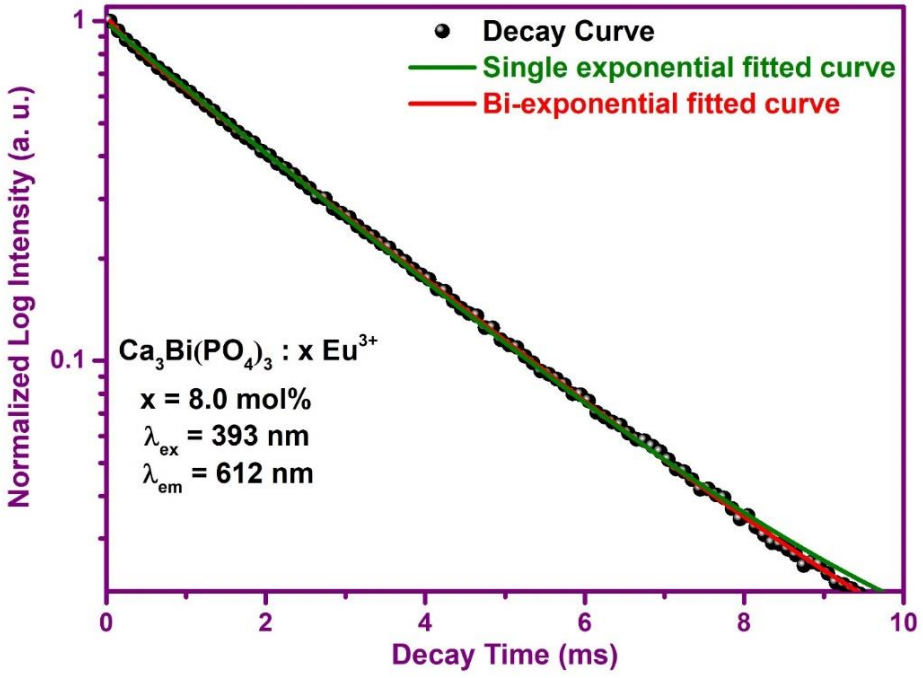

Fig. 3.10: *PL decay curve for the 8.0 mol% Eu^{3+} doped $Ca_3Bi(PO_4)_3$ phosphor at λ_{ex} = 393 and λ_{em} = 612 nm.*

The recorded decay curve was exponential and the best fitted with double exponential equation as described in equation number 2.06 section, 2.3.7 of chapter 2 and represent in

Fig.3.10. The average decay time (τ_{avg}) has been calculated with the help of formula presented in equation number 2.07 in section 2.3.7 of chapter 2 [154]. The average decay time for the $^5D_0$ level of the Eu^{3+} (x= 8.0 mol%) doped $Ca_3Bi(PO_4)_3$ phosphor is 1.598 ms.

3.3.7. Temperature Dependent PL Properties

Phosphors are usually coated over the UV/blue LED chips, which result in the rise of temperature from 120 to 150 °C of the phosphor materials and hence decreases the performance of the lighting devices. Therefore, the thermal quenching of phosphor is a very important parameter for SSL applications. The thermal quenching behavior of Eu^{3+} (x= 8.0 mol%) doped $Ca_3Bi(PO_4)_3$ phosphor was analyzed using the PL spectra at different temperatures. Fig. 3.11 represents the temperature dependent PL spectra for Eu^{3+} (x= 8.0 mol%) doped $Ca_3Bi(PO_4)_3$ phosphor under 393 nm excitation wavelength. The spectra reveal that the decrease in emission intensity with temperature increases from room to 200 °C. The inset of Fig. 3.11 represents the plot between relative integrated emission intensity of ($^5D_0 \rightarrow {}^7F_1$) and ($^5D_0 \rightarrow {}^7F_2$) transition with rising temperature by considering the respective transition highest emission intensity at 28 °C taken as 100 %. As demonstrated in the inset of Fig. 3.11, the PL intensity of the as synthesized phosphor at 150 and 200 °C persisted about 83.94 and 75.45%, respectively in comparison with its preliminary value at RT.

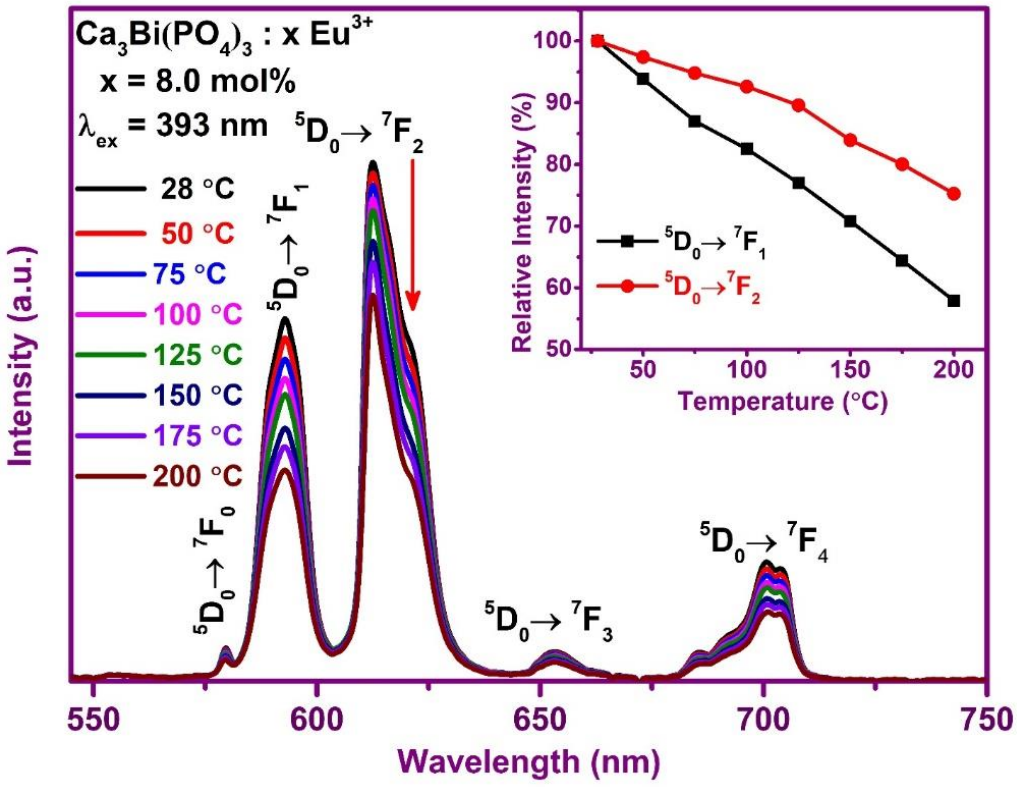

Fig. 3.11: *Temperature dependent PL properties of 8.0 mol% Eu^{3+} doped $Ca_3Bi(PO_4)_3$ phosphor. The inset shows the relative emission intensity variation with temperature in the range from 28 to 200 °C.*

A graph between $ln[(I_o/I_T) - 1]$ as a function of $1/K_B\,T$ was plotted for the estimation of ΔE. The graph with the linear fitting was displayed in Fig. 3.12, which gives the slope value as -0.218. Therefore, the activation energy ΔE can be approximately 0.218 eV for $Ca_3Bi(PO_4)_3$: x Eu^{3+} (x = 8.0 mol%) phosphor, which is higher than that of a red emitting phosphors $Li_2Ca_4Si_4O_{13}$:Eu^{3+} (~0.14 eV), $Sr_2Si_5N_8$:Eu^{2+} (~0.20 eV), $Ca_{19}Mg_2(PO_4)_{14}$:Eu^{3+} (~0.14 eV) [39,161,162]. Hence, the temperature dependent PL characteristics of the Eu^{3+} doped $Ca_3Bi(PO_4)_3$ phosphor suggests that the prepared phosphor exhibit good thermal stability.

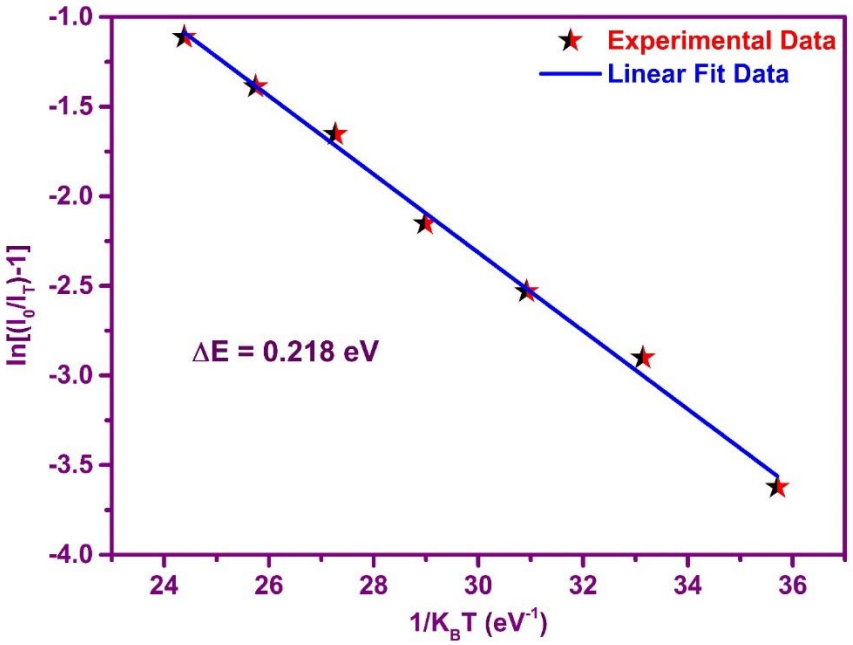

Fig. 3.12: *Plot between In[(I$_0$/I$_T$)-1] versus 1/K$_B$T plot.*

3.4. Conclusions

In summary, thermally stable red emitting Eu^{3+} activated $Ca_3Bi(PO_4)_3$ phosphors have been successfully synthesized via SSR method. The XRD patterns display that all the peaks can be recognized to be a cubic $Ca_3Bi(PO_4)_3$ crystal structure and also confirms that Eu^{3+} ion occupies at the Bi^{3+} ion site in $Ca_3Bi(PO_4)_3$ lattice without any changes in the cubic structure. The optical bandgap (E_g) is 4.40 eV for the host $Ca_3Bi(PO_4)_3$. The Bi^{3+} ions in the host lattice exhibit a broad broad blue host emission at 434 nm under 326 nm excitation wavelength. The PL excitation profile specifies that Eu^{3+} activated $Ca_3Bi(PO_4)_3$ phosphor can be efficiently excited by n-UV (393 nm) and blue (465 nm) radiation. PL spectra of Eu^{3+} activated $Ca_3Bi(PO_4)_3$ phosphor exhibit orange and intense red emission peaks at 593 nm ($^5D_0 \rightarrow {}^7F_1$) and 612 nm ($^5D_0 \rightarrow {}^7F_2$), respectively under the 393 and 465 nm excitation wavelengths. The optimized activator Eu^{3+}concentration was found to be 8.0 mol% for $Ca_3Bi(PO_4)_3$. The host emission intensity reduces and the activator peaks intensity enhanced with an increase in doping

concentration of Eu^{3+} ions in $Ca_3Bi(PO_4)_3$ phosphor, which indicates the energy transfer from host to activator (Eu^{3+}) ions under λ_{ex}= 326 nm. The CIE coordinates of undoped $Ca_3Bi(PO_4)_3$ were lie in the blue region and tuned towards the red region with an increase in doping concentration of Eu^{3+} ions via energy transfer. The CIE coordinates for the optimized phosphor under 393 nm excitation were falling in the red region and having color purity of 99.03%. The PL decay curves were bi-exponential for the optimized phosphor with an average decay time of 1.598 ms. The temperature impact over the PL properties indicates that the intensity persists to 75.45% at 200 °C that of at RT, which confirm the excellent thermal stability of phosphor. The combination of the above mentioned results endorses that the color tunable and red emitting Eu^{3+} activated $Ca_3Bi(PO_4)_3$ phosphor can act as a potential candidate for the applications in pc-white LEDs and other luminescent devices under the excitation of n-UV/blue radiation.

CHAPTER 4

White Light Emitting Thermally Stable $Ca_3Bi(PO_4)_3:Dy^{3+}$ Phosphor for Solid State Lighting Applications

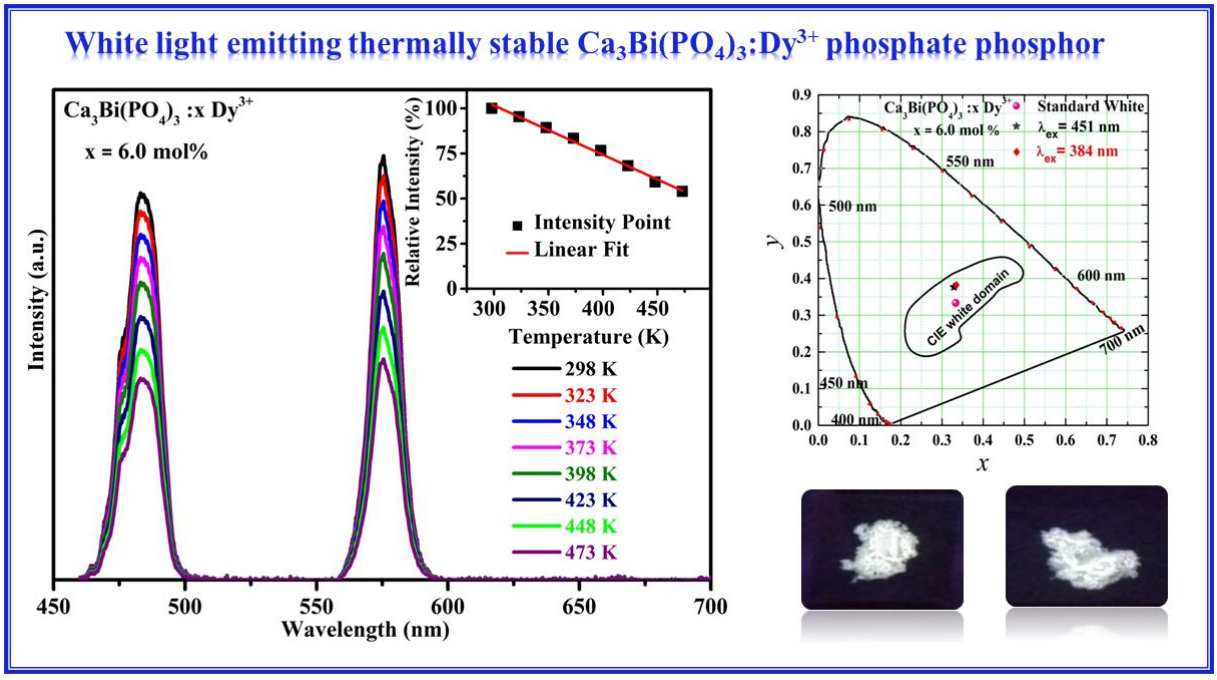

Part of this work has been published in Journal of the American Ceramic Society 102 (2019) 6087-6099 (IF: 4.186)

4.1. Introduction

In the present era, pc-WLEDs are materializing as a dynamic solid state light source for the next generation lighting and display devices. The pc-WLEDs offer numerous advantages such as higher efficiency, less energy consumption, long operating lifetime (>100,000 h), robustness and environmental friendly characteristics as compared to incandescent and fluorescent lamps [49,97,135,163,164]. There are several ways to obtain white light. Presently, the commercial approach comprises of blue emitting InGaN chip with yellow emitting (YAG: Ce^{3+}) phosphor [19,28]. However, this approach has disadvantages such as halo effect, low CRI index (Ra ≤65) and high CCT due to the lack of red color [7-9]. Another approach has been widely investigated, which is based on the UV/n-UV chip with the combination of red, green and blue (RGB) phosphors [3,165]. This approach provides better CRI and CCT but increases the synthesis processing time and cost of the device. Further, this approach also suffers from certain drawbacks such as phase separation, reabsorption of blue light by green and red phosphors, poor RGB color mixing and low color stability owing to the different emitting centers or phosphors [166,167]. To overcome the aforementioned problems, development of a single phase white light emitting phosphor is very important and has gained significant attention in comparison to RGB phosphors in the area of solid state lighting [20,168].

The white light emission can be obtained in single host lattice either by doping of single rare-earth (RE) or multiple RE ions in the appropriate host [28]. Among various RE activators, Dy^{3+} is considered as a potential activator ion in many host lattices for the white light emitting device applications [169]. Dy^{3+} ion doped materials exhibit emission peaks in blue and yellow region and their combination may yield white light. So, it is important to find chemically and thermally stable suitable host lattice for appropriate doping of Dy^{3+} ion in order to explore its suitability for WLED applications [23].

Among all inorganic phosphor hosts, phosphate based phosphors are the most preferred choice for display and lighting applications due to their low sintering temperature, high luminous efficiency, exceptional chemical and thermal stability [25,26,87]. Moreover, RE doped orthophosphate phosphors have attracted much attention for light emitting diodes and display applications [88,89]. The eulytite type orthophosphate with the general formula $A_3B(PO_4)_3$ (A = divalent alkaline earth & B = trivalent Bi or RE ion) have gained attention due to their excellent optical, magnetic, and dielectric property, along with thermal and chemical stability [90,91]. Among all the eulytite structures, calcium based eulytite type orthophosphate ($Ca_3Bi(PO_4)_3$) phosphor can be synthesized at a moderate temperature [92]. Eulytite-type materials doped with rare earth ion exhibit promising luminescence properties, due to the disordered structure [93]. Based on the literature survey, it was recognized that eulytite-type materials can perform as significant host matrices for lightning applications [91]. Recently, rare earth activated eulytite-type orthophosphate phosphors have been reported, such as $Sr_3Y(PO_4)_3:Dy^{3+}$, $Sr_3La(PO_4)_3:Eu^{2+}$, $Ba_3Lu(PO_4)_3:Eu^{2+}$, Mn^{2+}, $Ba_3Y(PO_4)_3:Dy^{3+}$etc. [94–97]. Yu et al. reported a comparative study of luminescent properties of $Ca_3Bi(PO_4)_3:Eu^{3+}$ phosphor synthesized via three different routes [98].

Nowadays, many wet chemical methods have been used to synthesize phosphors such as hydrothermal, sol-gel, combustion, co-precipitation method, etc. [170,171]. Among these wet chemical methods, co-precipitation method has been preferred due to its advantages such as easy process, homogeneous mixing of reactant, high yield, inexpensive, less-reaction time and the reaction takes place at normal atmospheric conditions [98,112,113]. Hence, the co-precipitation method has been used to synthesize the present phosphor.

In the current chapter, Dy^{3+} ions doped $Ca_3Bi(PO_4)_3$ phosphors have been successfully synthesized by co-precipitation method. The structural, morphological, photoluminescence and

colorimetric properties were discussed in detail to disclose that the $Ca_3Bi(PO_4)_3$ host is a promising white light emitting phosphor for solid state lighting applications.

4.2. Experimental Section

4.2.1. Sample preparation

A schematic procedure for the preparation of the Dy^{3+} doped $Ca_3Bi(PO_4)_3$ phosphor via co-precipitation method, which is given in Fig. 2.03 and explained in detail in section 2.2.2 of chapter 2. The highly pure $Ca(NO_3)_2•4H_2O$, $Bi(NO_3)_3•5H_2O$, $Dy(NO_3)_3•6H_2O$ and H_3PO_4 were used as precursor materials for the preparation of the Dy^{3+} doped $Ca_3Bi(PO_4)_3$ phosphor.

4.3. Results and discussion

4.3.1. X-ray Diffraction and Structural Analysis

Crystal structure and phase purity of un-doped and doped $Ca_3Bi(PO_4)_3$ powder samples were identified by XRD patterns. Fig. 4.01 (a) shows the standard JCPDS (Joint Committee on Powder Diffraction Standards) XRD pattern, while Fig. 4.01 (b, c & d) represent the XRD patterns of un-doped and doped $Ca_3Bi(PO_4)_3$: x Dy^{3+} (x = 1.0 and 10.0 mol%) powder samples, respectively. All the diffraction peaks of the un-doped and doped $Ca_3Bi(PO_4)_3$ powder samples were matched well with the standard JCPDS (85-2447) data. The synthesized powder sample exhibits cubic structure with space group of $I\bar{4}3d$ (220) and lattice parameters a = b = c = 9.984 Å. In this structure, Ca and Bi atoms are at the 16c site with occupation ratios equal to 3/4 and 1/4, respectively. The P and O atoms are located at 12a and 48e sites, respectively which form three dimensional $[PO_4]^{3-}$ tetrahedra structure [172]. The diffraction patterns for Dy^{3+} ions doped $Ca_3Bi(PO_4)_3$ powder did not reveal any impurity peaks, suggesting that the Dy^{3+} ions have been effectively incorporated into the host lattice.

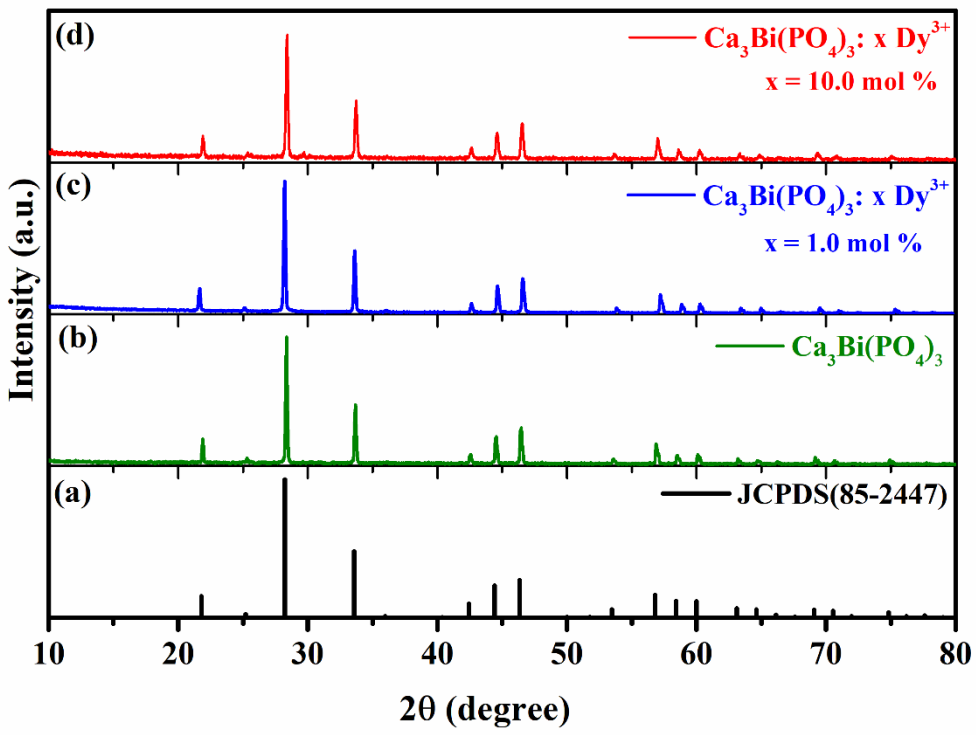

Fig. 4.01: *(a) Standard JCPDS (85-2447) data of $Ca_3Bi(PO_4)_3$, XRD pattern of (b) Un-doped $Ca_3Bi(PO_4)_3$ (c) 1.0 mol% Dy^{3+} doped $Ca_3Bi(PO_4)_3$ and (d) 10.0 mol% Dy^{3+} doped $Ca_3Bi(PO_4)_3$ sample synthesized by co-precipitation technique.*

The effective ionic radii of Dy^{3+} ion (r = 0.91 Å for coordination number CN = 6) is slightly smaller than of Bi^{3+} (r = 1.03 Å for CN = 6) ions. As the valence state of Dy^{3+} and Bi^{3+} ions are same, it is reasonable to assume that Dy^{3+} occupy the Bi^{3+} site [91]. The lattice parameter *(a)* was estimated for the un-doped and doped $Ca_3Bi(PO_4)_3$: x Dy^{3+} (x = 1.0 and 10.0 mol%) samples by using the following equation [114,173]:

$$\frac{1}{d^2} = \frac{h^2+k^2+l^2}{a^2} \qquad (4.01)$$

where *d* is the interplanar lattice spacing, *(h k l)* are the miller indices, and *a* is the lattice constant. The estimated lattice constant with uncertainties have been listed in Table 4.1.

Table 4.1: Lattice constant, crystallite size of $Ca_3Bi(PO_4)_3$ powder sample and microstrain present in the sample.

Sample $Ca_3Bi(PO_4)_3$: *x* Dy^{3+}	Lattice constant a (Å)	Crystallite size D (nm)		Microstrain
		Hall–Williamsons equation	Debye Scherrer formula	ε Strain ($x10^{-3}$)
x = 0.0 mol%	9.92 ± 0.06	58.82 ± 0.82	64.33 ± 0.90	0.088 ± 0.002
x = 1.0 mol%	9.92 ± 0.08	51.28 ± 0.71	56.53 ± 0.79	0.150 ± 0.003
x = 10.0 mol%	9.91 ± 0.08	50.03 ±0.75	54.15 ± 0.84	0.167 ± 0.003

The estimated lattice constant decreases in the case of Dy^{3+} ion doping in $Ca_3Bi(PO_4)_3$ host lattice as compared with the un-doped sample. The decrease in lattice constant can be attributed to compression in unit cell volume due to the substitution of smaller ionic radii of Dy^{3+} ions at the place of larger Bi^{3+} ions in the host lattice [174]. In the XRD patterns, FWHM and Braggs diffraction angle can be used to estimate the crystallite size of the powder sample. The crystallite size was determined by using the Debye-Scherer formula as depicted in equation number (2.02) in section 2.3.1 of chapter 2 [115,175]. β is the FWHM and θ is the Braggs diffraction angle. Since, the FWHM is mainly influenced by small crystallite size as well as microstrain present in sample, the Williamson-Hall (W-H) equation number (2.03) has been employed to estimate the strain and the crystallite size as given in the 2.3.1 of chapter 2 [176].

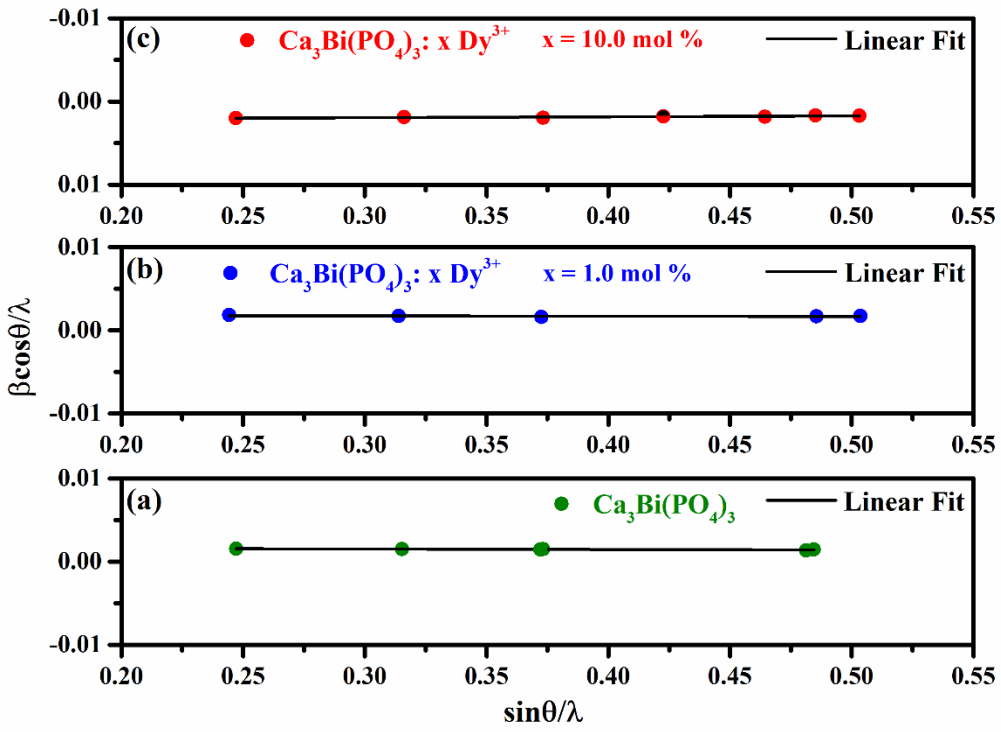

Fig. 4.02: *Williamson-Hall (W-H) plot of (a) un-doped $Ca_3Bi(PO_4)_3$ and (b) 1.0 mol% (c) 10.0 mol% Dy^{3+} doped $Ca_3Bi(PO_4)_3$ sample.*

The average crystallite size and lattice strain were estimated by using the plot of βCosθ/λ versus Sinθ/λ shown in the Fig. 4.02 (a & b) for un-doped and doped $Ca_3Bi(PO_4)_3$: x Dy^{3+} (x = 1.0 and 10.0 mol%). In this graph, slope represents the microstrain present in the prepared powder sample and reciprocal of y-axis intercept estimates the average crystallite size *(D)* of the sample. Average crystallite size estimated by using Debye-Scherer and Williamson Hall equations as well as strain present in the powder sample are summarized in Table 4.1. It is observed that the *D* value decreases by doping of Dy^{3+} ion. This tendency can be due to the ionic radius mismatch between Dy^{3+} and Bi^{3+} ions, which also suggests the incorporation of Dy^{3+} into $Ca_3Bi(PO_4)_3$ [177,178].

Rietveld refinement was performed by using FullProf suit software to verify the structure of the synthesized $Ca_3Bi(PO_4)_3$ phosphor. The refinement pattern for $Ca_3Bi(PO_4)_3$ sample was shown in Fig. 4.03, which confirms the single phase formation without any secondary phase and good agreement between the experimental and calculated XRD patterns.

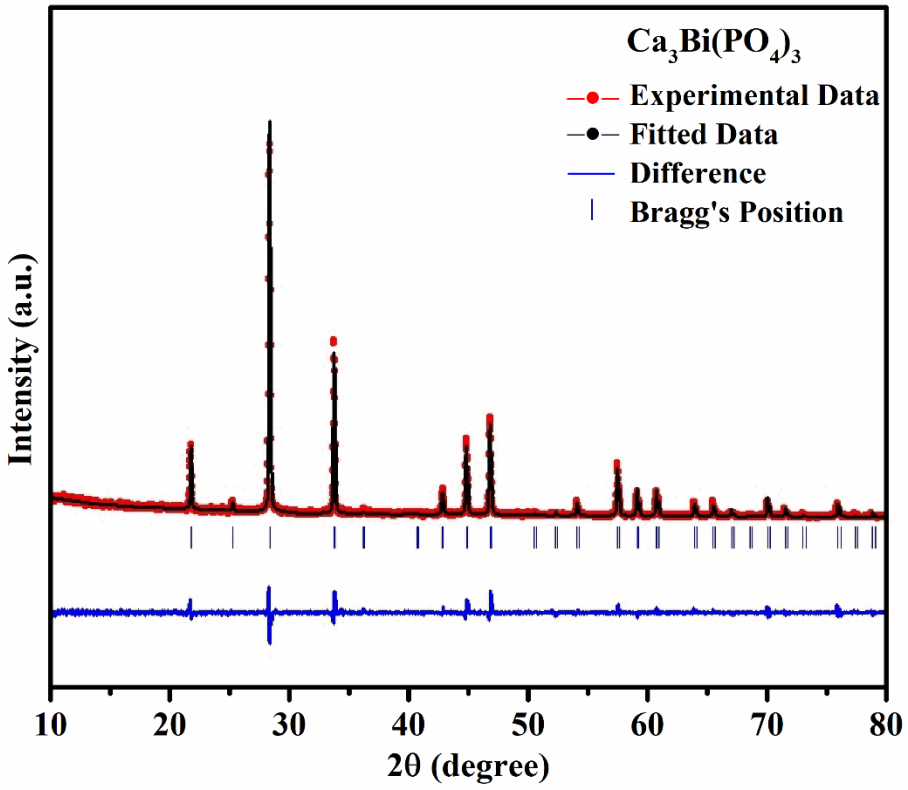

Fig. 4.03: *Reitveld refinement plot of un-doped $Ca_3Bi(PO_4)_3$ sample. The red and black colored lines represent the experimental and fitted data, respectively. The blue line represents the difference between the experimental and fitted data.*

The results also confirmed that the cubic structure of $Ca_3Bi(PO_4)_3$ has been synthesized having lattice parameters a = b = c = 9.895 Å. The quality of the Rietveld refinement has been checked by the goodness of fit, which must approach unity. In the present study, the goodness of fit has been found to be 1.64.

4.3.2. FT-IR spectroscopy

Fig. 4.04 represents the FT-IR spectrum of the $Ca_3Bi(PO_4)_3$ sample in 400-4000 cm^{-1} range. The absorption band of $(PO_4)^{3-}$ generally has two broad bands located in the range 500-650 cm^{-1} and 930-1250 cm^{-1}. The bands located at 561 and 1067 cm^{-1} are attributed to the symmetric stretching vibration of the PO_4^{3-} units. The $(PO_4)^{3-}$ free ions have four different modes i.e. v_1 (A1) of P-O symmetric stretching vibration, v_2 (E) of PO_2 symmetric bending vibration, v_3 (F2) of P-O asymmetric stretching vibration and v_4(F2) of PO_2 asymmetric bending vibration modes in the $(PO_4)^{3-}$ tetrahedron [179,180].

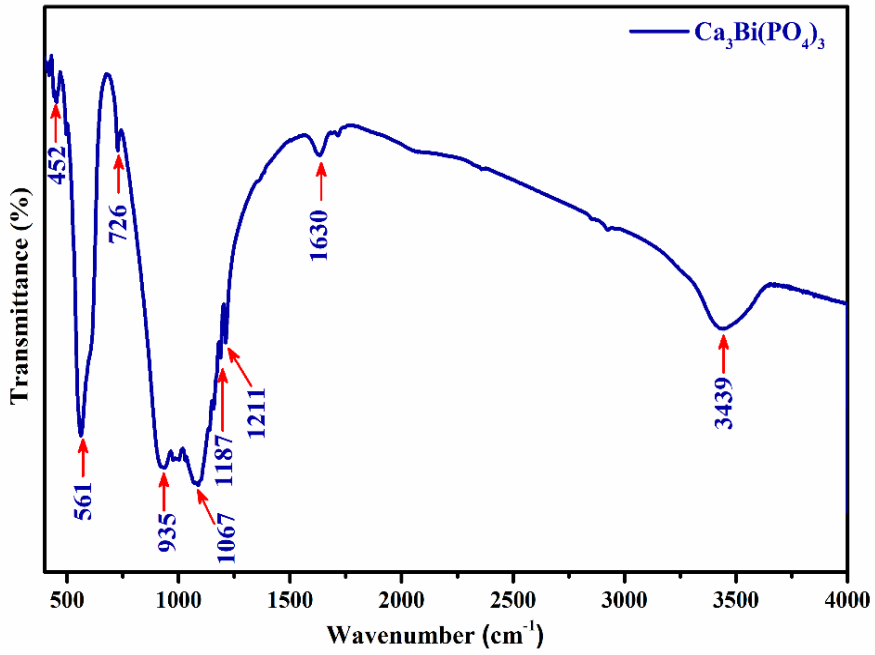

Fig. 4.04: *FT-IR Spectrum for un-doped $Ca_3Bi(PO_4)_3$ sample at room temperature.*

In the crystal structure, the $(PO_4)^{3-}$ vibration may undergo some changes due to the disordering of local point symmetry and anion O^{2-} ions. The band at 935 cm^{-1} correspond to the v_1 $(PO_4)^{3-}$ symmetric stretching [24]. The band at 452 cm^{-1} correspond to v_2 $(PO_4)^{3-}$ bending vibrations. The shoulder at 1211 cm^{-1} corresponds to the v_3 $(PO_4)^{3-}$ anti-symmetric stretching

vibrations whereas the band present at 726 cm^{-1} is assigned to $\nu_4 (PO_4)^{3-}$ bending vibration [181,182]. The band at 1630 cm^{-1} is ascribed to the bending vibrations of O-H bonds and 3439 cm^{-1} are attributed to the symmetric stretching of the water molecule [18].

4.3.3. Morphological Study

The surface morphology of $Ca_3Bi(PO_4)_3$: x Dy^{3+}(x= 1.0 mol%) phosphor is shown in Fig.4.05. The FE-SEM micrograph reveals that the as synthesized powder particles exhibit inhomogeneous and irregular shape. The typical particle size is in the micrometer range. The micrometer crystalline particles would be suitable to acquire efficient luminescence and very much useful for optoelectronic devices applications.

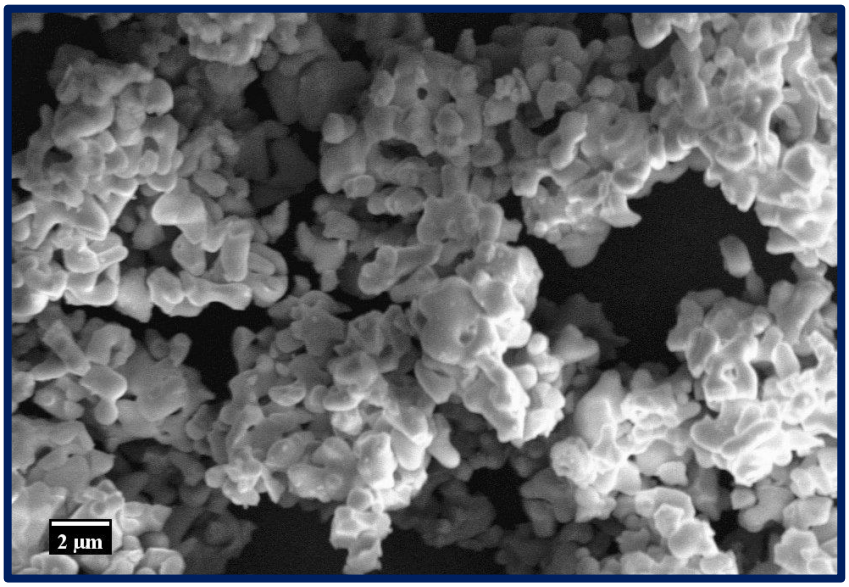

Fig. 4.05: *FE-SEM micrographs of $Ca_3Bi(PO_4)_3$: x Dy^{3+}(x= 1.0 mol%) phosphor.*

4.3.4. Luminescence Properties of Dy^{3+} Doped $Ca_3Bi(PO_4)_3$ Phosphor

The photoluminescence excitation (PLE) spectrum of 1.0 mol% Dy^{3+} doped $Ca_3Bi(PO_4)_3$ (CBP) phosphor is presented in Fig. 4.06 (a). PLE spectrum was recorded in the wavelength range from 300-500 nm while keeping the emission fixed at 575 nm. The PLE spectrum consists

of several absorption peaks at 322, 334, 347, 362, 384, 424, 451 and 471 nm, due to the characteristic transitions of the Dy^{3+} ions from the ground state $^6H_{15/2}$ to the various excited states as depicted in Fig. 4.06 (a). Among these, intense peaks were observed at 347, 362, 384 and 451 nm corresponding to the $^6H_{15/2} \rightarrow {}^6P_{7/2}$, $^6H_{15/2} \rightarrow {}^4I_{11/2}$, $^6H_{15/2} \rightarrow {}^6P_{5/2}$, $^6H_{15/2} \rightarrow {}^4I_{13/2}$, $^6H_{15/2} \rightarrow {}^6F_{7/2}$ and $^6H_{15/2} \rightarrow {}^4I_{15/2}$ transitions, respectively [183]. The PLE spectrum of the Dy^{3+} doped CBP phosphor shows that the synthesized phosphor can be excited efficiently by n-UV and blue light, which matches well with the emission of commercially available n-UV and blue LED chips.

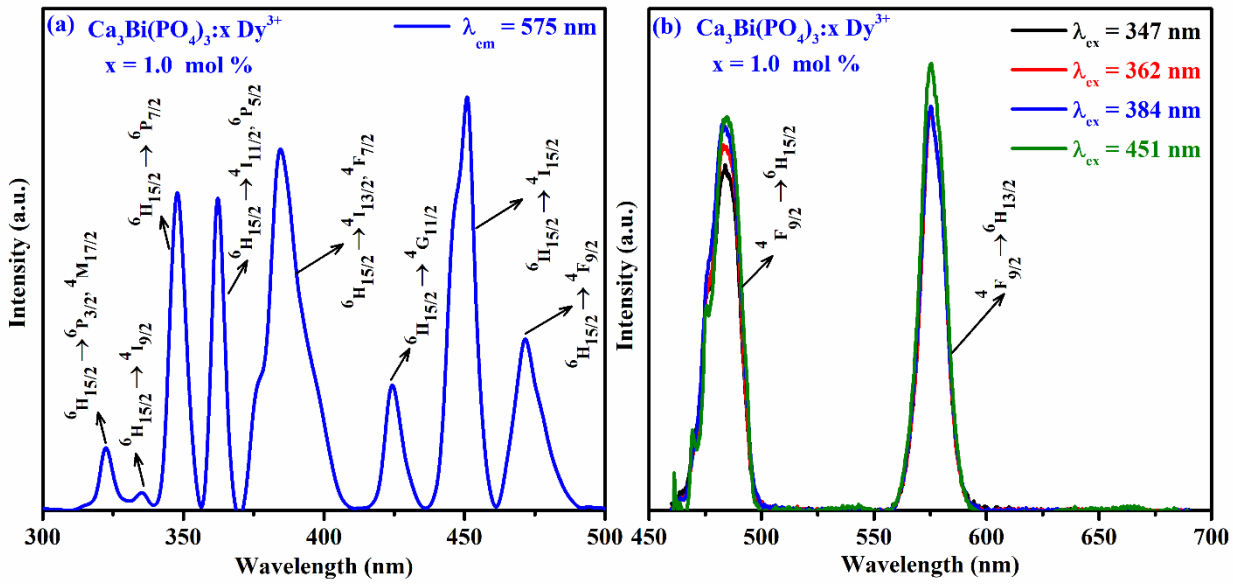

Fig. 4.06: *(a) PLE spectrum of 1 mol% Dy^{3+} doped $Ca_3Bi(PO_4)_3$ phosphors by monitoring emission at 575 nm and (b) emission spectra of 1 mol% Dy^{3+} doped $Ca_3Bi(PO_4)_3$ phosphors recorded under different excitation wavelengths.*

The emission spectra of 1.0 mol% Dy^{3+}doped $Ca_3Bi(PO_4)_3$ phosphor shown in Fig. 4.06 (b). The emission spectra have been recorded in the range of 450 to 700 nm by exciting at 347, 362, 384 and 451 nm wavelengths. A minute variation in the emission intensity profile has been

observed under different excitation wavelengths. The emission spectra consist of two main peaks centered at 484 nm (blue band) and 575 nm (yellow band) corresponding to transitions $^4F_{9/2} \rightarrow {}^6H_{15/2}$ and $^4F_{9/2} \rightarrow {}^6H_{13/2}$ of Dy^{3+} ions, respectively. The emission bands $^4F_{9/2} \rightarrow {}^6H_{15/2}$ and $^4F_{9/2} \rightarrow {}^6H_{13/2}$ corresponding to the magnetic dipole (MD) and forced electric dipole (ED) transitions of Dy^{3+} ions, respectively [184]. The emission intensity of MD transition does not depend on the crystal field of the host but forced ED transition strongly depends on the crystal field environment around Dy^{3+} ions. The intensity of yellow band is higher than the blue band, which may be due to the location of the active ions (Dy^{3+}) in low symmetry site environment without the inversion center in the host [22,185].

4.3.5. Effect of Dy^{3+} Concentration

To investigate the effect of activator ion concentration on emission properties of $Ca_3Bi(PO_4)_3$ host lattice, Dy^{3+} concentration was varied from x = 1.0 to 10.0 mol%. Fig. 4.07 (a-d) represents the emission intensity variation as a function of Dy^{3+} ion doping concentration in $Ca_3Bi(PO_4)_3$ phosphor under excitation of 347, 362, 384 and 451 nm wavelengths. It can be observed from Fig. 4.07 (a-d) and its inset, that the emission intensity increases with increasing Dy^{3+} concentration up to 6.0 mol%. Beyond 6.0 mol% of Dy^{3+} ions concentration in $Ca_3Bi(PO_4)_3$ phosphor, the emission intensity decreased due to the concentration quenching which may be due to increase in the probability of non-radiative energy transfer as the distance between adjacent Dy^{3+} ions are condensed. In general, the energy transfer between Dy^{3+} ions depends on the critical distance between them. This critical distance can be calculated for the present host by the expression given by Blasse, which is defined in equation number (1.01), section 1.3.3 of chapter 1 [63]. In this case, R_c is calculated by using of following values C_o = 0.06 mol of Dy^{3+}, V = 954.22 $Å^3$ and N = 4. With increase in Dy^{3+} ion concentration above the 6.0 mol%, the distance between Dy^{3+}-Dy^{3+} ions are below the critical distance. The R_c value

has been found to be 19.64 Å for $Ca_3Bi(PO_4)_3$:x Dy^{3+} (x = 6.0 mol%). Since, the calculated R_c value is larger than 5 Å, multipolar interaction will become significant in the present case [65].

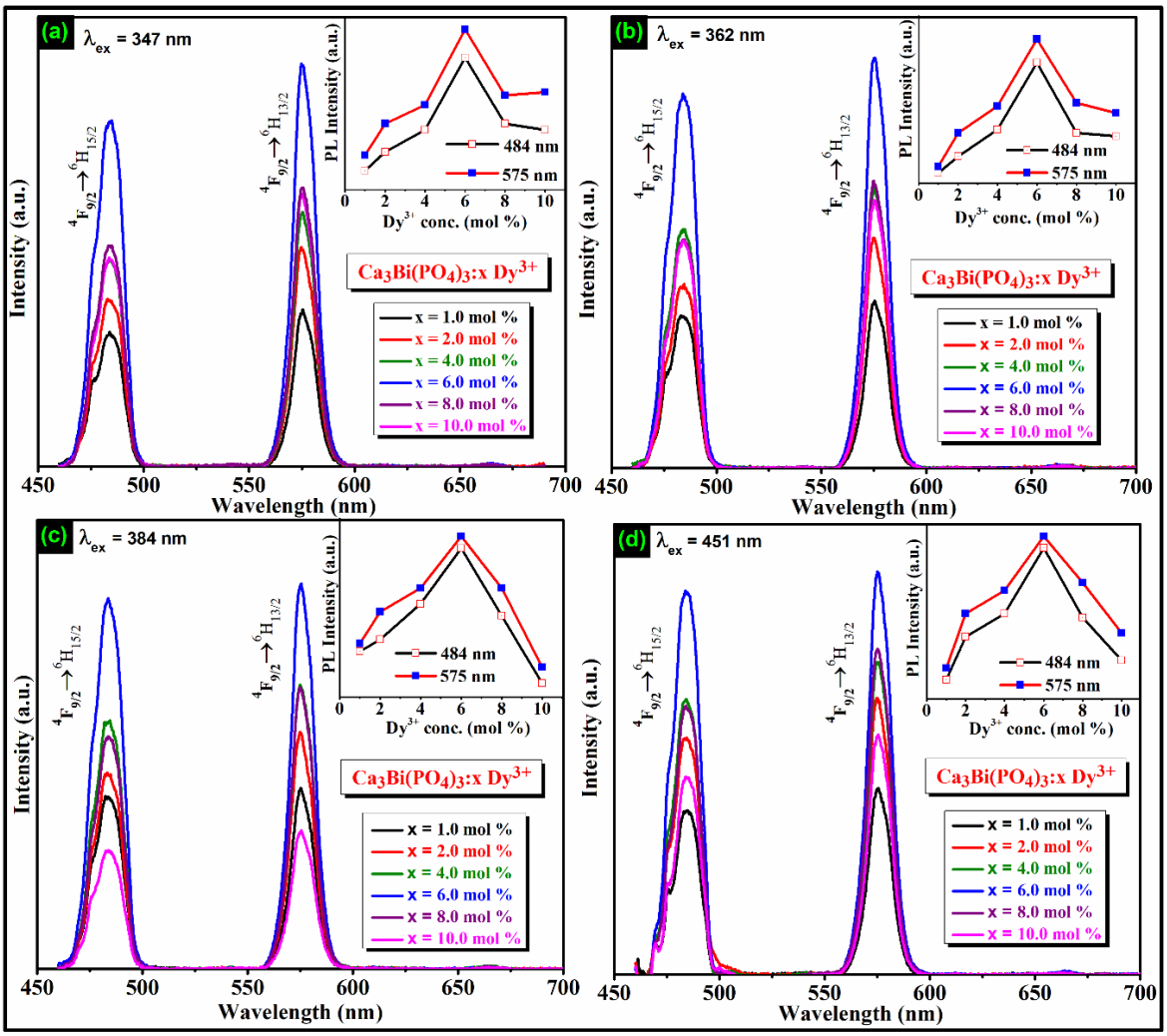

Fig. 4.07: *PL emission spectra of varying Dy^{3+} ion concentration (x = 1.0, 2.0, 4.0, 6.0, 8.0 and 10.0 mol%) in $Ca_3Bi(PO_4)_3$ phosphors under different excitations λ_{ex} = (a) 347, (b) 362, (c) 384 and (d) 451 nm (Inset represents the variation in the emission intensity of the emission peaks with Dy^{3+} ion concentration).*

According to Dexter's theory, the luminescence intensity *I* and the mole fraction of doping ion concentration *x* could be related as follows [64, 66,67]

$$\frac{I}{x} = K[1 + \beta(x)^{Q/3}]^{-1} \quad (4.02)$$

where *K* and *β* are constants for the same excitation of a given host lattice. The value of *Q* explains the type of electric multipolar among the adjacent Dy^{3+} ions. The values of *Q* = 6, 8, and 10 define the interaction to be dipole-dipole, dipole-quadrupole, quadrupole-quadrupole, respectively [68]. Assuming that $\beta(x)^{Q/3} >> 1$, the equation (4.02) can be approximately reduced as follows:

$$\log\frac{I}{x} = K' - \frac{Q\log(x)}{3}; \ (K' = \log k - \log\beta) \quad (4.03)$$

In the present work, the value of *Q* has been estimated using the slope of the graph between log(I/x) and log (x) as shown in Fig. 4.08. The calculated slope (-2.002) of the linear fit is equal to $-Q/3$ value which gives *Q* as 6.006 that is close to 6. The estimated value of *Q* confirmed that the energy transfer between the adjacent Dy^{3+} ions is due to the dipole-dipole interaction.

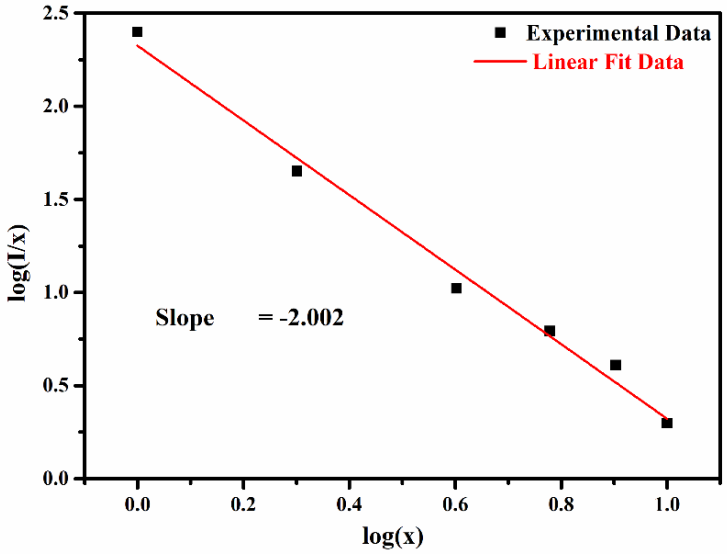

Fig. 4.08: *Relationship of log (I/x) with log(x) plot.*

Fig. 4.09 represents the partial energy level diagram of Dy^{3+} doped $Ca_3Bi(PO_4)_3$ phosphor. The as-synthesized phosphor absorbs n-UV and blue light, which are related to the absorption bands originated from $^6H_{15/2}$ to various excited energy levels of Dy^{3+} ions. It can be seen from the energy level diagram that the non-radiative transitions take place above $^4F_{9/2}$ level as the energy difference between different energy levels is low.

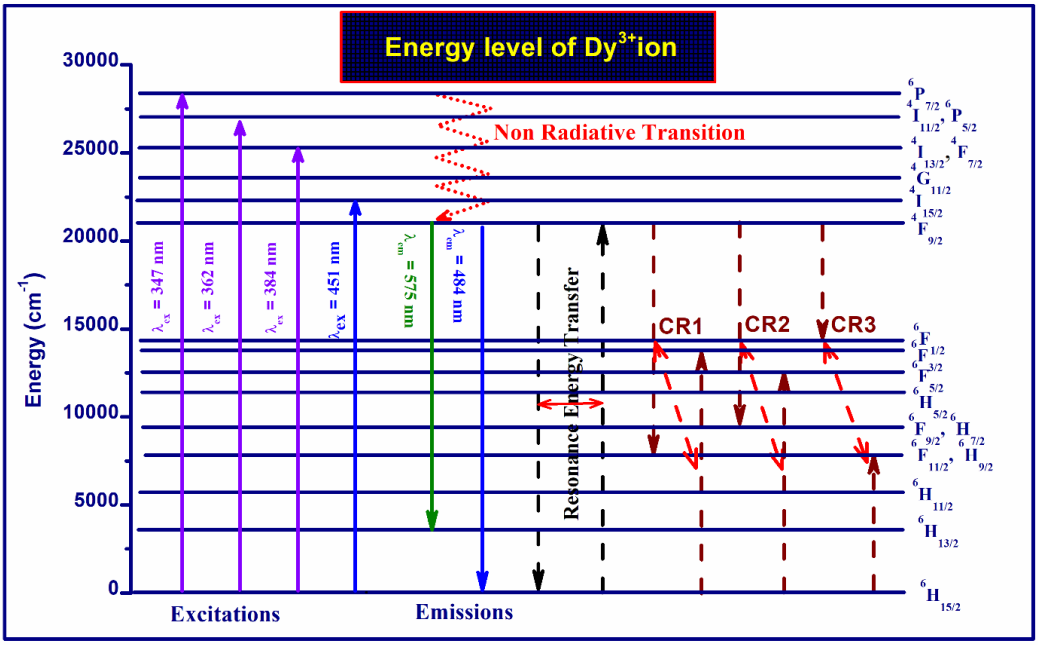

Fig. 4.09: *Partial energy level diagram of Dy^{3+} in $Ca_3Bi(PO_4)_3$ phosphor.*

On the other hand, radiative photonic emission takes place from $^4F_{9/2}$ state to the different levels $^6H_{13/2}$ and $^6H_{15/2}$ due to sufficient energy difference between them. The non-radiative energy transfer and concentration quenching may take place due to resonance energy transfer (RET) and cross relaxation (CR) channels among neighboring Dy^{3+} ions. Considering the energy match rule, the possible resonant energy transfer and three cross relaxation channels (CR1, CR2, CR3) are as follows [48,186,187] :

$$\text{RET: } (^4F_{9/2}+{}^6H_{15/2} \rightarrow {}^6H_{15/2}+{}^4F_{9/2})$$

CR1: $(^4F_{9/2}+^6H_{15/2}\rightarrow ^6F_{11/2},^6H_{9/2}+^6F_{3/2})$

CR2: $(^4F_{9/2}+^6H_{15/2}\rightarrow ^6F_{9/2},^6H_{7/2}+^6F_{5/2})$

CR3: $(^4F_{9/2}+^6H_{15/2}\rightarrow ^6F_{1/2},^6F_{11/2}+^6H_{9/2})$

4.3.6. Colorimetry Calculations

The CIE chromaticity coordinates were calculated based on the emission spectra measured for Dy^{3+} doped $Ca_3Bi(PO_4)_3$ phosphor under 384 and 451 nm excitation wavelengths. The values of the CIE chromaticity coordinates have been calculated under 451 nm excitation, which are listed in Table 4.2. All the calculated values of the CIE chromaticity coordinates are situated in CIE white region. Fig. 4.10 represents the CIE coordinate values (0.336, 0.385) and (0.329, 0.377) for 6.0 mol% Dy^{3+}doped $Ca_3Bi(PO_4)_3$ phosphors under 384 and 451 nm excitation, respectively. The calculated CIE coordinate values are very close to the standard white light point (0.333,0.333). Hence, it can be concluded that white light could be generated from Dy^{3+} doped $Ca_3Bi(PO_4)_3$ phosphor to make it as a suitable candidate for WLEDs.

Table 4.2: CIE chromaticity coordinates (x, y), CCT and Average decay time (μs) of $Ca_3Bi(PO_4)_3$:xDy^{3+} phosphors for 451 nm excitation.

Sample $Ca_3Bi(PO_4)_3$: *x* Dy^{3+}	Color Coordinates (x, y) with $\pm$ 0.3 × 10^{-3} uncertainty	CCT (K)	Average decay time (ms)
x = 1.0 mol%	(0.326, 0.375)	5743 ± 6.37	840 ± 0.012
x = 2.0 mol%	(0.336, 0.387)	5364 ± 5.95	778 ± 0.015
x = 4.0 mol%	(0.340, 0.385)	5241 ± 5.81	739 ± 0.019
x = 6.0 mol%	(0.329, 0.377)	5615 ± 6.23	699 ± 0.013
x = 8.0 mol%	(0.336, 0.385)	5360 ± 5.94	647 ± 0.017
x = 10.0 mol%	(0.344, 0.391)	5109 ± 5.67	590 ± 0.021

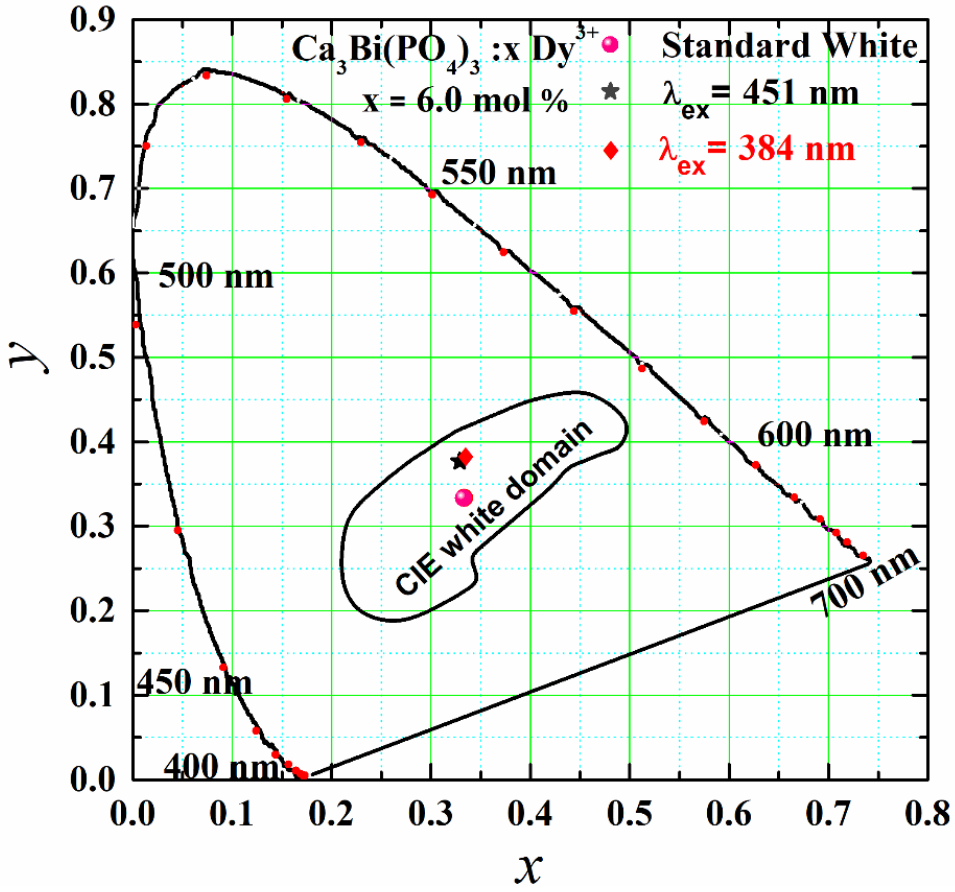

***Fig. 4.10**: CIE diagram of 6.0 mol% Dy^{3+} doped $Ca_3Bi(PO_4)_3$ phosphor λ_{ex} = 384 & 451 nm.*

The CCT has been defined as the quality of the light source, which reveals that the generated white light is either cool or warm. The value of CCT has been calculated by an equation proposed by McCamy as mentioned in equation number (1.09) section 1.4 of chapter 1 [70].The CCT values have been calculated for Dy^{3+} doped $Ca_3Bi(PO_4)_3$ phosphors under 451 nm excitations wavelength listed in Table 4.2. The values of CCT for all synthesized phosphors samples were found to be in the range 5109-5743 K, which falls in the cool white light region.

4.3.7. Lifetime Analysis

The decay curves have been recorded to estimate the lifetime for the $^4F_{9/2}$ level under 451 nm excitation by varying Dy^{3+} concentration in $Ca_3Bi(PO_4)_3$ phosphor at room temperature as represented in Fig. 4.11. The decay curves were fitted with different exponential equations.

It can be observed that all the decay curves were fit biexponentially with the following equation presented in equation number (2.06) in section 2.3.7 of chapter 2 [129,130]. The average value of the decay time for different Dy^{3+} doped $Ca_3Bi(PO_4)_3$ phosphor samples was evaluated from formula presented in equation number (2.07) in section 2.3.7 of chapter 2 [131]:

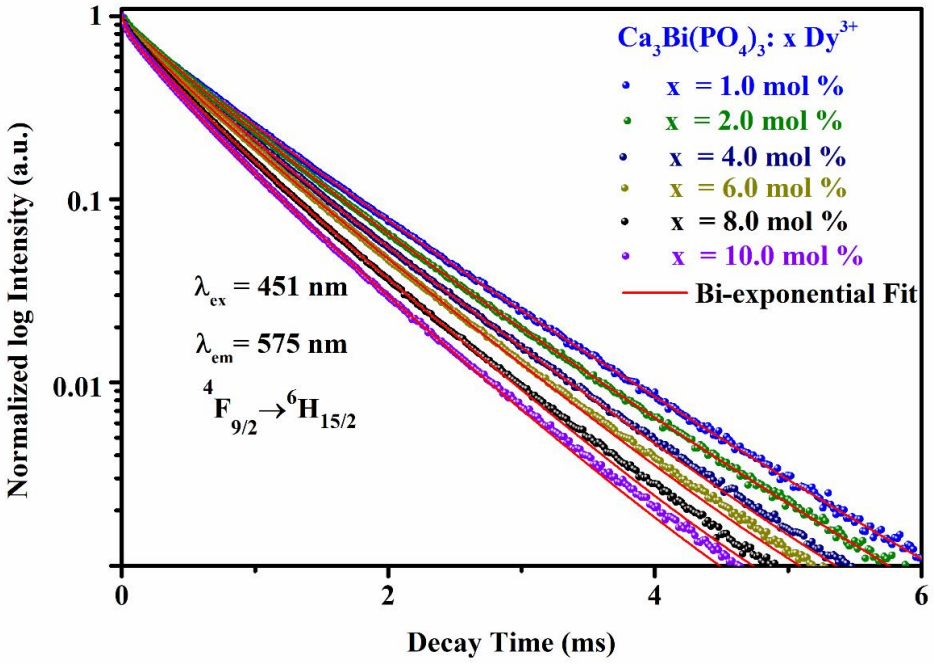

Fig. 4.11: *Decay curves for $^4F_{9/2}$ level in Dy^{3+} doped $Ca_3Bi(PO_4)_3$ phosphors.*

The average decay values of the different phosphors have been listed in Table 4.02. The average decay time of 1.0 mol% Dy^{3+} doped $Ca_3Bi(PO_4)_3$ phosphor is 840 μs. With increasing the concentration of Dy^{3+} ions, the average decay time of the phosphor decreases from 840 to 590 μs. The decrease in average lifetime is due to the energy transfer among Dy^{3+} ions.

4.3.8. Effect of Temperature on Photoluminescence Intensity

To better understand the thermal quenching behavior of CBP: x Dy^{3+} (x = 6.0 mol%) phosphor, the photoluminescence spectra measured under 384 nm excitation wavelength with

increasing temperature from 298 to 473 K as shown in Fig. 4.12. As the temperature increases from 298 to 473 K, the emission intensity of the phosphor decreases. The inset of Fig. 4.12 represents the plot between relative integrated emission intensity of $^4F_{9/2} \rightarrow {}^6H_{13/2}$ transition with temperature by considering the highest integrated emission intensity as 100 %. The emission intensity decreased to 83.41 % at 373 K and 54.08 % at 473 K and the shape of the emission band remains unchanged which indicate that the phosphor Dy^{3+} doped $Ca_3Bi(PO_4)_3$ exhibit excellent thermal stability [154].

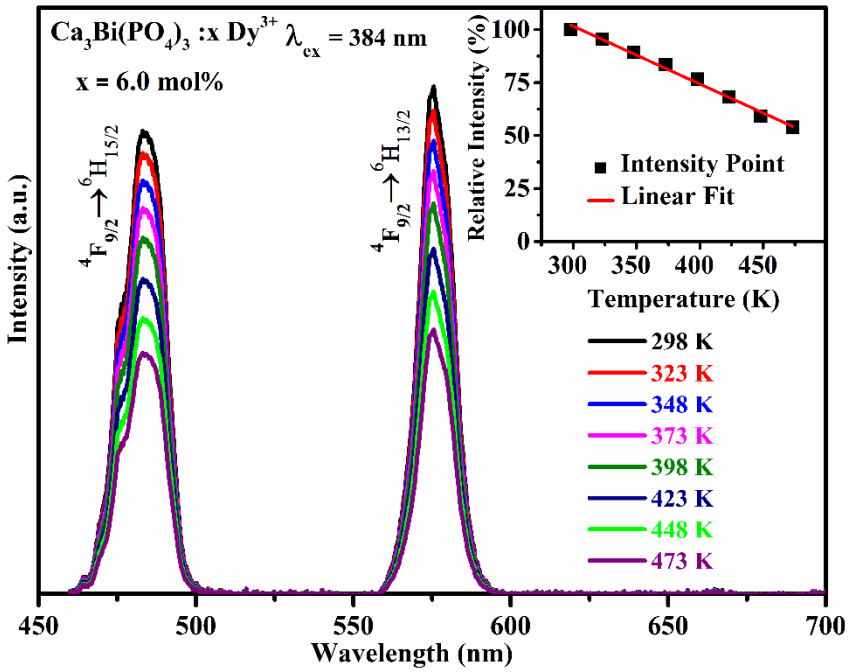

Fig. 4.12: *TD-PL spectra of Dy^{3+} doped $Ca_3Bi(PO_4)_3$ phosphors. The inset shows the relative emission intensity variation of $^4F_{9/2} \rightarrow {}^6H_{13/2}$ transition in the temperature range 298-473 K.*

Furthermore, the thermal stability of $Ca_3Bi(PO_4)_3$: x Dy^{3+} (x = 6.0 mol%) phosphor can be analyzed by evaluating activation energy (ΔE). Hence, the activation energy (ΔE) for the thermal quenching was calculated using the Arrhenius equation shown in equation number 2.08

in section 2.3.8 of chapter 2 [188]. The value of activation energy (ΔE) can be estimated form the linear fitted graph between $ln[(I_o/I_T)-1]$ and $1/K_BT$ as represent in Fig. 4.13. From the slope of the linear fit, the estimated activation energy for $Ca_3Bi(PO_4)_3$: x Dy^{3+} (x = 6.0 mol%) phosphor was found to be 0.223 eV, which is higher than that of $Ca_3WO_6:Dy^{3+}$ (0.105 eV), $CaAl_4O_7:Mn^{4+}$ (0.196 eV) and $Ca_{1.65}Sr_{0.35}SiO_4:Ce^{3+}$ (0.135) phosphor[121,133,134]. The temperature dependent photoluminescence result specifies that the as-prepared $Ca_3Bi(PO_4)_3$:x Dy^{3+} (x = 6.0 mol%) phosphor exhibits good thermal stability.

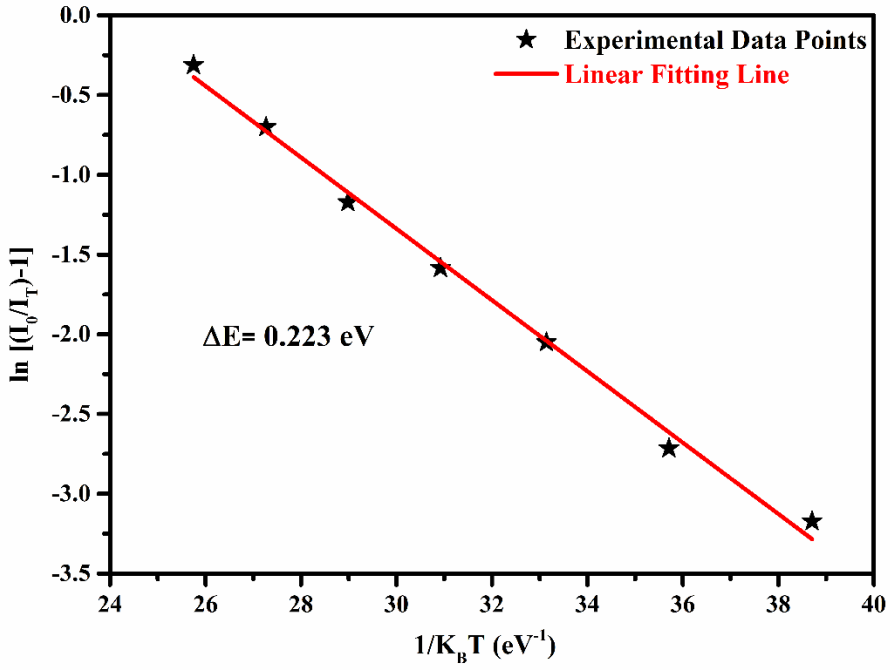

Fig. 4.13: *Plot of $ln[I_o/I_T)-1]$ with $1/K_BT$ for the 6.0 mol% Dy^{3+} doped $Ca_3Bi(PO_4)_3$ phosphor.*

4.4. Conclusions

Dy^{3+} doped $Ca_3Bi(PO_4)_3$ phosphors have been successfully synthesized with different doping concentrations (0-10.0 mol%) by co-precipitation method. Structural, morphological and spectroscopic properties of the synthesized phosphors were characterized by XRD, FE-SEM, FT-IR, PL, temperature dependent PL and lifetime. The XRD and Rietveld analysis

revealed that the synthesized phosphors consist of a single phase with cubic structure. FT-IR spectrum indicated the presence of different functional groups. The FE-SEM micrograph represents that the as-synthesized powder particles had micron size with an irregular shape. The excitation spectra indicate that this phosphor could be effectively excited by n-UV and blue LED chips. Emission spectra of Dy^{3+} doped $Ca_3Bi(PO_4)_3$ phosphor exhibit blue and yellow emission bands at 482 ($^4F_{9/2}\rightarrow{}^6H_{15/2}$) and 575 nm ($^4F_{9/2}\rightarrow{}^6H_{13/2}$), respectively. The optimized doping concentration was found to be 6.0 mol% and the concentration quenching mechanism arises due to the dipole-dipole interaction. The CIE coordinates located in the white light region and the CCT values indicate cool white light emission. The decay curves were bi-exponential in nature and the value of decay time decreased with increasing Dy^{3+} ions concentration suggesting the energy transfer between adjacent Dy^{3+} ions. The temperature dependent PL indicates good thermal stability of the as synthesized phosphor. The combination of the above mentioned results suggest the potential utility of the synthesized phosphors for the applications in WLEDs under the excitation of n-UV/blue LED chips.

CHAPTER 5

Structural and Color Tunable Properties in Sm^{3+}/Eu^{3+} Doped $Ca_3Bi(PO_4)_3$ Phosphor for Solar Cell and w-LED Applications

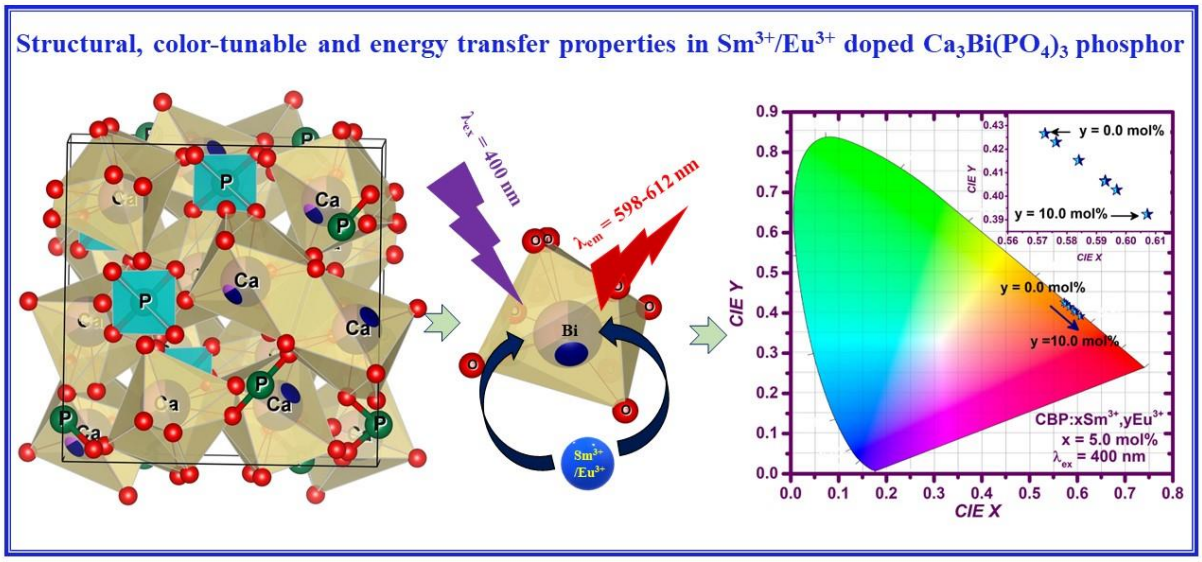

Part of this work has been published in Journal of Materials Science: Materials in Electronics, 33 (2022) 5201-5213 (IF: 2.8)

5.1.Introduction

The worldwide energy demand and consumption have been rising rapidly due to the overgrowing population and people picking a lavish lifestyle [2,72]. This energy demand and consumption can resolve by opting two significant approaches, i.e., energy-saving strategy and employing green renewable energy. As a point of interest, pc-w-LEDs and solar cells have been considered as the two potential approaches [29,30]. The solar spectrum is an abundant and valuable green renewable energy resource that is freely accessible in every part of the earth. It has the potential to fulfill the worldwide energy crises, which could possibly reduce the dependency on traditional fossil fuel-based power generation [189]. A solar cell has attracted much attention among researchers and industries as a favorable choice for green renewable energy generation without any harmful impact on the nature. Presently, silicon-based solar cells are leading the worldwide photovoltaic industries due to their easy availability in colossal quantity, zero toxicity and high stability [190]. But, the silicon-based solar cell operated with limited conversion efficiency cause most of the spectrum was unexploited, i.e., spectral mismatch. Especially, the intensity of radiation in the solar spectrum within the range from 300 to 500 nm was not utilized by C-Si solar cell due to high reflection, surface recombination and thermalization losses [191]. A number of scientists and researchers have been continuously working and devised numerous methods, which can enhance the solar cell energy conversion efficiency by utilizing the unused part of the solar spectrum [31–34]. One of the most important methods is the downshifting phosphor coating on top of the solar cell, which can enhance the conversion efficiency. To achieve this result, n-UV pumped efficient green, orange or red emitting phosphor material required, which can directly apply on the top of solar cell and enhance the spectral conversion efficiency.

Also, the red emitting phosphor used in commercially available pc-w-LEDs, which can conquer the shortcomings such as halo effect, deficient color rendering index (R_a< 65~70) and less thermal stability [35–38]. Thus, it is necessary to prepare effective visible red emitting phosphor having numerous eminent characteristics, for instance, highly efficient n-UV/blue excitation with intense emission, chemically stable and environmental friendly materials to use in solar cell and pc-w-LEDs [39–42].

In recent years, RE induced downshifting phosphor materials had been synthesized for the utility in pc-w-LEDs [192]. RE activated eulytite type orthophosphate $A_3B(PO_4)_3$ (A = divalent ions & B = trivalent Pb, Bi or RE ion) has been reported as appropriate phosphor host material due to their excellent optical properties, high chemical as well as thermal stability along with high luminous efficiency [90,193–195]. Amongst the eulytite type orthophosphate hosts, $Ca_3Bi(PO_4)_3$ is a remarkable host for luminescent materials and possibly utilized in numerous lighting and display, sensing devices [86,92].

The appropriate dopant of transition metal/ RE ions was essential in the phosphor host, which can effectively absorb UV/blue photons and emit in the red region [196,197]. Among all the RE ions, Europium (Eu^{3+}/Eu^{2+}) activated phosphors are perfectly appropriate for downshifting phosphor, due to their numerous energy levels as well as high luminescence efficiency and also emit in the red region upon excitation with the n-UV/blue wavelengths [198]. Adding a sensitizer to an activator will possibly expand the absorption profile and boost the emission intensity of the activator through the ET process. Among numerous RE ions, Sm^{3+} has been observed as the enormously suitable sensitizer for Eu^{3+} ions [199]. The inclusion of Sm^{3+} ions as the sensitizer, enhanced the Eu^{3+} emission in different host matrices.

In the present study, single Sm^{3+} doped and combination of Sm^{3+}, Eu^{3+} co-doped calcium bismuth phosphate [$Ca_3Bi(PO_4)_3$] phosphors have been prepared via co-precipitation technique. The crystallographic phase, structure, morphology, thermal behavior and optical properties have been examined. Energy transfer mechanism was studied in detail via employing Dexter's ET formula and Reisfeld's approximation. Furthermore, temperature-dependent PL spectra, CIE coordinates and lifetime curve analysis have been explored to enhance the quality of luminescence characteristics of CBP: xSm^{3+},yEu^{3+} phosphors for the utility in pc-w-LEDs, solar cell and other photonic devices.

5.2. Experimental section

CBP doped with Sm^{3+} ion and co-doped with Sm^{3+}, Eu^{3+} ions samples were prepared via co-precipitation technique which is given in Fig. 2.03 and explained in detail in section 2.2.2 of chapter 2. In CBP:xSm^{3+} samples, doping concentration (Sm^{3+} ions) was varied as x = 1.0 to 8.0 mol%. In the case of co-doped CBP:xSm^{3+}, yEu^{3+} samples, Sm^{3+} ion concertation was fixed (x = 5.0 mol%) and varied the Eu^{3+} ion concentration from y = 1.0 to 10.0 mol%. The highly pure $Ca(NO_3)_2$•$4H_2O$ (99.00%), Bi_2O_3 (99.00%), H_3PO_4 (99.00%), $Sm(NO_3)_3$•$6H_2O$ (99.99%) and $Eu(NO_3)_3$•$5H_2O$ (99.99%) were used as a precursor materials for the preparation of CBP:xSm^{3+} and CBP:xSm^{3+}, yEu^{3+} phosphors.

5.3. Results and Discussion

5.3.1. X-ray Diffraction Studies

The crystalline phase and structure of undoped, doped and co-doped CBP samples were investigated based on diffraction patterns as shown in Fig. 5.01. Several sharp and intense diffraction patterns indicate that the prepared samples have crystalline in nature. The diffraction

patterns for the prepared samples were analogous and well indexed with standard patterns (JCPDS: 085-2447). All the prepared samples were crystallized in cubic structure with $I\bar{4}3d$ (220) space group. The diffraction patterns for Sm^{3+} doped and Sm^{3+}/Eu^{3+} co-doped CBP samples did not disclose any anonymous peaks, intimating that the RE ions were efficiently assimilated into the CBP host lattice.

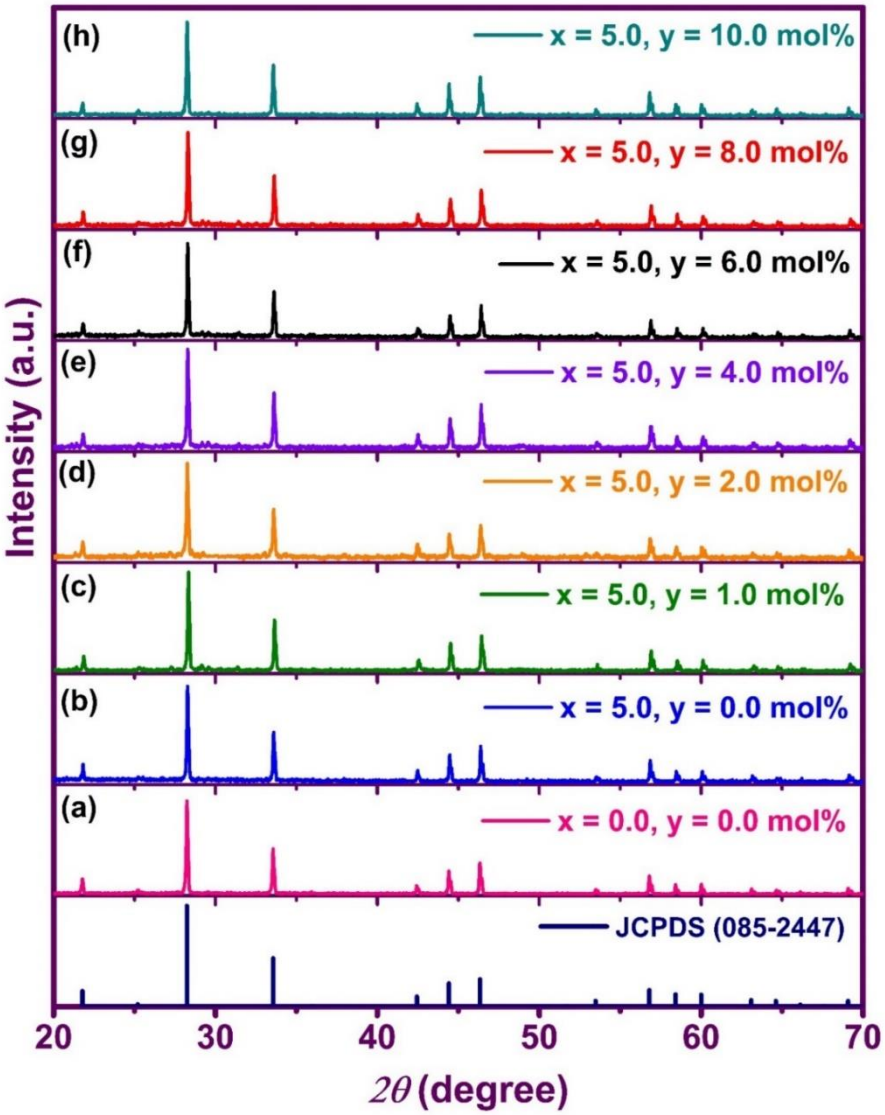

Fig. 5.01: *XRD patterns for (a) undoped CBP powder, (b) CBP:xSm^{3+} (x = 5.0 mol%) and (c-h) co-doped CBP:xSm^{3+}, yEu^{3+} (x = 5.0 & y = 1.0 to 10.0 mol%) samples compared with standard JCPDS data.*

The Debye Scherer formula [$D = K\lambda/\beta cos\theta$] has been used to estimate the average crystallite (D) size for the prepared samples [115]. Shape factor ($K \approx 0.91$), X-ray wavelength for CuK_α radiation, ($\lambda \approx 1.5406$ Å), full width at half maxima (β) of intense patterns at Braggs angles (θ) of 28.2°, 33.5°, 46.3° and 44.4° were used to estimate D value of samples. The average crystallite size for the prepared sample were tabulated in Table 5.01.

Table 5.1: Crystallite size of CBP:xSm^{3+}, yEu^{3+} powder sample assessed using Debye-Scherrer formula.

Sample CBP:xSm^{3+}, yEu^{3+}	Crystallite Size D (nm)
x = 0.0 & y = 0.0 mol%	72.95
x = 5.0 & y = 0.0 mol%	72.74
x = 5.0 & y = 1.0 mol%	71.47
x = 5.0 & y = 2.0 mol%	71.15
x = 5.0 & y = 4.0 mol%	71.02
x = 5.0 & y = 6.0 mol%	70.97
x = 5.0 & y = 8.0 mol%	70.02
x = 5.0 & y = 10.0 mol%	66.85

The D value decreases with doping and co-doping of Sm^{3+} and Sm^{3+}/Eu^{3+} ions in CBP. Decrease in D values may be expected to the ionic radius discrepancy amongst Sm^{3+} (r = 0.95Å for coordination number: CN = 6), Eu^{3+} (r = 0.94 Å for CN = 6) and Bi^{3+} (r = 1.03 Å for CN = 6) ions, which also recommends that the successful incorporation of RE ions in CBP host. Also, the acceptable radii variation amongst doped and substituted ions was less than the limits of 30%.

The Rietveld refinement has been executed for the undoped CBP sample. Fig. 5.02 (a) represents the refinement pattern for the CBP sample. The refinement results of CBP have been endorsed single cubic phase crystallization and the resulting lattice parameters a = b = c = 9.893

Å and α = β = γ = 90°. The goodness of fit (χ^2) was found to be 1.90, which indicates the superiority of refinement. Fig. 5.02 (b) shows the unit cell structure of CBP prepared by executing the VESTA software. In CBP cubic structure, Ca, Bi, P and O atoms were occupied at $16c$, $16c$, $12a$ and $48e$ sites, respectively [92].

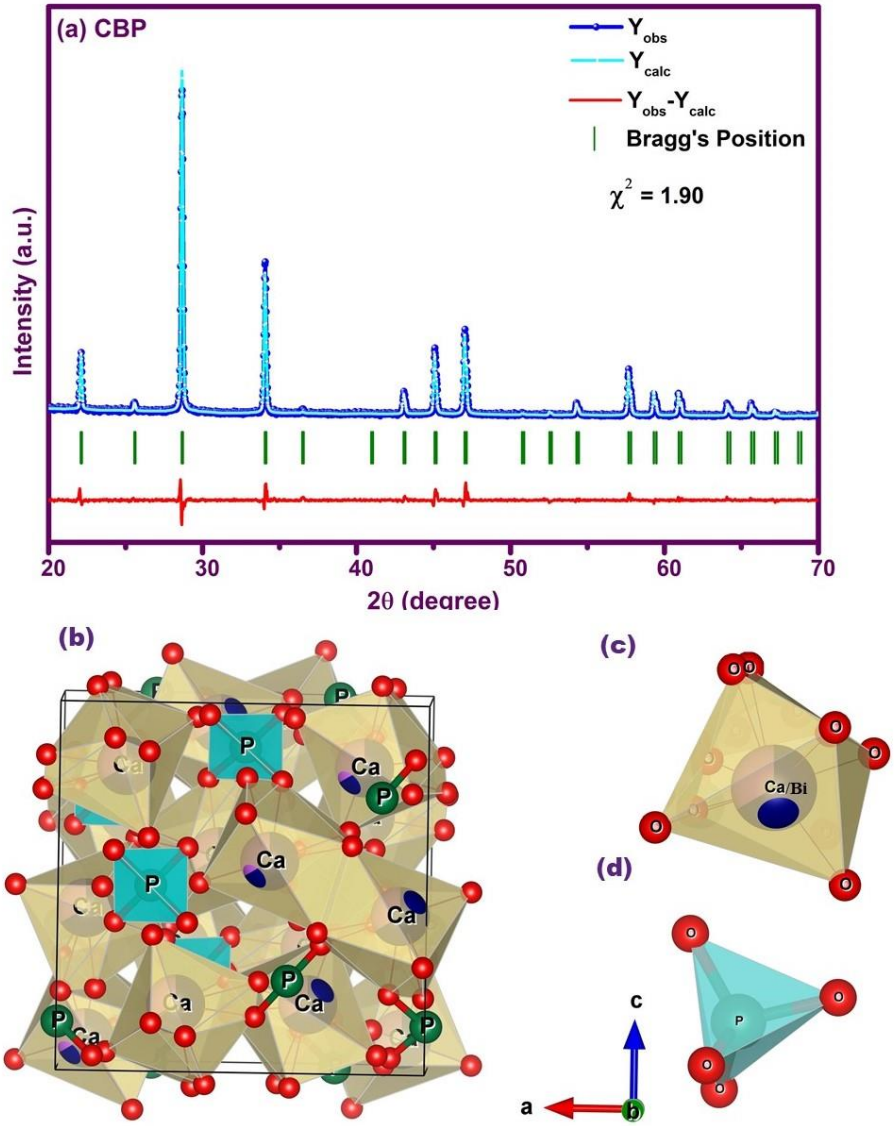

Fig. 5.02: *(a) Reitveld refinement pattern (b) unit cell structure of cubic CBP sample (c) octahedron shape of Ca bonded with O atoms and (d) tetrahedron shape of P bonded with O atoms.*

Table 5.2: Reitveld refinement results for cubic CBP sample.

Atoms	Wyckoff site	*x*	*y*	*z*
Ca	16c	0.07435	0.07435	0.07435
Bi	16c	0.07435	0.07435	0.07435
P	12a	0.37500	0.00000	0.25000
O1	48e	0.49323	0.37926	0.71356
O2	48e	0.59125	0.38070	0.72700

Atomic site and Wyckoff position are listed in Table 5.02. The occupation ratios of Bi and Ca ions in 16*c* site are 1/4 and 3/4, respectively and bonded with eight O atoms to form octahedron as shown in Fig. 5.02 (c). The O atoms separated into two positions and four O atoms bonded with one P atom to form three dimensional $[PO_4]^{3-}$ tetrahedron structure as displayed in Fig.5.02 (d).

5.3.2. Morphological Analysis

The morphology of the CBP particles examined using the SEM micrograph as displayed in Fig. 5.03 (a & b). The micrograph discloses that the sample consists of heterogenous structure with agglomeration of non-uniform particles. The CBP particle size was noticed in the range of around 1 μm.

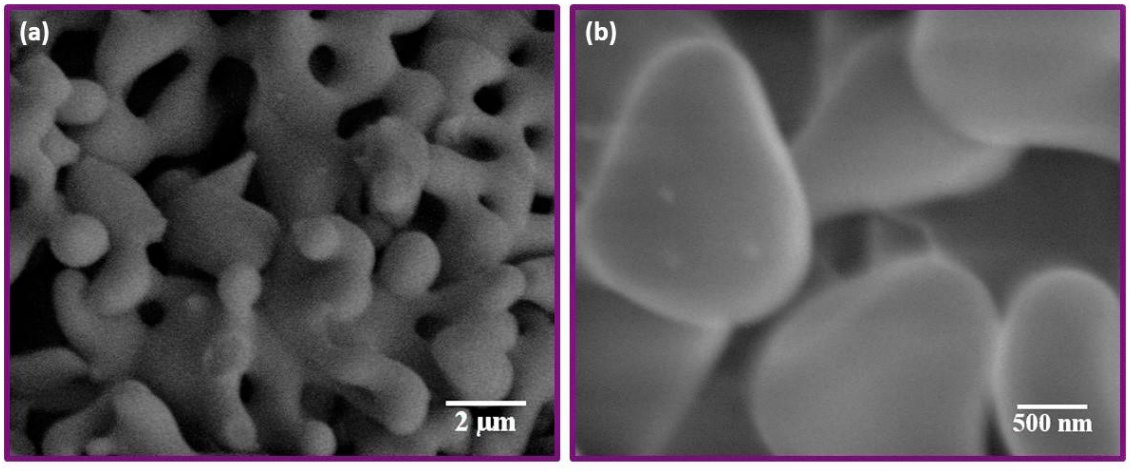

Fig. 5.03: *SEM micrographs for undoped CBP powder sample at different magnifications (a) 2 μm and (b) 500 nm.*

5.3.3. Photoluminescence Properties

Excitation spectra for Sm^{3+} ion (x =1.0 to 8.0 mol%) doped CBP phosphors were recorded with monitoring the emission at 598 nm wavelength. Excitation spectra demonstrated in Fig. 5.04 (a), which exhibit a series of excitation peaks corresponding to $4f - 4f$ transitions in 300 to 500 nm range. Excitation peaks at 325 ($^6H_{5/2}\rightarrow{}^4P_{1/2}$), 341 ($^6H_{5/2}\rightarrow{}^4H_{9/2}$), 358 ($^6H_{5/2}\rightarrow{}^4D_{3/2}$), 372 ($^6H_{5/2}\rightarrow{}^4D_{1/2}$), 400 ($^6H_{5/2}\rightarrow{}^4F_{7/2}$), 413 ($^6H_{5/2}\rightarrow{}^4M_{19/2}$), 437 ($^6H_{5/2}\rightarrow{}^4G_{9/2}$) and 466 nm ($^6H_{5/2}\rightarrow{}^4I_{11/2}+{}^4I_{13/2}+{}^4M_{15/2}$) were attributed to the distinctive transitions of Sm^{3+} ions [68,200]. The most populous peaks are noticed at 400 and 466 nm. Excitation intensity improved with the Sm^{3+} ion doping concentration up to x = 5.0 mol% and afterward reduced.

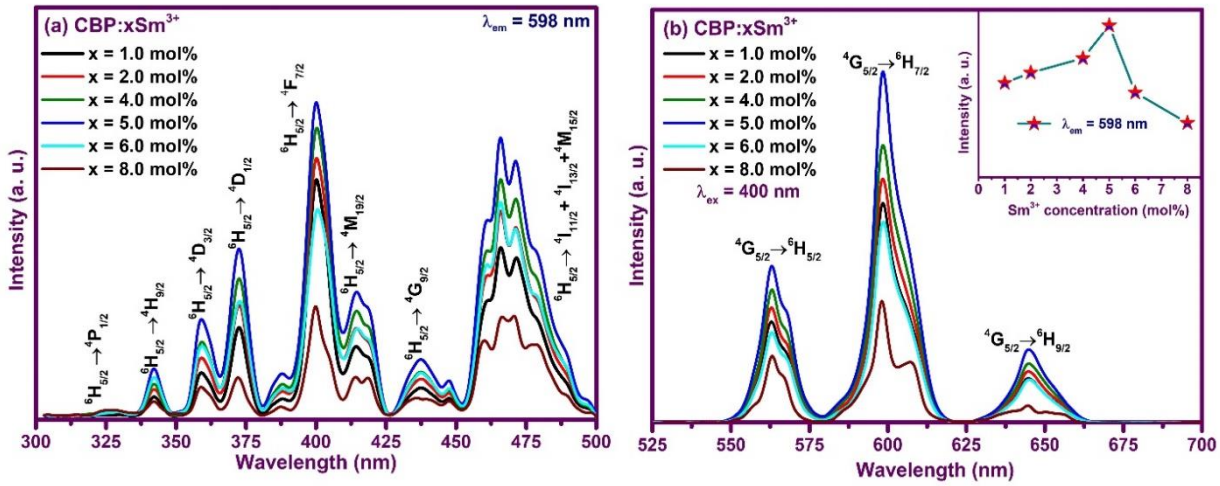

Fig. 5.04: *(a) Excitation spectra measured at λ_{em} = 598 nm, (b) Emission spectra under λ_{ex} = 400 nm for CBP:xSm^{3+} (x = 1.0, 2.0, 4.0, 5.0, 6.0 and 8.0 mol%) phosphor.*

Emission spectra for CBP:xSm^{3+} were recorded under 400 nm excitation wavelengths as depicted in Fig.5.04 (b). Three emission peaks were spotted at 562, 598 and 644 nm, which are evolving due to $^4G_{5/2}\rightarrow{}^6H_{5/2}$, $^4G_{5/2}\rightarrow{}^6H_{7/2}$ and $^4G_{5/2}\rightarrow{}^6H_{9/2}$ distinctive transitions of Sm^{3+} ions [201]. The first peak at 562 nm ($^4G_{5/2}\rightarrow{}^6H_{5/2}$) is purely MD transition, which abides by the

$\Delta J = 0, \pm 1$ selection rule and unaffected from crystal felid environment. The second peak at 598 nm ($^4G_{5/2} \rightarrow {}^6H_{7/2}$) is due to both partially MD and partially forced ED transition but only abide by $\Delta J = \pm 1$ selection rule. Whereas the third peak at 644 nm ($^4G_{5/2} \rightarrow {}^6H_{9/2}$) is purely forced ED transition follow the selection rule $\Delta J \leq \pm 6$, which is hypersensitive in nature and strongly influenced by crystal felid environment [200, 202]. The intensity fraction of ED with MD, indicates symmetry of the local environment of dopant ions in the host lattice. In this phosphor, the ED transition is less intense than MD transition, which reveals that higher environmental symmetry of Sm^{3+} ions with an inversion center in CBP host lattice.

Emission intensity enhances with an increase in the Sm^{3+} ion doping concentration and reaches its highest intensity at the concentration of 5.0 mol% and after that, the concentration quenching effect emerges. Inset image of Fig. 5.04 (b) signifies the intensity variation concerning with Sm^{3+} ion doping concentration, which also confirms that the 5.0 mol% Sm^{3+}ion doped CBP phosphor gives the highest emission intensity under the 400 nm excitation wavelength. As a result, the optimized doping concentration of Sm^{3+} ion in CBP host is x = 5.0 mol%.

The concentration quenching may be evolved due to a very less critical distance between doping ions and escalation in the possibility of non-radiative energy transfer among the nearest doping ions. The critical distance was evaluated and found to be 20.82 Å, as per the formula provided by Blasse [63]. Larger value (≥5 Å) of critical distance discloses the quenching is attributed to the multipole interaction among the Sm^{3+} ions. Type of multipolar interaction was identified via Dexter's theory having modified formula as defined in equation number (1.02), section 1.3.3 of chapter 1 [203, 204].

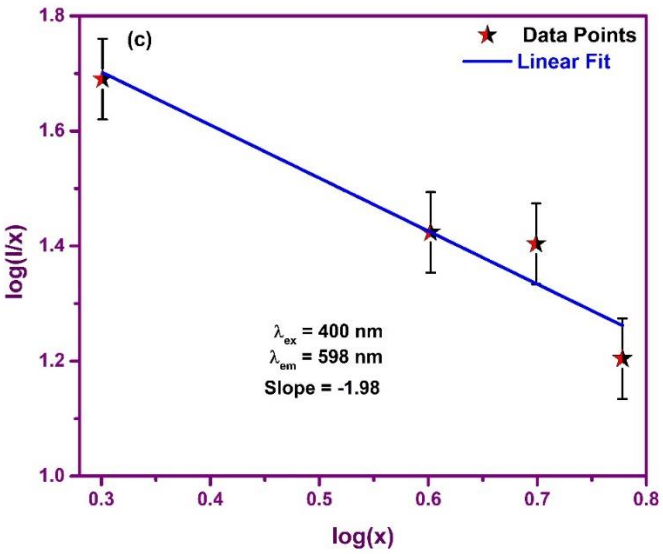

Fig. 5.04. *(c) plot between log (I/x) and log(x).*

Fig. 5.04 (c) represents the Dexter's plot between $log(I/x)$ and $log\ (x)$ and the linear fitted slope is -1.98. The Q value was retrieved to be 5.94, which is close to 6. Henceforth, the multipolar interaction in Sm^{3+} doped CBP is dipole-dipole type.

To reveal the possibility to enhance emission profile and expand the excitation spectra of Sm^{3+} ions, co-dopant (Eu^{3+}) ion has been included to synthesize CBP phosphors with fixed Sm^{3+} ion concentration (i.e., optimized: x = 5.0 mol%) by varying the Eu^{3+} ion concentration (y = 0.0 to 10.0 mol%). Fig. 5.05 (a) shows the excitation spectra of CBP: yEu^{3+} (y = 1.0 mol%) and CBP: xSm^{3+}, yEu^{3+} (x = 5.0 mol% y = 1.0 mol%) with monitoring the emission at λ_{em} = 612 nm. Also, the excitation spectrum was recorded for CBP: xSm^{3+}, yEu^{3+} (x = 5.0 mol%, y = 1.0 mol%) with monitoring λ_{em} = 598 nm. Excitation spectrum of CBP: yEu^{3+} (y = 1.0 mol%) exhibits a series of peaks at 316, 359, 380, 391, 414 and 462 nm attributed to $f - f$ transitions of Eu^{3+} ions. Excitation spectrum for the CBP: xSm^{3+}, yEu^{3+} (x = 5.0 mol%, y = 1.0 mol%) monitoring with λ_{em} = 612 nm shows a number of peaks due to Eu^{3+} ions along with other

several peaks due to Sm^{3+} ions, also the intensity got improved than the CBP: yEu^{3+} (y = 1.0 mol%).

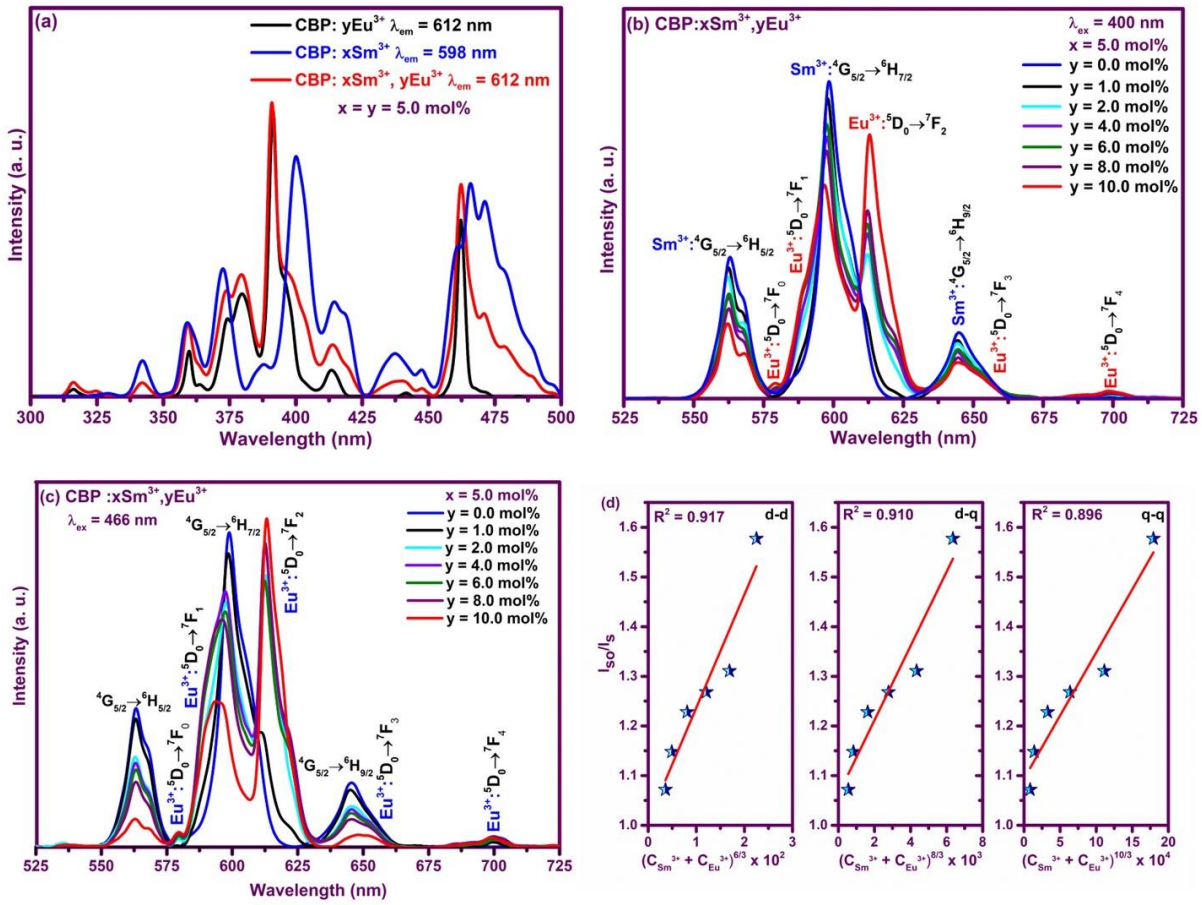

Fig. 5.05: *(a) Black and red solid lines represent the excitation spectrum of CBP: yEu^{3+} phosphor (y = 1.0 mol%, λ_{em} = 612 nm) and CBP:xSm^{3+}, yEu^{3+} phosphor (x = 5.0 & y = 1.0 mol%, λ_{em} = 612 nm), respectively. Blue line show the excitation spectrum for CBP:xSm^{3+}, yEu^{3+} phosphor (x = 5.0 mol%, y = 1.0 mol%) with monitoring λ_{em} = 598 nm. Emission spectra under (b) λ_{ex} = 400 nm (c) λ_{ex} = 466 for CBP:xSm^{3+}, yEu^{3+} (x = 5.0 & y = 0.0 to 10.0 mol%) (d) Dependence of I_{SO}/I_S of Sm^{3+} on $(C_{Sm+Eu})^{6/3}$, $(C_{Sm+Eu})^{8/3}$ and $(C_{Sm+Eu})^{10/3}$*

Excitation peaks were taking place at 341, 372, 400, 441 and broad peak observed from 457 to 495 nm, attributed to the $^6H_{5/2} \rightarrow {}^4H_{9/2}$, $^6H_{5/2} \rightarrow {}^4D_{1/2}$, $^6H_{5/2} \rightarrow {}^4F_{7/2,}$ $^6H_{5/2} \rightarrow {}^4G_{9/2}$ and $^6H_{5/2} \rightarrow {}^4I_{11/2} + {}^4I_{13/2} + {}^4M_{15/2}$ transitions of Sm^{3+} ions, respectively. Excitation spectra of CBP: xSm^{3+}, yEu^{3+} (x = 5.0 mol%, y = 1.0 mol%) monitoring with λ_{em} = 598 nm is similar with the excitation spectra of CBP: xSm^{3+} phosphor as presented in Fig. 5.04 (a).

In accordance with the excitation spectra, emission spectra for CBP:xSm^{3+}, yEu^{3+} phosphors were recorded under λ_{ex} = 400 and 466 nm excitation wavelengths as illustrated in Fig. 5.05 (b & c). The strongest emission peak observed at 598 nm ($^4G_{5/2} \rightarrow {}^6H_{7/2}$) is due to Sm^{3+} ions, when the Eu^{3+} concentration is low (i.e., y= 0.0 and 1.0 mol%). Further, the intensity related to $^4G_{5/2} \rightarrow {}^6H_{7/2}$ transition of Sm^{3+} ions is considerably dropped with the increasing Eu^{3+} concentration caused by the energy transfer from Sm^{3+} sensitizer to activator Eu^{3+} ions [56,199]. However, the emission intensity related to Eu^{3+} ion improves with increasing the Eu^{3+} ion content from 1.0 to 10.0 mol% and at this concentration of Eu^{3+} ion quenching was not observed. In Fig. 5.05 (b & c), the analogous patterns were spotted for the emission spectra of CBP:xSm^{3+}, yEu^{3+} phosphor excited at 400 and 466 nm with slight intensity variation. The studied results suggest that the energy transfer observed from the sensitizer Sm^{3+} ions to activator Eu^{3+} ions under λ_{ex} = 400 and 466 nm.

The exchange and multipolar interaction are the two ways of energy transfer between sensitizer and activator ions. As per the expression given by Dexter's for multipolar interaction and Reisfeld's estimation, the fraction of the sensitizer emission intensity without activator ion to emission intensity of sensitizer with activator ion can be acquired as [205]:

$$\frac{I_{SO}}{I_S} \propto C^{n/3} \tag{5.01}$$

where I_{SO} is the emission intensity of sensitizer Sm^{3+} ion only and I_S is the emission intensity of Sm^{3+} with activator Eu^{3+} ions. *C* denotes the sum of Sm^{3+} sensitizer and Eu^{3+} activator ions concentration in mol%. The parameter '*n'* belongs to the type of multipolar interaction, having values are 10, 8 and 6 associated to (q-q) quadrupole-quadrupole, (d-q) dipole-quadrupole, and (d-d) dipole-dipole interactions, respectively [205]. Fig. 5.05 (d) shows the plot between I_{SO}/I_S and $C^{n/3}$ for d-d, d-q and q-q interactions under the excitation wavelength of λ_{ex} = 400 nm. The best linear fit has been acquired for I_{SO}/I_S versus $C^{6/3}$ plot having n = 6, which recommends that the energy transfer from sensitizer Sm^{3+} ions to activator Eu^{3+} ion is owing to dipole-dipole in nature.

The partial energy level diagram of Sm^{3+}, Eu^{3+} in CBP phosphor clarifies the ET process as presented in Fig. 5.06. The as-synthesized phosphor was effectively excited by specific near-UV/blue radiation and excited atoms from ground level to different excited energy levels. Subsequently, some non-radiative transitions take place in-between levels as mentioned by black dotted lines and give radiative emission in the visible region as explained in earlier PL properties. The energy difference between lowest excited $^4G_{5/2}$ (~17,924 cm^{-1}) level of Sm^{3+} ion and $^5D_0$ (~17,286 cm^{-1}) levels of Eu^{3+} ion was found to be 638 cm^{-1} [202]. As the energy difference is very less, the part of energy from $^4G_{5/2}$ level of Sm^{3+} ion was migrated to $^5D_0$ level of Eu^{3+} ions. The result evidently specifies that Sm^{3+} act as an effective sensitizer for the Eu^{3+} activator ion in CBP phosphor.

PL quantum yield is one of the most important parameters of phosphor to disclose practical utility in any optoelectronics devices. Hence, the PL quantum yield was evaluated for CBP:xSm^{3+}, yEu^{3+} (x =5.0 mol% & y = 10.0 mol%) phosphor with the of integrated under λ_{ex} = 448 nm and λ_{em} = 612 nm [206]. The PL quantum yield is found to be 86.65%, which is

higher than the commercial red phosphor $Y_2O_3:Eu^{3+}$ as well other reported phosphors [92,207,208]. The obtained PL characteristics of CBP:xSm^{3+}, yEu^{3+}

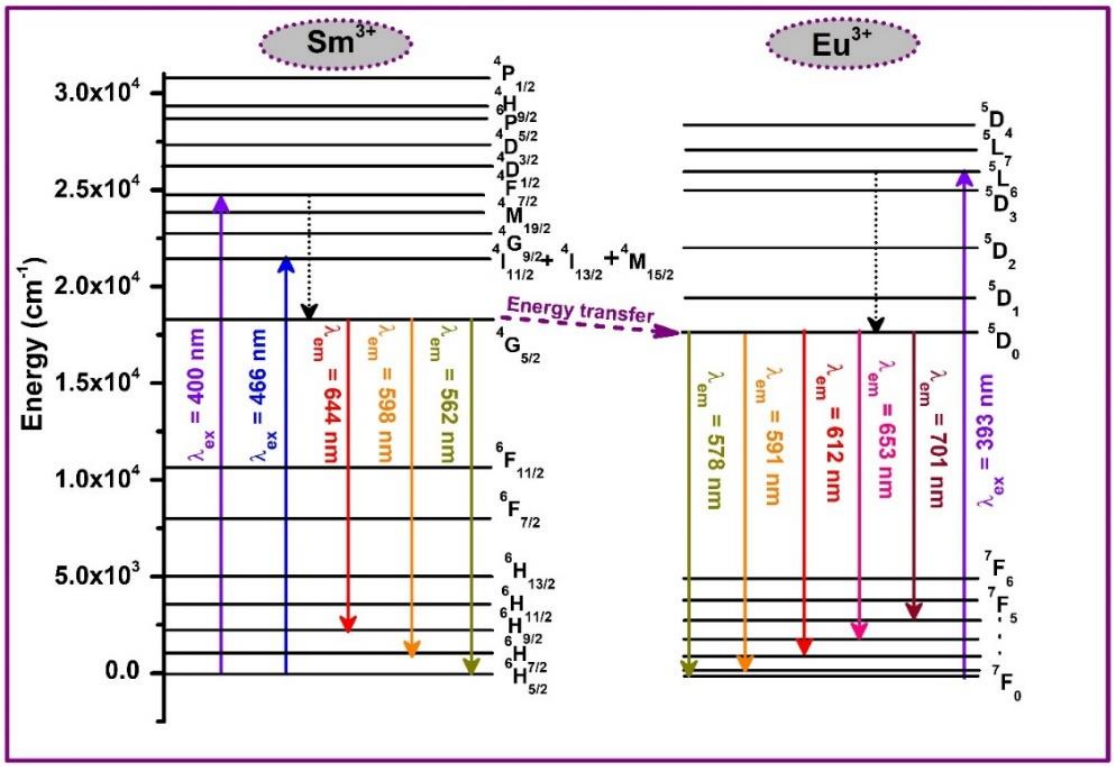

Fig. 5.06: *Partial energy level diagram presenting the energy transfer from sensitizer to activator in Sm^{3+}, Eu^{3+} co-doped CBP phosphor.*

phosphor with high value of PL quantum yield validate that the phosphor can be a potential red emitting component in pc-w-LEDs and other photonic devices.

5.3.4. Colorimetric Properties

The Commission Internationale de l'Eclairage (CIE) color coordinates for the synthesized phosphors have been evaluated by utilizing the emission spectra at λ_{ex} = 400 nm, which are tabulated in Table 5.03. The CIE color coordinates for the as-prepared co-doped CBP: xSm^{3+}, y Eu^{3+} (x =5.0 mol% & y = 0.0 to 10.0 mol%) phosphors can be seen from the Fig. 5.07. The

evaluated CIE color coordinates for CBP: xSm^{3+} (x = 5.0 mol%) phosphor were situated in orange region. The color coordinates were tuned towards red region with an increase in the Eu^{3+} ions concentration from 0.0 to 10.0 mol% in co-doped CBP phosphors. The inset of Fig. 5.07 depicts the variation in CIE coordinates from orange to red with an increase in the Eu^{3+} ion concentration from 0.0 to 10.0 mol% in the co-doped CBP phosphors. The aforementioned results reveal that the CBP: xSm^{3+}, yEu^{3+} phosphors have favorable characteristics for near-UV pumped tunable orange to red constituent to utilize in warm white LEDs and other photonic devices.

Table 5.3: CIE color coordinates, lifetime, ET efficiency of CBP:xSm^{3+}, yEu^{3+} (x = 5.0 & y = 0.0 to 10.0 mol%) phosphors at λ_{ex} = 400 and λ_{em} = 598 nm.

CBP:xSm^{3+}, yEu^{3+} Phosphors (x = 5.0 mol%)	CIE color coordinates (x, y)	Lifetime (τ_{avg}) (ms)	ET efficiency η_T (%)
y = 0.0 mol%	(0.572, 0.426)	2.453	-
y = 1.0 mol%	(0.576, 0.422)	2.365	3.58
y = 2.0 mol%	(0.584, 0.415)	2.193	10.59
y = 4.0 mol%	(0.592, 0.406)	1.978	19.36
y = 6.0 mol%	(0.593, 0.406)	1.946	20.64
y = 8.0 mol%	(0.596, 0.402)	1.754	28.49
y = 10.0 mol%	(0.607, 0.392)	1.368	44.20

5.3.5. Decay Time Analysis

To examine the energy transfer mechanism from sensitizer to activator, the decay curves of $^4G_{5/2} \rightarrow {}^6H_{7/2}$ for the CBP:xSm^{3+}, yEu^{3+} (x = 5.0 mol% & y = 0.0 to 10.0 mol%) phosphors were recorded with the wavelength of λ_{em} = 598 nm and λ_{ex} = 400 nm.

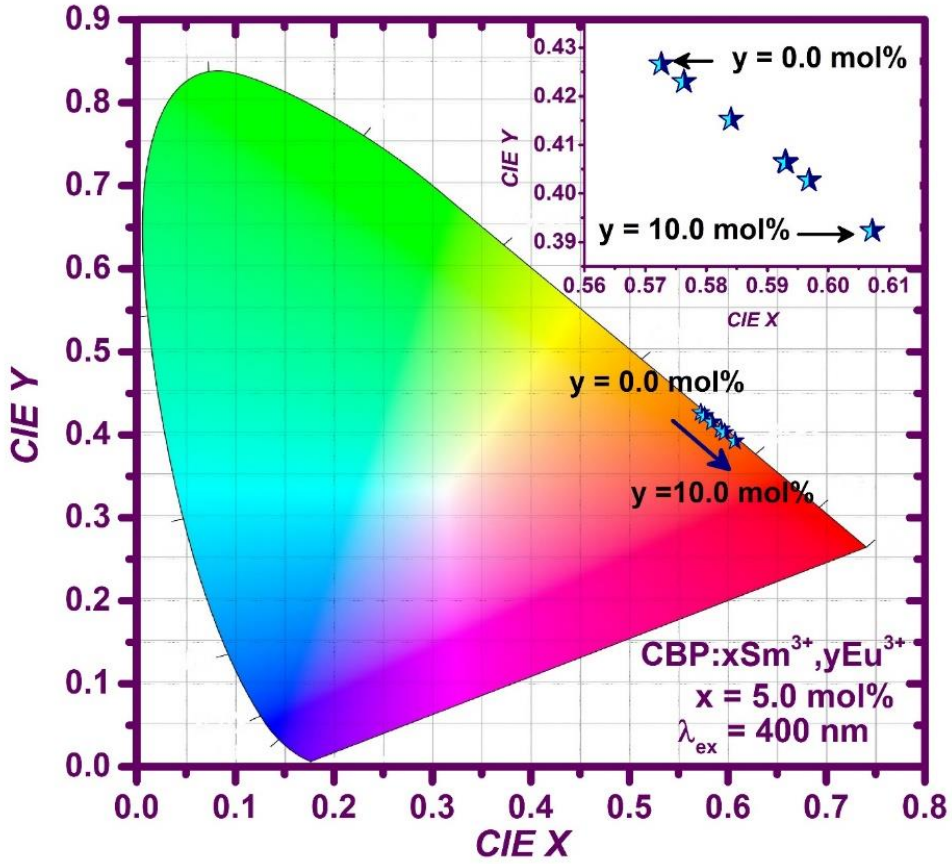

Fig. 5.07: *CIE plot for CBP:xSm^{3+}, yEu^{3+} phosphor (x = 5.0 & y = 0.0 to 10.0 mol%) at λ_{ex} = 400 nm. Inset plot reveals the color coordinate modulation with increasing Eu^{3+} concentration from 0.0 to 10.0 mol%.*

Fig. 5.08 (a) demonstrates that the decay profile rapidly reduces with an increase of Eu^{3+} activator ions content, which is a solid confirmation of a part of energy migrates from Sm^{3+} to Eu^{3+} ions. The decay curves exhibit exponential nature and best fitted with the bi-exponential equation as mentioned in equation number (2.06) in section 2.3.7 of chapter 2.

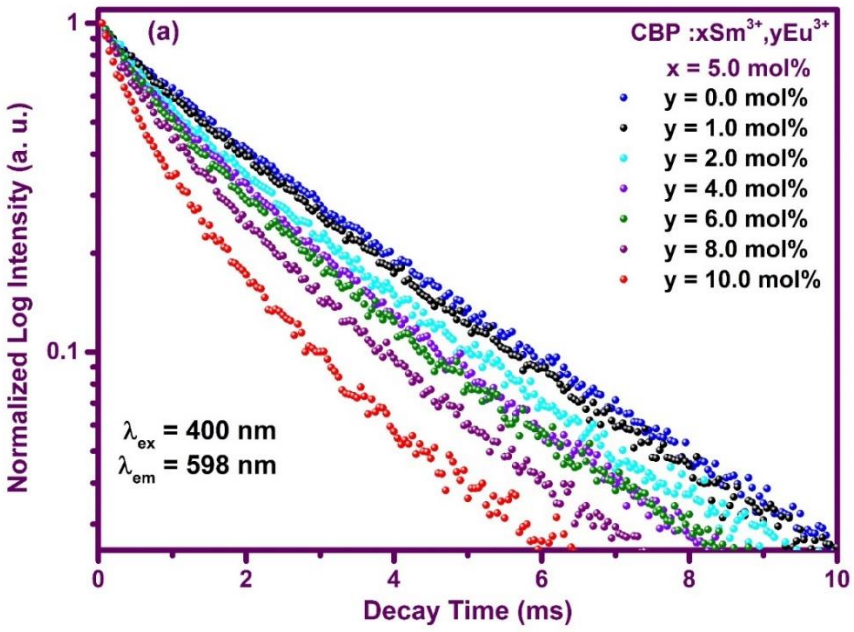

Fig. 5.08: *(a) Decay curves for CBP:xSm^{3+}, yEu^{3+} phosphor with varying Eu^{3+} concentration (x = 5.0 & y = 0.0 to 10.0 mol%) at λ_{ex} = 400 and λ_{em} = 598 nm.*

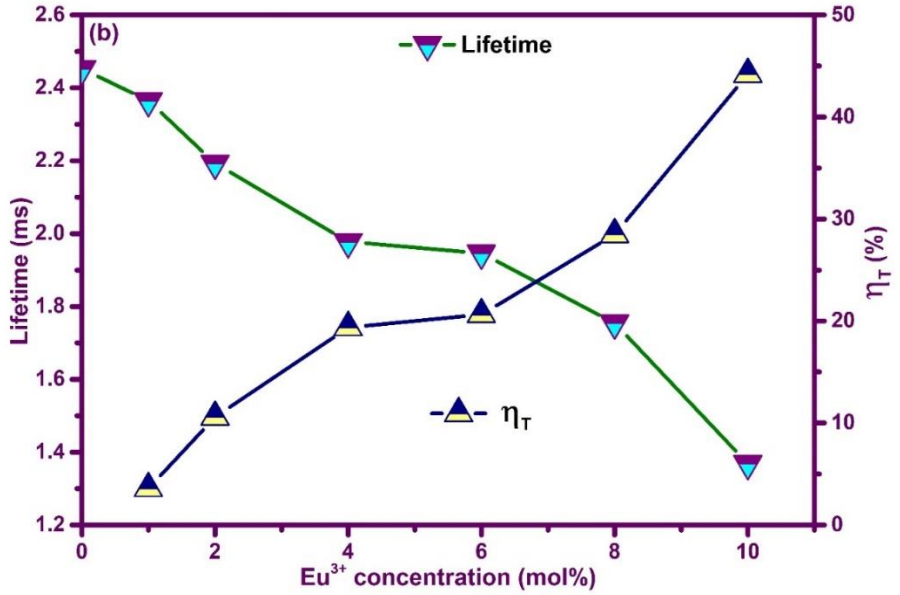

Fig. 5.08: *(b) Variation of lifetime value and ET efficiency with increases Eu^{3+} concentration from 0.0 to 10.0 mol%.*

The average lifetime (τ_{avg}) has been determined by applying formula as presented in equation number (2.07) in section 2.3.7 of chapter 2 [209,210]. The τ_{avg} (ms) values are tabulated in Table 5.03 with increasing Eu^{3+} concentration. It was noticed that the value of average lifetime for co-doped phosphors decreases with surge in the Eu^{3+} concentration as shown in Fig. 5.08 (b). The energy transfer (η_T) efficiency was calculated using τ_{avg} value in the following equation [211]:

$$\eta_T(\%) = \left(1 - \frac{\tau_d}{\tau_{d0}}\right) \times 100 \tag{5.02}$$

where, τ_{d0} and τ_d signifies the average lifetime time in ms of CBP: xSm^{3+},yEu^{3+} phosphor in the absence of Eu^{3+} ions (i.e., y = 0.0 mol%) and existence of the Eu^{3+} ions, respectively. The η_T values are presented in Table 5.03. A plot perceiving the variation in lifetime and η_T values with increasing Eu^{3+} concentration as illustrated in Fig. 5.08 (b). It has been observed that η_T value improves with Eu^{3+} ion concentration, which implies a part of energy transfer from Sm^{3+} to Eu^{3+} ions. The η_T value in terms of percentage enhanced from 3.58 to 44.20 % with the increase in Eu^{3+} ion concentration from 1.0 to 10.0 mol% in CBP: xSm^{3+}, yEu^{3+} phosphor. The enhancement in η_T value signifying that with the surge in Eu^{3+} concentration, more and more energy is transferred from sensitizer Sm^{3+} to activator Eu^{3+} ion.

5.3.6. Thermal Stability of CBP: xSm^{3+}, yEu^{3+} Phosphor

Thermal stability is one of the important factors for phosphor to use as active component in many appliances. So, the emission spectra were recorded with temperature rise from environmental temperature 32 to 200 °C under the excitation wavelength of λ_{ex} = 400 nm. The emission spectra for the CBP:xSm^{3+}, yEu^{3+} (x = 5.0 & y = 10.0 mol%) at different temperatures were exhibited in Fig. 5.09 (a). The intensity of the emission profile declines with increasing

temperature. The emission intensity declined to 81.27% at 150 °C and 70.37% at 200 °C of initial intensity at 32 °C, which reveals that the as-prepared phosphor has higher thermal stability. In addition, the activation energy (ΔE) is calculated via formula expressed by Arrhenius and described in equation number (2.08) in section 2.3.8 of chapter 2 [212]. The $ln[(I_o/I_T)-1]$ versus $1/K_BT$ plot has been prepared and linearly fitted, which provides ΔE value and the resultant plot is shown in Fig. 5.09 (b). The ΔE value was noted as 0.217 eV for CBP:xSm^{3+}, yEu^{3+} (x = 5.0 & y = 10.0 mol%). The obtained activation energy was higher than the reported $Na_4CaSi_3O_9$:Sm^{3+}, Eu^{3+} (ΔE = 0.114 eV) and $Ca_9La(PO_4)_7$:Sm^{3+} (ΔE = 0.167 eV) and $Lu_2Ge_2O_7$:Bi^{3+},Sm^{3+} (ΔE = 0.114 eV) phosphors [213–215]. Hence, the as prepared phosphor has excellent thermal stability.

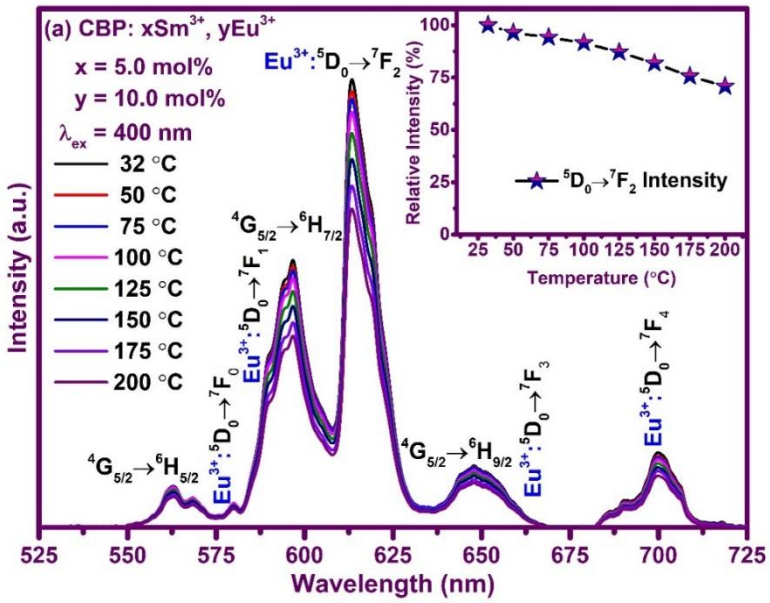

Fig. 5.09: *(a) Emission intensity variation with temperature for CBP:xSm^{3+}, yEu^{3+} (x = 5.0 & y = 10.0 mol%) under λ_{ex} = 400 nm. The inset reveals the relative emission intensity variation with rise in temperature from 32 to 200 °C.*

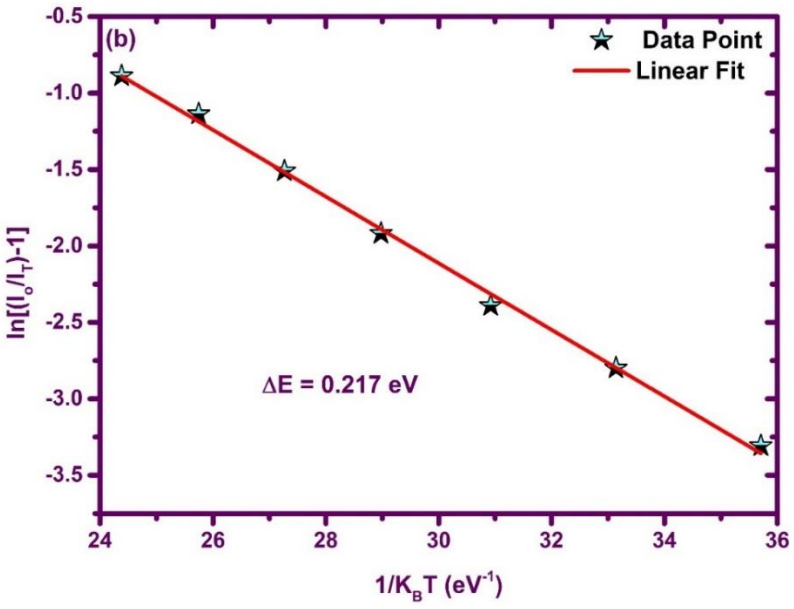

Fig. 5.09: *(b) plot between* $In[(I_o/I_T)-1]$ *versus* $1/K_BT$.

5.4. Conclusions

In summary, the tunable orange to red-emitting CBP:Sm^{3+}, Eu^{3+} phosphors have been efficiently synthesized by employing co-precipitation technique. The XRD and refinement results reveal the pure and single phase of CBP crystallizes in cubic structure. The CBP:Sm^{3+} phosphor is properly pumped by the near-UV and blue radiation and emit in the orange region. PL spectra of co-doped phosphors at λ_{ex} = 400 nm were found that the emission peak intensities of Sm^{3+} ions are reduced when increasing Eu^{3+} concentration, simultaneously enhancing the Eu^{3+} ions emission peak intensity. The lifetime values for CBP:Sm^{3+}, Eu^{3+} phosphors reduce with increase in the Eu^{3+} content under 400 nm excitation, which suggest ET between the Sm^{3+} to Eu^{3+} ions. The dipole-dipole nature of ET interaction was takes place in CBP phosphors, which was verified by applying Dexter and Reisfeld's theory. The PL quantum yield for CBP:Sm^{3+}, Eu^{3+} phosphor was found to be 86.65 %, which is higher than the commercial phosphors, demonstrating that the as prepared phosphor can be a probable red-emitting

constituent in photonic devices. The CIE color coordinates modulate from orange to red region with Eu^{3+} ions concentration under 400 nm excitation. The emission profile with varying temperature, signifies excellent thermal stability of the as synthesized CBP:Sm^{3+}, Eu^{3+} phosphor. The prominent results with optimum PL recommend that CBP phosphors will be useful for various fascinating applications in the field of displays, inorganic w-LEDs, solar cells and other photonic devices.

CHAPTER 6

Temperature-Dependent PL and Optical Thermometry Performance in $Ca_3Bi(PO_4)_3:Er^{3+}$ Phosphor

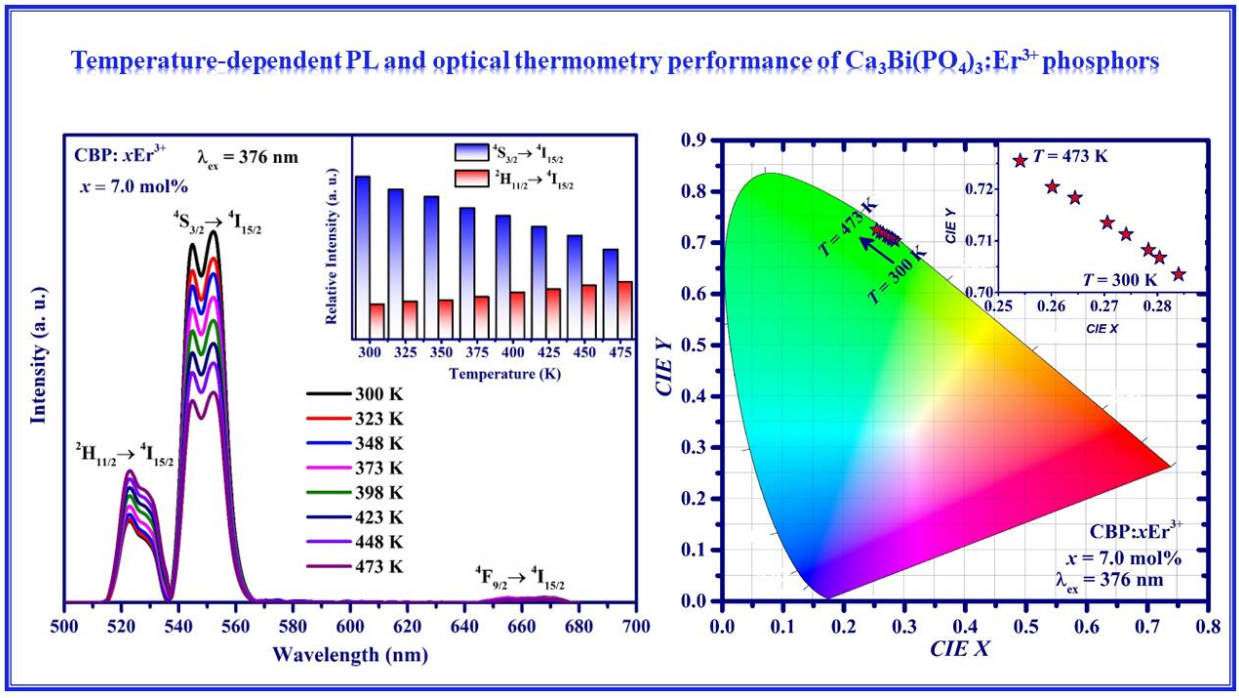

Part of this work has been published in Solid State Sciences, 131 (2022) 106956 (IF: 3.752)

6.1. Introduction

In the current times, the rare earth/transition metal induced luminescent materials based photonic devices have been swiftly growing and brought enormous advances around the world. This global innovation creates an ever-increasing demand for transformative photonic devices to fulfill the required applications [216–218]. The application of photonic devices is abundant in all sectors ranging from advanced science & technology, industries to daily life tasks. The ever-growing demand and variety of applications for luminescent materials have inspired the researcher to improve the existing features of phosphors. These luminescent materials have found a wide range of applications in extensive fields such as lasers, advanced displays, solid state lighting, optical storage, sensing and many more [219,220].

One of the prime applications of photonic devices is to sense the real-time temperature with high accuracy as the temperature is an essential and fundamental parameter used to define biological, chemical and physical processes [221,222]. The temperature sensors can measure the temperature in an effective ubiquitous way in all the investigations in the fields of engineering, science and medical. Also, the phosphor based temperature sensor provides access to extract more comprehensive data in environments where traditional electrical sensors are unreliable [216,223]. Phosphor thermometry is one of the advanced surface temperature measurement techniques that employ the photoluminescence characteristics of rare earth/transition metal incorporated crystalline/amorphous materials [224,225]. Rare-earth ions have drawn lots of consideration owing to their electron transitions within the $4f$ shell and high sensitivity to the composition [226,227]. For the optical thermometric applications, thermally coupled energy levels of rare earth ions were most useful to satisfy the exponential Boltzmann distribution law. Among the various rare-earth ions, Er^{3+} ions have thermally coupled energy

levels, i.e., $^2H_{11/2}$ and $^4S_{3/2}$ levels, which give non-overlapping emission peaks in the visible region [53,228]. These properties of rare earth ions with an appropriate host can be effectively apply to sense the temperature by probing the fluorescence intensity ratio (FIR) of the thermally coupled energy levels [224,228].

In order to obtain an efficient thermographic phosphor, it is critical to choose an appropriate host material. In numerous stable inorganic hosts, orthophosphate is one of the excellent host materials owing to their exceptional characteristics, i.e., lower synthesis temperature, large bandgap, chemical and thermal stability, good optical characteristics [87,109,148]. In orthophosphate, eulytite-type host formulated as $A_3B(PO_4)_3$ (A = alkaline earth, B = Bi^{3+}, Y^{3+}, In^{3+} etc.) exhibits good optical characteristics, thermal and chemical stability with high incorporation of RE ions in the lattice [86,90]. The eulytite-type orthophosphate's excellent optical properties with low phonon energy attract significant attention among the scientific community. Hence, the numerous lanthanides activated eulytite-type orthophosphates have been prepared and reported for photonic device applications. One eulytite-type orthophosphate is $Ca_3Bi(PO_4)_3$, having a wide optical band gap, decent optical properties, stable crystal structure, water-resistant property [92]. In recent years, different lanthanides doped $Ca_3Bi(PO_4)_3$ phosphors were synthesized via various methods and reported for possible use in many optoelectronic devices [98,194].

In the present chapter, a series of Er^{3+} ion-doped $Ca_3Bi(PO_4)_3$ phosphors have been prepared through co-precipitation route and characterized for potential applications in the photonic devices. The phase, crystallographic, morphological and optical characteristics of the synthesized phosphor were explored in detail. The average decay time of the synthesized sample was assessed through the time-resolved PL Curve. The effect of temperature on

variation in luminescence intensity was explored using the temperature-dependent photoluminescence (TDPL) profile. Finally, the prepared phosphor has been examined for the applicability in down-conversion based optical thermometry and w-LEDs.

6.2. Experimental Work

6.2.1. Preparation of CBP:Er^{3+} Samples

A systematic procedure was demonstrated in Fig. 2.03 for the preparation of CBP:Er^{3+} phosphor via employing chemical co-precipitation route and explained in detail in section 2.2.2 of chapter 2.

6.3. Results and Discussion

6.3.1. Structural analysis

The XRD patterns of CBP doped with Er^{3+} ions were demonstrated in Fig. 6.01. All XRD patterns were compared and found analogous with the standard data. The crystalline peaks were well indexed and indicate the pure phase formation of the samples. The CBP phase belongs to the well crystalline cubic crystal system with space group of $I\bar{4}3d$ (220) [90]. In the case of Er^{3+} doped CBP, no impurity peaks were observed in the diffraction patterns, which verifies that Er^{3+} ion is effectively immersed in the CBP host lattice. As per the ionic radii and valence states, Er^{3+} ions were predicted to sit in Bi^{3+} ion's place due to the minimum differences in their ionic radii and the analogous valence states. The percentage of ionic radii difference (D_r) between of host and dopant ions for VI coordination number was evaluated using the well known elementary formula [140]. The ionic radii of Bi^{3+} and Er^{3+} ions were 1.03 Å and 0.91 Å, respectively. The calculated D_r was found to be 11.65 %,

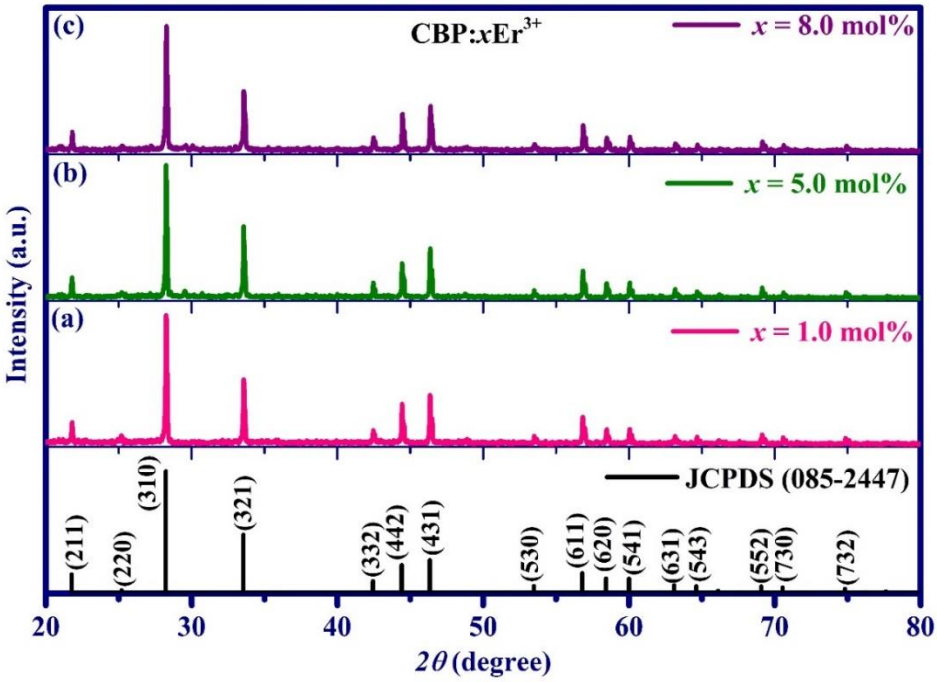

Fig. 6.01: *Diffraction patterns for standard JCPDS data (085-2447) compared with doped CBP: xEr^{3+} powder samples (a) x = 1.0 mol%, (b) x = 5.0 mol% and (c) x = 8.0 mol%, powder samples.*

significantly less within the acceptable percentage difference (30%). So, the small D_r Value reveals that the Er^{3+} ions were easily placed into the $Ca_3Bi(PO_4)_3$ host matrix by replacing the Bi^{3+} ions.

Microstrain and crystallite size were influenced the fullwidth at half maxima (β) value of the crystalline sample. Therefore, with the help of β value, the average crystallite size and microstrain for all the prepared samples were calculated using the Williamson-Hall equation number (2.03) in section 2.3.1 of chapter 2 [57,116]. The acquired average D values and microstrain were estimated using the plot shown in Fig. 6.02 and tabulated in Table 6.1. The average D value for 1.0 mol% Er^{3+} doped CBP samples was estimated to be 47.61 nm. The

average *D* value reduces with an increase in doping concentration of Er^{3+} ions as unveiled from Table 6.1.

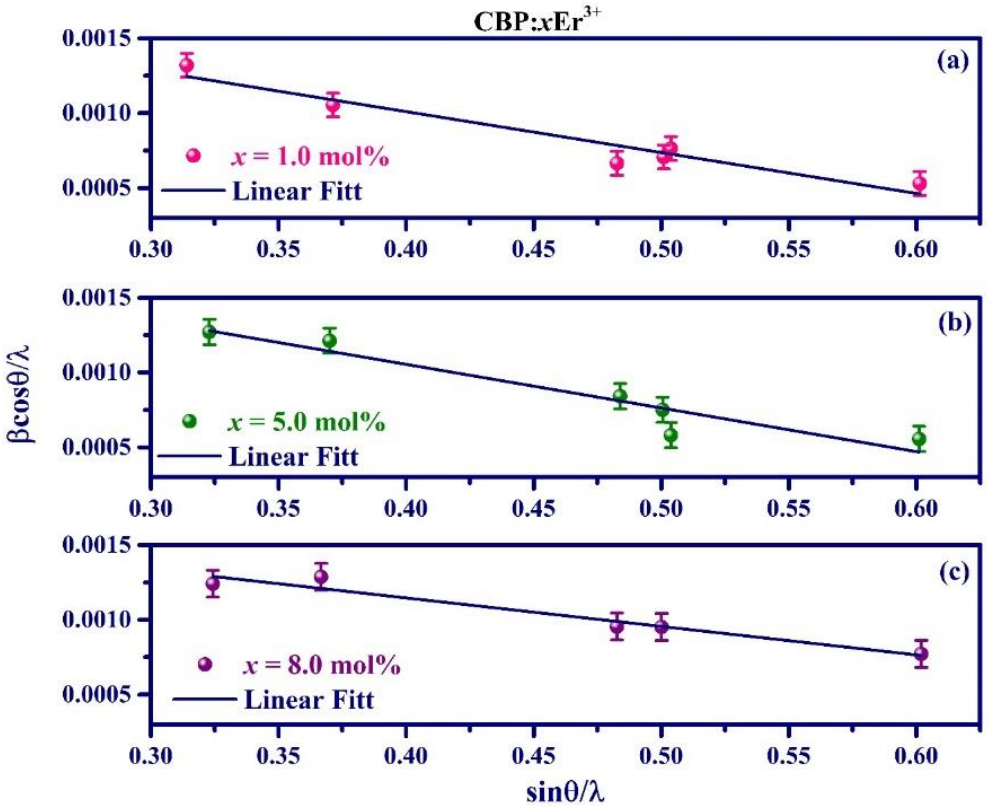

Fig. 6.02: *W-H plot for CBP: xEr^{3+} (a) x = 1.0, (b) x = 5.0 and (c) x = 8.0 mol%.*

Table 6.1: Crystallite size and microstrain of CBP: *x*Er^{3+} sample assessed using W-H equation.

Sample CBP: *x*Er^{3+}	Crystallite Size, D (nm)	Microstrain (ε) (x10^{-3})
x = 1.0 mol%	47.61	0.39
x = 5.0 mol%	45.45	0.56
x = 8.0 mol%	44.95	0.61

The assessed values of microstrain for the Er^{3+} doped CBP samples were upsurge with increase in doping concentration. The reduction in average D and increase in microstrain value can be resulted due to the effective ionic radii differences between doping of Er^{3+} ions (r = 0.91 Å) and host Bi^{3+} (r = 1.03 Å) ions at VI coordination. These results also signify the incorporation of Er^{3+} ions in the place of Bi^{3+} ions without any change in the CBP phase and crystal structure.

6.3.2. Optical Bandgap Study

The diffuse reflectance profile for CBP doped with Er^{3+} ions was recorded in the range of 200 to 1600 nm, as demonstrated in Fig. 6.03. The prepared sample shows various peaks in n-UV, visible and near-infrared regions owing to characteristic transitions from $^4I_{15/2}$ level to different higher energy levels placed at 366 ($^4G_{9/2}$), 378 ($^4G_{11/2}$), 407 ($^2H_{9/2}$), 450 ($^4F_{5/2}$), 488 ($^4F_{7/2}$), 523 ($^2H_{11/2}$), 543 ($^4S_{3/2}$), 651 ($^4F_{9/2}$), 803 ($^4I_{9/2}$), 980 ($^4I_{11/2}$) and 1546 nm ($^4I_{13/2}$) due to the Er^{3+} ions doped CBP sample. The reflectance profile was used to estimate optical bandgap (E_g) with the help of the equation as described in equation numbers (2.04) and (2.05) in section 2.3.4 of chapter 2 [120,121]. The direct optical bandgap was estimated using the plot between $[F(R)h\nu]^2$ and $h\nu$ as given in the inset of Fig. 6.03. The direct E_g of CBP: $x$$Er^{3+}$ (x = 1.0 mol%) was calculated via extrapolating the slope to α = 0 and get the optical bandgap value of 4.32 eV, which is close with the direct optical bandgap of $Ca_3Bi(PO_4)_3$ host sample.

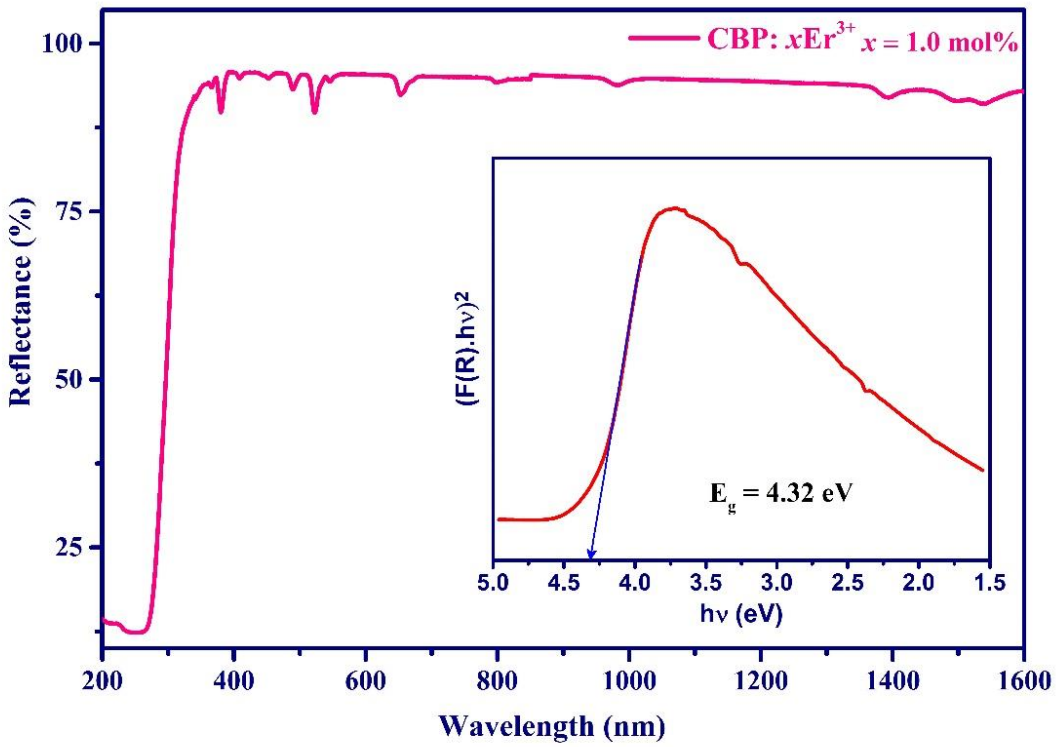

Fig. 6.03: *DRS spectra for CBP: xEr^{3+} (x = 1.0 mol%). Inset plot reveals the assessment of optical band gap using Kubelka-Munk function.*

6.3.3. Surface Morphological Analysis

The surface morphology of the CBP: $x\text{Er}^{3+}$ (x = 7.0 mol%) sample was studied using the help of FE-SEM micrographs as displayed in Fig. 6.04 (a & b). The morphology of CBP:Er^{3+} was asymmetrical spherical particles consists of some aggregation and formation of non-uniform bigger size particles. Fig. 6.04 (b) shows the dissimilar non-uniform particles of the prepared CBP:Er^{3+}sample. Fig. 6.04 (c) demonstrated the energy dispersive spectrum (EDS) along with elements present in the sample, which approves the existence of Er^{3+} doping ions in prepared CBP: $x\text{Er}^{3+}$ (x = 7.0 mol%) sample. Fig. 6.04 (d) indicates the elemental mapping image, which has been verified that the presence of calcium, bismuth, phosphorous, oxygen and uniform distribution of erbium ions in the prepared CBP: $x\text{Er}^{3+}$ sample.

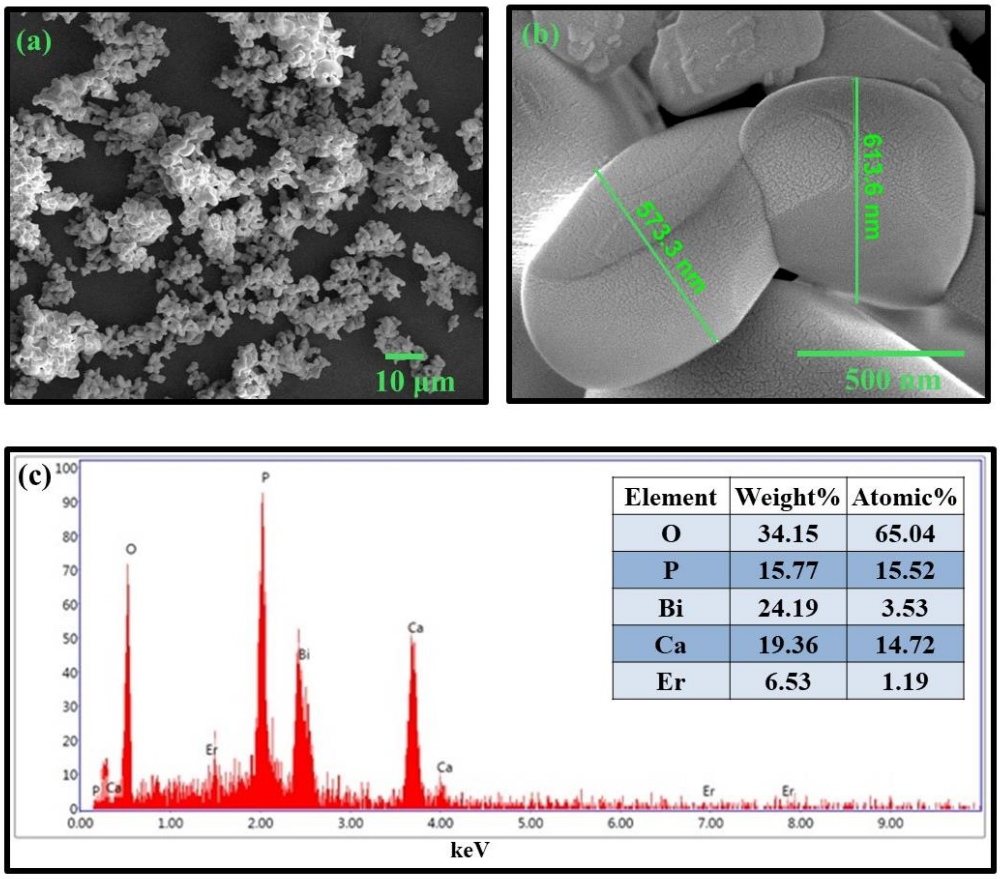

Element	Weight%	Atomic%
O	34.15	65.04
P	15.77	15.52
Bi	24.19	3.53
Ca	19.36	14.72
Er	6.53	1.19

Fig. 6.04: *FE-SEM micrograph for CBP: xEr^{3+} (x = 7.0 mol%) powder sample at different magnifications at (a) 10 µm and (b) 1 µm. (c) EDS spectrum. Inset table shows the weight% and atomic% of elements present in the sample.*

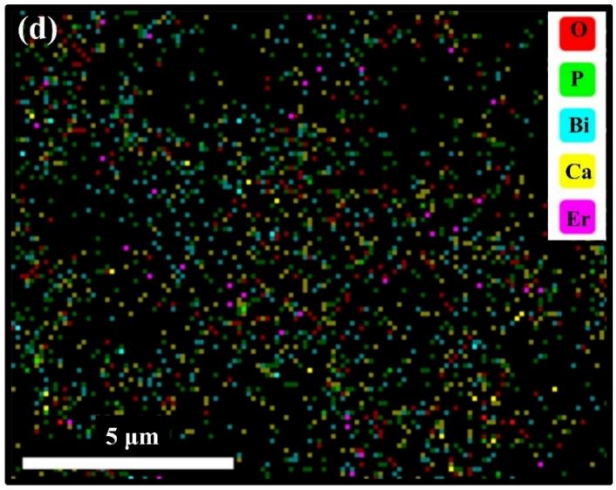

Fig. 6.04: *(d) Elemental mapping of CBP: xEr^{3+} (x = 7.0 mol%) powder sample.*

6.3.4. Analysis of PL Properties

The excitation profile for CBP: $x\text{Er}^{3+}$ (x = 1.0 mol%) phosphor was recorded at RT by monitoring the emission wavelength at 552 nm. Fig. 6.05 (a) illustrates the excitation spectrum, which exhibits a number of excitation peaks from 325 to 500 nm wavelength range. The peaks were centered at 358, 363, 376, 404, 448 and 486 nm interrelated to ($^4I_{15/2}\rightarrow{}^2K_{15/2}$), ($^4I_{15/2}\rightarrow{}^4G_{9/2}$), ($^4I_{15/2}\rightarrow{}^4G_{11/2}$), ($^4I_{15/2}\rightarrow{}^2H_{9/2}$), ($^4I_{15/2}\rightarrow{}^4F_{3/2}$), ($^4I_{15/2}\rightarrow{}^4F_{5/2}$), and ($^4I_{15/2}\rightarrow{}^4F_{7/2}$) transition of Er^{3+} ions, respectively [229]. Among these peaks, the most intense excitation peak was ascribed to ($^4I_{15/2}\rightarrow{}^4G_{11/2}$) transition at 376 nm wavelength. Therefore, the emission spectra were recorded under the excitation wavelength of 376 nm for all CBP: $x\text{Er}^{3+}$ phosphors.

The emission spectra for CBP: $x\text{Er}^{3+}$ phosphor at the excitation wavelength of 376 nm was illustrated in Fig. 6.05 (b). The emission spectra exhibit two significant peaks at 523, 552 nm and a minor peak at 662 nm corresponding to the transitions $^2H_{11/2}\rightarrow{}^4I_{15/2}$, $^4S_{3/2}\rightarrow{}^4I_{15/2}$ and $^4F_{9/2}\rightarrow{}^4I_{15/2}$ of Er^{3+} ions, respectively. Among these emission peaks, the most intense peak was observed at 552 nm ($^4S_{3/2}\rightarrow{}^4I_{15/2}$ transition) of Er^{3+} ions.

Emission intensity varies with the amount of doping ions concentration in any host lattice. In order to optimize the Er^{3+} ion concentration in CBP host, phosphor was prepared with varying concentration of Er^{3+} (x = 1.0 to 8.0 mol%). Fig. 6.05 (b) reveals the change in emission intensity with Er^{3+} ion concentration in CBP phosphor. Emission intensity improves with an upsurge in the amount of Er^{3+} ions doping in CBP host and the highest emission was observed at x = 7.0 mol%, beyond this concentration the emission intensity diminishes. The inset plot of Fig. 6.05 (b) confirms the emission intensity variation of $^4S_{3/2}\rightarrow{}^4I_{15/2}$ transition as

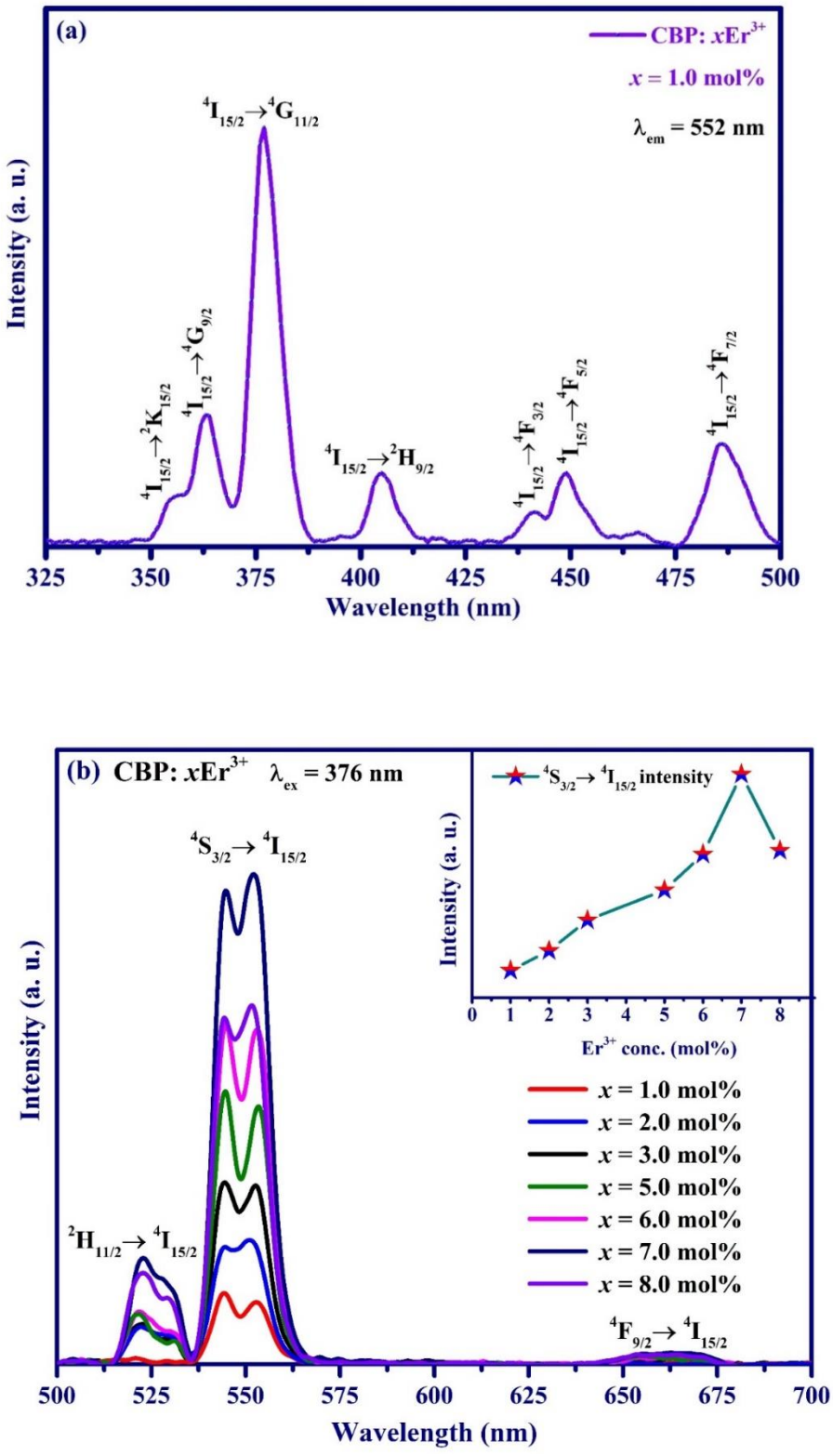

Fig. 6.05: *(a) Excitation spectrum of CBP:xEr^{3+} (x = 1.0 mol%) phosphor at λ_{em} = 552 nm. (b) Emission spectra of CBP:xEr^{3+} (x = 1.0-8.0 mol%) phosphor under λ_{ex} = 376 nm.*

a function of Er^{3+} ion doping concentration in CBP phosphor at an excitation wavelength of 376 nm. As the amount of doping increases beyond the 7.0 mol%, the distance among the nearest Er^{3+} ions may decrease, which intensifies the probability of non-radiative energy transfer among the nearest doping ions. The minimum distance is known as critical distance (R_c), the concentration quenching came into consideration below this distance. R_c for CBP:Er^{3+} phosphor has been assessed using the expression given by Blasse [63]:

$$R_c = 2\left(\frac{3V}{4\pi C_o N}\right)^{\frac{1}{3}} \quad (6.01)$$

where *V*, C_o and *N* signify the unit cell volume (V = 954.22 Å^3), activator ion concentration (C_o = 0.07 mol) and the number of the cation sites (N = 4) in the host unit cell, respectively. The R_c for CBP: *x*Er^{3+} phosphor was estimated to be 19.64 Å. The resultant (R_c >> 5 Å), suggested that the non-radiative energy transfer among the closest doping ions can be due to electric multipolar interaction.

6.3.5. Decay Time Analysis

The PL decay curves for CBP: *x*Er^{3+} (x = 7.0 mol%) phosphors were recorded at λ_{ex}= 376 nm and λ_{em}= 552 nm as shown in Fig. 6.06. The decay curve shows an exponential nature and well fitted with bi-exponential equations. The fitted bi-exponential equation is as described in equation number (2.06) in section 2.3.7 of chapter 2 [56,230]. The average decay time (τ_{avg}) for different CBP: *x*Er^{3+} (x = 7.0 mol%) phosphors were considered from the provided formula presented in equation number 2.07 in section 2.3.7 of chapter 2. The τ_{avg} for 7.0 mol% Er^{3+} doped CBP phosphor was 70 μs.

The Inokuti- Hirayama (I-H) model was applied on the PL decay curve. As per this model, decay curve is given by the equation as follows [49,231]:

$$I_t = I_0 \exp\{\frac{-t}{\tau_o} - Q\left(\frac{t}{\tau_o}\right)^{\frac{3}{s}}\} \quad (6.02)$$

in I-H model I_t is the emission intensity at time t sec, τ_o the lifetime value, respectively. Q denotes the energy transfer parameter.

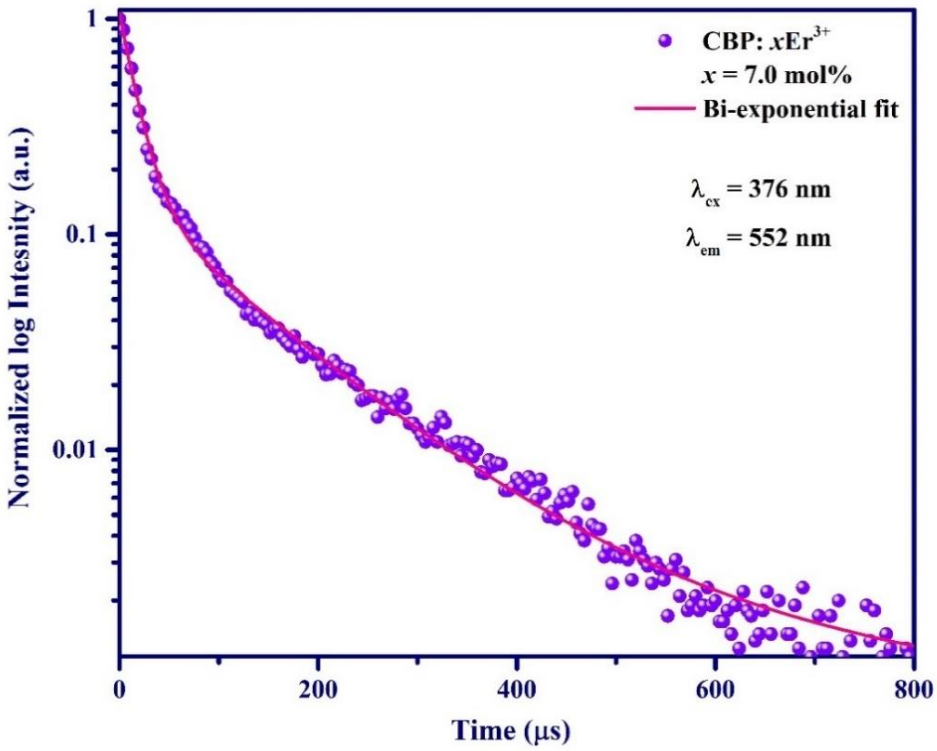

Fig. 6.06: *Decay curve of CBP:xEr^{3+} (x = 7.0 mol%) phosphor at λ_{ex} = 376 & λ_{em} = 552 nm.*

The value of *S* defines the type of multipole interaction with the values *S* = 6, 8 and 10 intended for dipole-dipole, dipole-quadrupole and quadrupole-quadrupole interactions among the Er^{3+} ions in CBP phosphor, respectively. Fig. 6.07 represent the decay curve with IH fitting for S=6, 8 & 10. The good fitting was observed for *S* = 6. Hence, the energy transfer mechanism is dipole-dipole in nature among the Er^{3+} ions in CBP phosphor.

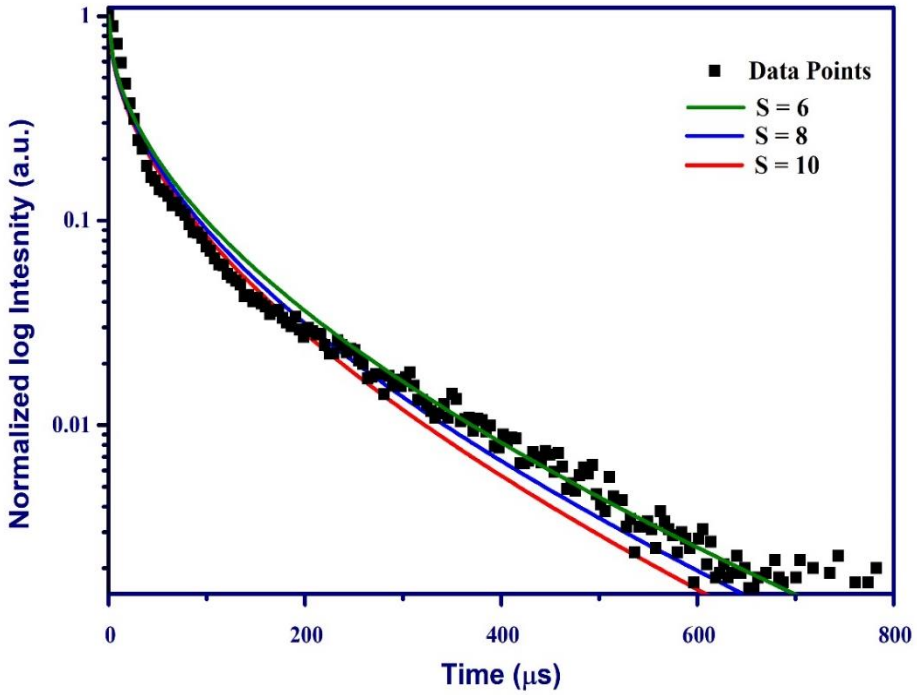

Fig. 6.07: *Decay curve of CBP:xEr^{3+} (x = 7.0 mol%) phosphor with I-H fitting at λ_{ex} = 376 and λ_{em} = 552 nm.*

6.3.6. Temperature Dependent PL Properties

The effect of temperature on the photoluminescence properties of phosphor materials is one of the significant features of the applicability of phosphor in many photonic applications. Typically, phosphors used in lighting devices require high thermal stability as the UV/blue LED chips generate temperature around 120 to 150 °C while operating time. Also, the thermal quenching features of the multipurpose phosphor can be applied on optical thermometric sensing devices. The thermal quenching performance of the Er^{3+} doped CBP phosphor was studied through the recorded PL profile at numerous temperatures. Fig.6.08. demonstrated the PL spectra for CBP: *x*Er^{3+} (*x* = 7.0 mol%) under $\boldsymbol{\lambda_{ex}}$= 376 nm with the upsurge in the temperature range from 300 K to 473 K.

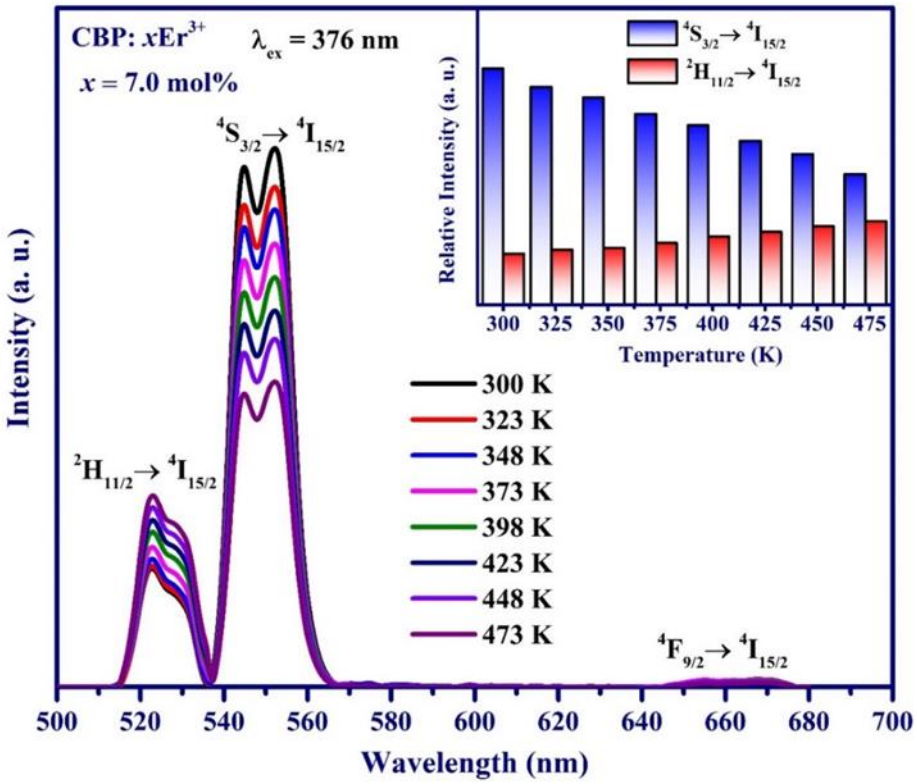

Fig. 6.08: *Emission intensity variation with temperature for CBP:xEr^{3+} (x = 7.0 mol%) under λ_{ex} = 376 nm. The inset reveals the relative emission intensity variation of $^4S_{3/2}\rightarrow{}^4I_{15/2}$ and $^2H_{11/2}\rightarrow{}^4I_{15/2}$ transition with rise in temperature from 300 to 473 K.*

The emission intensity of all peaks was contingent on the temperature and the peak intensity corresponding to the transitions $^2H_{11/2}\rightarrow{}^4I_{15/2}$, $^4S_{3/2}\rightarrow{}^4I_{15/2}$ and $^4F_{9/2}\rightarrow{}^4I_{15/2}$ varies with increase in temperature. The $^2H_{11/2}\rightarrow{}^4I_{15/2}$ transition peak's intensity enhances with the upsurge in temperature. At the same time, the intensity of $^4S_{3/2}\rightarrow{}^4I_{15/2}$ and $^4F_{9/2}\rightarrow{}^4I_{15/2}$ transitions decline with temperature. The intensity improvement in $^2H_{11/2}\rightarrow{}^4I_{15/2}$ transition was due to the $^2H_{11/2}$ level thermally populated from the $^4S_{3/2}$ level via external temperature. This type of variation in PL profiles were arises due to the thermally coupled and very less energy variation (200-2000 cm^{-1}) between the $^4S_{3/2}$ and $^2H_{11/2}$ levels of Er^{3+} ions [228]. The inset bar

diagram shows the change in $^2H_{11/2} \rightarrow {}^4I_{15/2}$ and $^4S_{3/2} \rightarrow {}^4I_{15/2}$ transition peak intensity with the upsurge in temperature, which also affects the emission intensity ratio. The emission intensity ratio between $^2H_{11/2} \rightarrow {}^4I_{15/2}$ and $^4S_{3/2} \rightarrow {}^4I_{15/2}$ transition increases with an increase in temperature from 300 to 473 K. The (ΔE) activation energy is one of the crucial parameters for the phosphor, which was reckoned using the Arrhenius equation as presented in equation number (2.08) in section 2.3.8 of chapter 2 [132]**.** As per the Arrhenius equation, the activation energy ΔE was assessed on the basis of linear fitted slope among *ln((I$_o$/I$_T$)-1)* and *1/K$_B$T*. The plotted Fig. 6.09 discloses the slope value, which was observed to be 0.193. So, the activation energy was found to be 0.193 eV for CBP: *x*Er^{3+} (*x* = 7.0 mol%) phosphor[121,133,134]. Hence, the effect of temperature on PL properties of the optimized phosphor shows that the phosphor has good thermal stability.

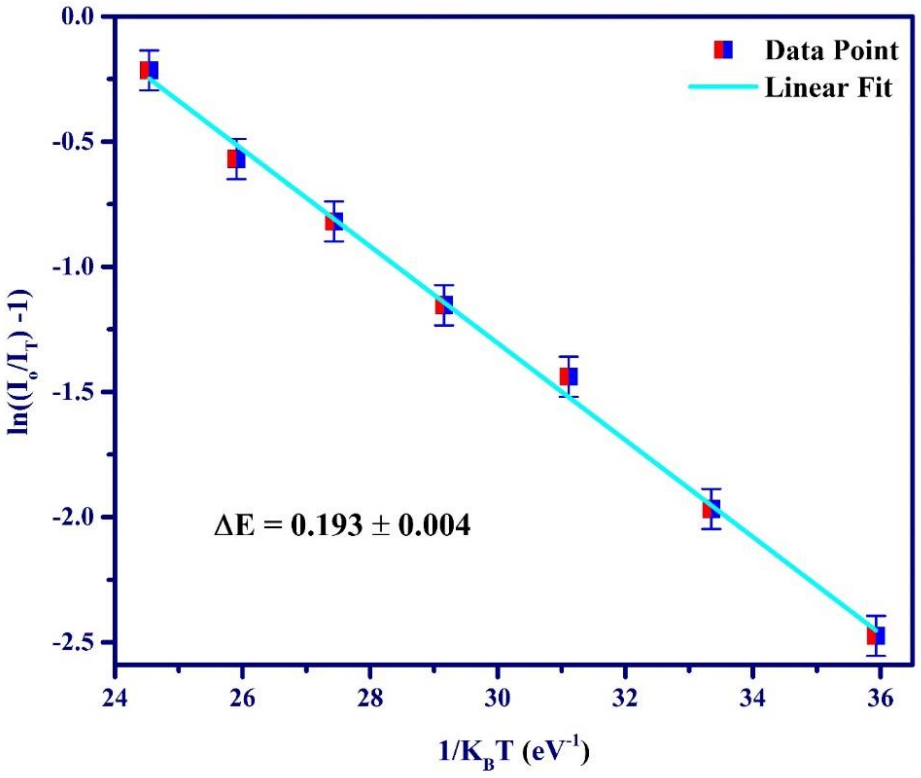

Fig. 6.09: *Plot between* $In[(I_0/I_T)\text{-}1]$ *versus* $1/K_BT$.

6.3.7. Effect of Temperature on CIE Coordinates Analysis

The CIE coordinates for CBP: $x\text{Er}^{3+}$ (x= 7 mol%) phosphor was calculated based on the recorded emission profile. The CIE coordinates are (0.283, 0.703) for CBP: $x\text{Er}^{3+}$ phosphor at an excitation wavelength of 376 nm, as demonstrated in Fig. 6.11. The CIE coordinates were situated in the green region. Hence, the green emission was obtained from CBP: $x\text{Er}^{3+}$ phosphor, making it an appropriate applicant for a green emitting component in photonic devices.

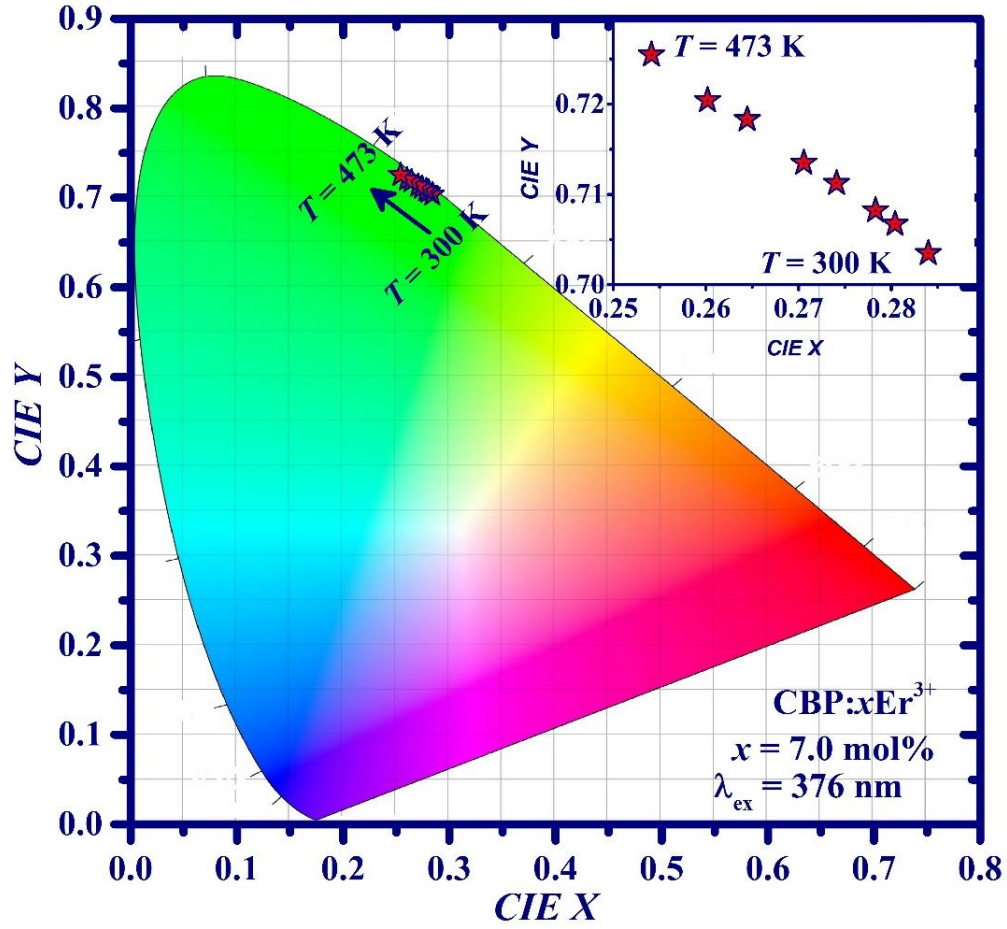

Fig. 6.10: *CIE coordinates values of CBP:$x\text{Er}^{3+}$ (x = 7.0 mol%) phosphor at different temperatures. Inset plot shows the variation of CIE coordinates with upsurge in temperature from 300 to 473 K.*

The emission profile of CBR:xEr^{3+} phosphor under 376 nm excitation was changed with the surge in temperature. Based on variation in emission spectra, the CIE color coordinates were tuned as presented in Fig. 6.10. CIE color coordinates of CBP: xEr^{3+} (x = 7.0 mol%) phosphors at different temperatures under λ_{ex} = 376 nm were listed in Table 6.02. The inset of Fig.6.10 depicts the variation in CIE coordinates from yellowish green to green with an increase in temperature in CBR:xEr^{3+} phosphors.

Table 6.2: CIE color coordinates of CBP: xEr^{3+} (x = 7.0 mol%) phosphors at different temperatures under λ_{ex} = 376 nm.

Temperature (K)	CIE color coordinates (*CIE x*, *CIE y*)
300	(0.284, 0.703)
323	(0.280, 0.706)
348	(0.278, 0.708)
373	(0.274, 0.711)
398	(0.270, 0.713)
423	(0.264, 0.718)
448	(0.261, 0.721)
473	(0.254, 0.725)

The color purity must be very high value for monochromatic emission. So, the color purity for CBR:xEr^{3+} phosphors were found out via using formula as [147]:

$$Color\ Purity = \sqrt{\frac{(x-x_{ee})^2+(y-y_{ee})^2}{(x_d-x_{ee})^2+(y_d-y_{ee})^2}} \quad (6.03)$$

here (x, y) signifies the CIE coordinates of phosphor under 376 nm excitation, (x_{ee}, y_{ee}) represent the standard white color CIE coordinates and (x_d, y_d) signifies the CIE coordinates for the foremost wavelength point. The color purity for optimized CBP:xEr^{3+} (x= 7 mol%)

phosphor's was found to be 97 %. The acquired color purity is very high for all prepared phosphors, which can be employed in photonic devices as an n-UV pumped green constituent.

6.3.8. Temperature Sensing Performance

FIR between the transitions from $^2H_{11/2}$ and $^4S_{3/2}$ levels to the $^4I_{15/2}$ of Er^{3+} ions doped CBP phosphor was primarily governed by the temperature, which can be used for the optical thermometry applications. Based on the PL variation by rising temperature from 300 to 473 K under 376 nm excitation, the atoms situated at $^4S_{3/2}$ level will be excited and move to higher energy at $^2H_{11/2}$ level, result in the FIR value changes. The FIR for the thermally coupled levels of Er^{3+} ion was defined using the Boltzmann distribution theory as follows [228,232]:

$$FIR = \frac{I_{523}}{I_{552}} = A exp\left(-\frac{\Delta E_{TCEL}}{k_B T}\right) \quad (6.04)$$

where I_{523} and I_{552} stand for the integrated PL intensity for $^2H_{11/2} \rightarrow {}^4I_{15/2}$ and $^4S_{3/2} \rightarrow {}^4I_{15/2}$ transitions of Er^{3+} ions, respectively. k_B denotes Boltzmann constant. A represents the pre-exponential and offset factors, respectively. The energy gap between thermally coupled levels and absolute temperature indicated by ΔE_{TCEL} and T, respectively. Based on TDPL spectra the $FIR\left(\frac{I_{523}}{I_{552}}\right)$ were estimated at different temperatures. As per the equation, a graph plotted between $\ln\left[FIR\left(\frac{I_{523}}{I_{552}}\right)\right]$ and the inverse of absolute temperature and fitted with the linear equation as shown in Fig. 6.11. As per the linear fitting, the data points give the slope value 1081.47. The energy gap between thermally coupled levels can be estimated by using the slope and k_B value, which was found to be 733.78 cm^{-1}. The estimated ΔE_{TCEL} values were nearly correlated to the energy population procedure in Er^{3+} ions [222].

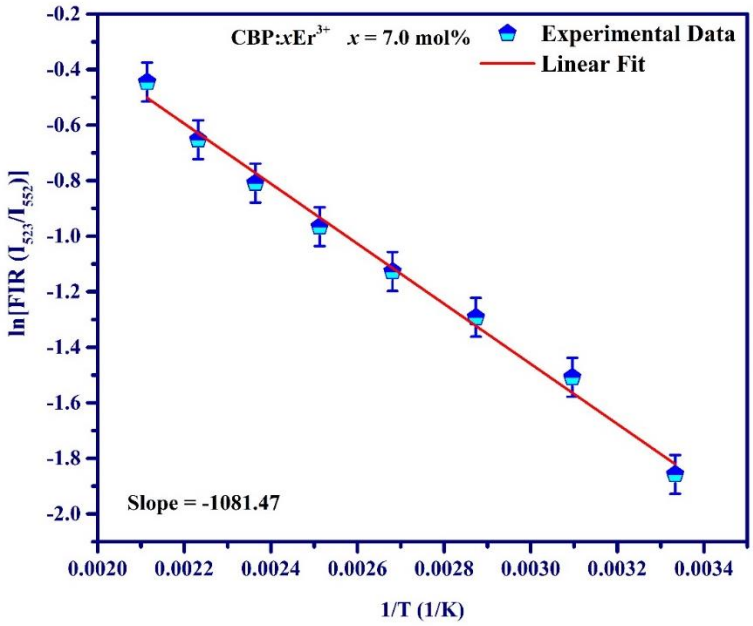

Fig. 6.11: *Plot of ln[FIR* $(\boldsymbol{I_{523}/I_{552}})$*] versus inverse of absolute temperature.*

One of the essential parameters is temperature sensitivity for practical applicability of the prepared phosphor to use in optical thermometry application. Hence, the absolute sensitivity S_a as well as the relative sensitivity S_r were calculated using the following expression [225,233]:

$$S_a = \frac{dFIR}{dT} = FIR * \frac{\Delta E_{TCEL}}{k_B T^2} \tag{6.05}$$

$$S_r = \frac{1}{FIR}\left(\frac{dFIR}{dT}\right) = \frac{\Delta E_{TCEL}}{k_B T^2} \tag{6.06}$$

The calculated value of S_a and S_r were depending on the absolute temperature. Hence, the variation in absolute as well as relative sensitivity with $T\ (K)$ were plotted and presented in Fig. 6.12. The plot reveals that the S_a value enhanced with temperature, while S_r value reduces with surge in temperature from 300 to 473 K. The observed maximum S_a was found to be 0.312 $\%K^{-1}$ at 473 K, whereas the maximum S_r was found to be 1.21 $\%\,K^{-1}$ at 300 K. Table 3 represent the comparison of maximum relative sensitivities of various prepared phosphor materials used

for optical thermometry [222, 228, 234–241]. The result shows that the optimized CBP: xEr^{3+} (x = 7.0 mol%) phosphor can be used as optical thermometry with a high sensitivity in comparison with the other phosphor materials reported.

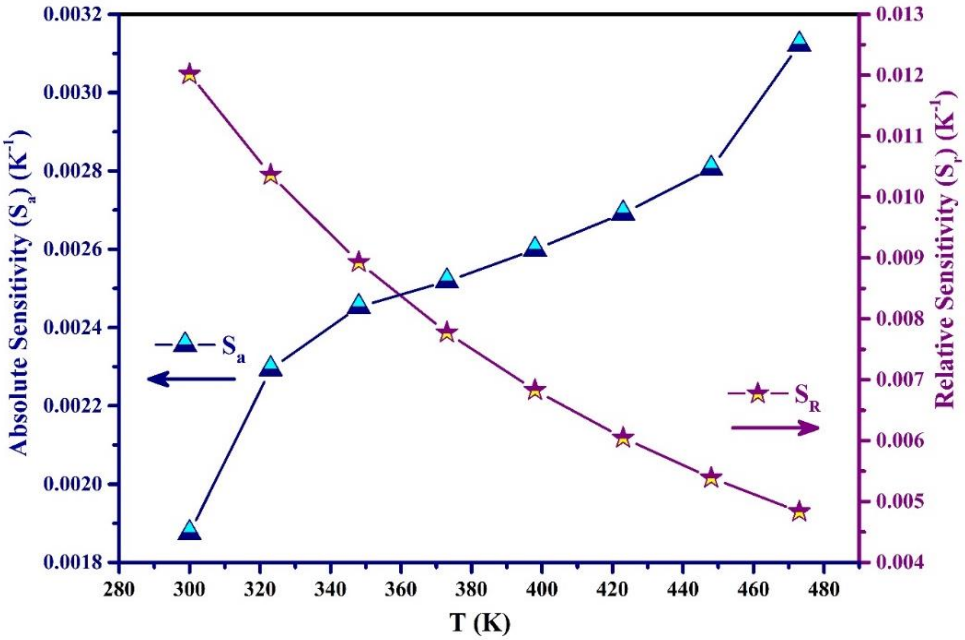

Fig. 6.12: *Variation of absolute sensitivity and relative sensitivity of CBP:xEr^{3+} (x = 7.0 mol%) phosphor with surge in temperature from 300 to 473 K.*

Table 6.3: Comparison of optical thermometry parameters and relative sensitivity (S_r) of phosphors on the basis of FIR technique.

Phosphors	Temperature range (K)	S_r (% K^{-1})	Reference
$Ba_2TiGe_2O_8$: Er^{3+}, Yb^{3+}	333-573	0.59	[222]
$SrSnO_3$: Er^{3+}	294-372	0.99	[228]
$NaBiF_4$: Yb^{3+}, Er^{3+}	303–523	1.07	[234]
$La_2Ti_2O_7$: Er^{3+}, Yb^{3+}	300-553	0.63	[235]
La_2O_3: Er^{3+}, Yb^{3+}	303–600	0.91	[236]
$Ca_2YZr_2Al_2O_{12}$: Bi^{3+}, Sm^{3+}	298-473	0.36	[237]
SrY_2O_4: Bi^{3+}, Eu^{3+}	313-563	0.86	[238]

CBP: Er^{3+}	300-473	1.21	This work
Na_2CaSiO_4:Er^{3+}	300-473	1.88	[239]
$NaYF_4$: Er^{3+}	113-443	2.96	[240]
$Li_4SrCa(SiO_4)_2$: Eu^{2+}	300-500	1.51	[241]

6.4. Conclusions

$Ca_3Bi(PO_4)_3$:Er^{3+} phosphors were successfully prepared by employing the chemical co-precipitation route. XRD patterns confirmed that the prepared $Ca_3Bi(PO_4)_3$:Er^{3+} crystallize in a cubic structure with space group of $I\bar{4}3d$ (220). The CBP: *x*Er^{3+} shows the various peaks in n-UV, visible and near-infrared regions owing to characteristic transitions from $^4I_{15/2}$ level to various higher energy levels. The direct optical bandgap was found to be 4.32 eV for CBP: *x*Er^{3+} (*x* = 1.0 mol%) sample. EDS and elemental mapping data confirm the presence and uniform distribution of compositional elements and doping ions in the prepared samples. The PL study specifies that the phosphor can be effectively excited by n-UV radiation and gives the visible emission at 523 ($^2H_{11/2}\rightarrow$ $^4I_{15/2}$), 552 ($^4S_{3/2}\rightarrow$ $^4I_{15/2}$) and 662 nm ($^4F_{9/2}\rightarrow$ $^4I_{15/2}$) corresponding to the transitions of Er^{3+} ions. The emission intensity varies with the content of Er^{3+} ions and optimum intensity has been observed for 7.0 mol% of Er^{3+} ions in the CBP host lattice. The calculated color coordinates were situated in the green region in the CIE diagram with a high percentage of color purity. The bi-exponential fitted lifetime decay curve was observed for the optimized phosphor with an average decay time of 70 μs. TDPL spectra show the dependency of emission intensity with temperature and dissimilar PL variation from thermally coupled from $^4S_{3/2}$ and $^2H_{11/2}$ levels of Er^{3+} ions. FIR of CBP: *x*Er^{3+} emission between the thermally coupled energy levels was utilized for optical thermometric applications and found the high value of relative sensitivity for the optimized phosphor. Hence, the above-

mentioned characteristics of the synthesized CBP: $x\mathrm{Er}^{3+}$ phosphors will find fascinating applications in optical thermometry and other optoelectronic devices.

CHAPTER 7

Summary and Future Scope of the Research Work

The detailed outcomes and future scope of the research are presented in this chapter. The overall outcomes of the present thesis are focused on the preparation of versatile thermally stable RE activated calcium bismuth phosphate phosphors with enhanced multi-color emitting n-UV/blue pumped luminescent materials for advanced optoelectronic device applications. The as prepared RE activated phosphors exhibit PL characteristics in spectral range pre-requisite for w-LEDs, solar cell, and optical temperature sensors. Important findings of the current research work are also discussed in the current chapter.

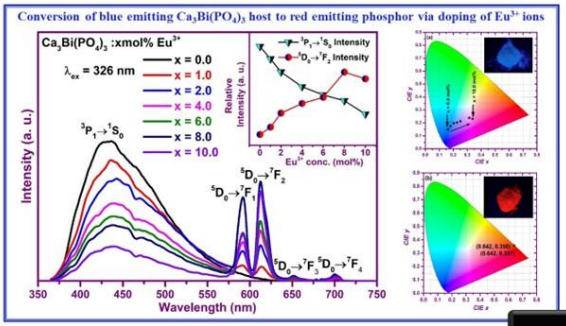

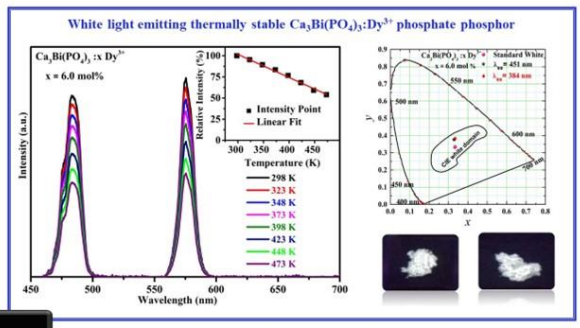

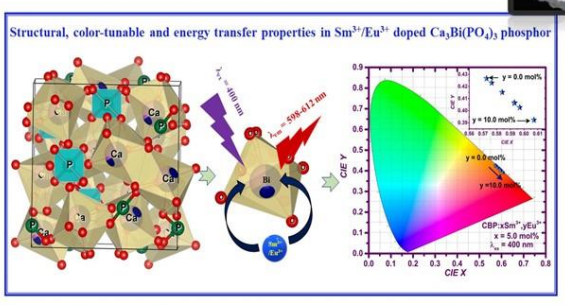

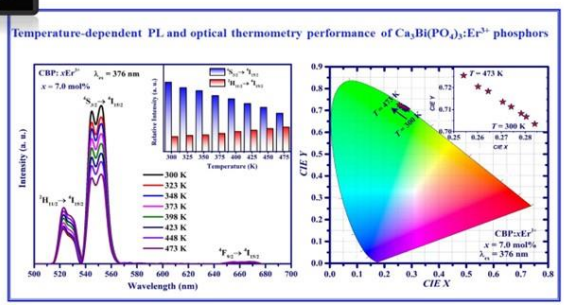

7.1. Summary of the work

The current research work is profoundly focused on the synthesis of strategic luminescent materials, their morphology/microstructural characterizations, color tunable, enhancement of luminescent properties of phosphor-based devices and their optoelectronic applications. Phosphors have emerged as an alternative to conventional energy sources. They offer to save huge amounts of electrical energy and reduce carbon emissions globally [8,9]. Furthermore, phosphors have been found in an extensive range of applications in our daily life, including SSL, advanced optical displays, optical waveguides, solar cells and many more [10-12]. Therefore, the mentioned objectives of the present proposal are to produce the most efficient phosphor with improved luminescent properties by scaling up the process for comfortable industrial acclimatization. The outcome of the research work for achieving the research objectives has been systematized into several chapters. These chapters include the preparation of pure and tunable color (blue, green, red, white light) emitting thermally stable $Ca_3Bi(PO_4)_3$ phosphors activated (Er^{3+}, Eu^{3+}, Eu^{3+}/Sm^{3+} and Dy^{3+} ions) via employing SSR and co-precipitation routes. The requirement for a thermally stable, persistent, effective, eco-friendly phosphor for optoelectronic devices is astounding, as illustrated in the introduction and motivation of the current research work. The as synthesized phosphor in the current research can meet the requirements with increased luminous properties and thermal stability, and it has found numerous utilization possibilities in optical sensors, artificial lighting, display devices, solar cells, security, etc.

The prepared eulytite type $Ca_3Bi(PO_4)_3$ host gives the emission in the blue region and the emission profile is tuned with an increase in the doping concentration of Eu^{3+} ions via energy transfer. The CIE coordinates of undoped $Ca_3Bi(PO_4)_3$ were lie in the blue region, which can modified by doping of Eu^{3+} ions under 326 nm excitation wavelength. The CIE coordinates for

the optimized phosphor under 393 nm excitation were falling in the red region and having color purity of 99.03%. The PL decay curves were bi-exponential for the optimized phosphor with an average decay time of 1.598 ms. The temperature impact over the PL properties indicates that the intensity persists to 75.45% at 200 °C that of at RT, which confirm the excellent thermal stability of phosphor. Thermally stable, crystalline, cubic structured Eu^{3+} activated $Ca_3Bi(PO_4)_3$ phosphors give emission in blue to red tunable color under numerous excitation. This excitation profile was effectively matched with n-UV/blue emitting LED chips for the preparation of artificial solid-state lighting and overcome shortcomings in the commercially used pc-w-LEDs. The as synthesized phosphor can successfully serve as a red emitting component when paired with commercial YAG: Ce^{3+} phosphor and coated over an LED chip to create artificial lighting with a high CRI and a low CCT value. The outcomes recommend, that the color tunable, red emitting and n-UV/blue pumped Eu^{3+} activated $Ca_3Bi(PO_4)_3$ phosphor can act as a potential candidate for the direct utility in pc-WLEDs and other photonic devices.

Single phase white light emitting Dy^{3+} doped $Ca_3Bi(PO_4)_3$ phosphors have been successfully synthesized by co-precipitation method. The Dy^{3+} doped $Ca_3Bi(PO_4)_3$ phosphor exhibit blue, yellow and red peaks under the effectively excited of n-UV and blue LED chips. The combination of blue, yellow and red emission peaks of the as prepared phosphor gives the white light with good thermal stability. The combination of the above mentioned results suggest the potential utility of the synthesized phosphors for the applications in WLEDs under the excitation of n-UV/blue LED chips.

The tunable orange to red-emitting CBP:Sm^{3+}, Eu^{3+} phosphors have been efficiently synthesized by employing co-precipitation technique. The PL quantum yield for CBP:Sm^{3+}, Eu^{3+} phosphor was found to be 86.65 %, which is higher than the commercial phosphors, demonstrating that the as prepared phosphor can be a probable red-emitting constituent in

photonic devices. The emission profile with varying temperature, signifies excellent thermal stability of the as synthesized CBP:Sm^{3+}, Eu^{3+} phosphor. The thermally stable with high quantum yield and optimum PL results indicate that CBP phosphors will be beneficial for a variety of exciting applications in the advanced screens, inorganic LEDs, solar cells, and other photonic devices.

The CBP: $x Er^{3+}$ shows the various peaks in n-UV, visible and near-infrared regions. The PL study specifies that the phosphor can be effectively excited by n-UV radiation and gives the visible green emission with high percentage of color purity. TDPL spectra show the dependency of emission intensity with temperature and dissimilar PL variation from thermally coupled from $^4S_{3/2}$ and $^2H_{11/2}$ levels of Er^{3+} ions. FIR of CBP: $x Er^{3+}$ emission between the thermally coupled energy levels was utilized for optical thermometric applications and found the high value of relative sensitivity for the optimized phosphor. This means the aforementioned Characteristics of the synthesized CBP: xEr^{3+} phosphors will find fascinating applications in optical thermometry and other optoelectronic devices.

7.2. Important Findings of Research Work

Research usually initiates with self-motivation and recognition of a contemporary problem and then followed by strategies to perform and execute the methodology for resolving it. The motivation, outline of the problem, literature survey and origin of research objectives for the development of efficient phosphors for diversified applications in optoelectronic devices. It includes the basics of photoluminescence and comprehensive studies about crystalline luminescent materials and their constituents. Furthermore, the role of phosphor in the advancement of smart optoelectronic devices and the importance of selected host material [$Ca_3Bi(PO_4)_3$] lattice have been discussed. Finally, every step to accomplish the research work,

such as the selection of the activator and sensitizer and optimization of emission and thermal stability for direct utility in a variety of optoelectronic devices such as lighting, solar cell and optical sensors have been investigated in detail.

Moving ahead to the prepared RE doped CBP phosphors and the key aspects/important findings of the present thesis are summed up as follows:

- The eulytite type $Ca_3Bi(PO_4)_3$ host lattice exhibit a broad broad blue host emission at 434 nm under 326 nm excitation wavelength. The host blue emission intensity reduces and the activator peaks intensity enhanced with an increase in doping concentration of Eu^{3+} ions in $Ca_3Bi(PO_4)_3$ phosphor, which indicates the energy transfer from host to activator (Eu^{3+}) ions under λ_{ex}= 326 nm. Also, Eu^{3+} activated $Ca_3Bi(PO_4)_3$ phosphor exhibit intense red emission under the n-UV and blue excitations. The resultant, color tunable and thermally stable blue/red emitting Eu^{3+} activated $Ca_3Bi(PO_4)_3$ phosphor can function as a possible contender for the applications in pc-w-LEDs and other luminous devices.
- Crystalline Dy^{3+} doped $Ca_3Bi(PO_4)_3$ phosphor could be effectively excited by n-UV and blue LED chips, which gives the white emission via combination of blue and yellow peaks. The optimized phosphor's CIE chromaticity coordinates were (0.329, 0.377), which are within the white light region. At 373 K, the emission intensity is still 83.41% of what it is at ambient temperature, which shows good thermal stability. The combination of the aforementioned outcomes leads to the probable applicability of the Dy^{3+} doped $Ca_3Bi(PO_4)_3$ phosphors for use in WLED applications excited by n-UV/blue LED chips.
- The CBP:Sm^{3+} phosphor is properly pumped by the near-UV and blue radiation and emit in the orange region. The expansion of the phosphors absorption profile and an increase

in the emission intensity was accomplished by co-doping CBP:Sm^{3+}, Eu^{3+} phosphor with 86.65 % PL quantum yield. All these outcomes illustrate that the as prepared phosphor can be a probable red-emitting constituent in inorganic whilte LEDs, solar cells and other photonic devices.

- One of the prime applications of photonic devices is to sense real-time temperature with high accuracy. With this objective, the CBP: *x*Er^{3+} phosphor was prepared, which is effectively excited by n-UV radiation and gives the visible emission at 523 ($^2H_{11/2}\rightarrow {}^4I_{15/2}$), 552 ($^4S_{3/2}\rightarrow {}^4I_{15/2}$) and 662 nm ($^4F_{9/2}\rightarrow {}^4I_{15/2}$) corresponding to transitions of Er^{3+} ions. The CIE coordinates were situated in the green region with a high percentage of color purity. TDPL spectra show the dependency of emission intensity with temperature and dissimilar PL variation from thermally coupled from $^4S_{3/2}$ and $^2H_{11/2}$ levels of Er^{3+} ions. FIR of CBP: *x*Er^{3+} emission between the thermally coupled energy levels were used for optical thermometric applications, and it was shown that the optimized phosphor had an excellent relative sensitivity value, which has fascinating applications in optical thermometry and other optoelectronic devices.

The aforementioned results confirm that RE doped $Ca_3Bi(PO_4)_3$ thermally stable, highly efficient phosphors developed in this thesis could be useful for optoelectronic device applications, especially in w-LEDs, photovoltaics and optical sensors.

7.3. Future Scope

- To explore other synthesis methods to improve the particle morphology, reduce the particle size to nano which in turn further improves the luminescence properties.
- To boost the luminescence properties for RE doped $Ca_3Bi(PO_4)_3$ phosphor via suitable co-dopant and surfactant.

- To enhance and optimize emission intensity using up and down conversion phosphors for photonic applications.
- Finally, to fabricate a prototype and assessment of the luminous efficacy, and other properties of phosphor based optoelectronic devices.
- To extend the utility of this phosphor for applications in bio-imaging, pressure sensing and security ink.

References:

[1] R. Baños, F. Manzano-Agugliaro, F.G. Montoya, C. Gil, A. Alcayde, J. Gómez, Renewable and Sustainable Energy Rev. 15 (2011) 1753–1766.

[2] P. Kumar, Kanika, S. Singh, R. Lahon, A. Gundimeda, G. Gupta, B.K. Gupta, J. Lumin. 196 (2018) 207–213.

[3] S. Ye, F. Xiao, Y.X. Pan, Y.Y. Ma, Q.Y. Zhang, Mater. Sci. Eng. R Rep. 71 (2010) 1–34.

[4] P. Moodley, C. Trois, Sustainable Biofuels: Opportunities and Challenges (2021) 21–42.

[5] W. Abrahamse, L. Steg, C. Vlek, T. Rothengatter, J. Environ. Psychol. 25 (2005) 273–291.

[6] H. Allcott, S. Mullainathan, Science (1979) 327 (2010) 1204–1205.

[7] M. Sharif Hossain, Energy Policy 39 (2011) 6991–6999.

[8] D. Van der Voort, J.M.E. de Ruk, G. Blasse, Phys. Stat. Sol. A 135 (1993) 621–626

[9] A. Ożadowicz, J. Grela, Energy Effic. 10 (2017) 563–576.

[10] J. McKittrick, L.E. Shea-Rohwer, J. Am. Ceram. Soc. 97 (2014) 1327–1352.

[11] S. Ye, F. Xiao, Y.X. Pan, Y.Y. Ma, Q.Y. Zhang, Mater. Sci. Eng. R Rep. 71 (2010) 1–34.

[12] E.F. Schubert, J.K. Kim, Science (1979) 308 (2005) 1274–1278.

[13] R.B. Basavaraj, H. Nagabhushana, B.D. Prasad, S.C. Sharma, S.C. Prashantha, B.M. Nagabhushana, Optik (Stuttg.) 126 (2015) 1745–1756.

[14] S. Kaur, M. Jayasimhadri, A.S. Rao, J. Alloys Compd. 697 (2017) 367–373.

[15] V.B. Pawade, H.C. Swart, S.J. Dhoble, Renew. Sustain. Energy Rev. 52 (2015) 596–612.

[16] H. Yang, G. Zhu, L. Yuan, C. Zhang, F. Li, H. Xu, A. Yu, J. Am. Ceram. Soc. 51 (2012) 49–51.

[17] H.K. Yang, J.H. Jeong, Society 12 (2010) 226–230.

[18] K. Jha, M. Jayasimhadri, J. Alloys Compd. 688 (2016) 833–840.

[19] G. Blasse, A. Bril, Appl. Phys. Lett. 11 (1967) 53–55.

[20] X. Li, J.D. Budai, F. Liu, J.Y. Howe, J. Zhang, X.-J. Wang, Z. Gu, C. Sun, R.S. Meltzer, Z. Pan, Light Sci. Appl. 2 (2013) e50.

[21] L. Wang, R.-J. Xie, Y. Li, X. Wang, C.-G. Ma, D. Luo, T. Takeda, Y.-T. Tsai, R.-S. Liu, N. Hirosaki, Light Sci. Appl. 5 (2016) e16155.

[22] L. Mishra, A. Sharma, A.K. Vishwakarma, K. Jha, M. Jayasimhadri, B. v. Ratnam, K. Jang, A.S. Rao, R.K. Sinha, J. Lumin. 169 (2016) 121–127.

[23] P. Suthanthirakumar, K. Marimuthu, J. Mol. Struct. 1125 (2016) 443–452.

[24] K. Vivekanandan, S. Selvasekarapandian, P. Kolandaivel, M.T. Sebastian, S. Suma, Mater. Chem. Phys. 49 (1997) 204–210.

[25] Y.S. Tang, S.F. Hu, C.C. Lin, N.C. Bagkar, R.S. Liu, Appl. Phys. Lett. 90 (2007) 151108–3.

[26] S. Choi, Y.J. Yun, S.J. Kim, H.K. Jung, Opt. Lett. 38 (2013) 1346–1348.

[27] J. L. Cia, R. Y. Yi, C. J. Zhao, S. T. Tie, J. Y. Shen, Mater. Res. Bull. 57 (2014) 85–90.

[28] M. Shang, C. Li, J. Lin, Chem. Soc. Rev. 43 (2014) 1372–86.

[29] K. Yoshikawa, H. Kawasaki, W. Yoshida, T. Irie, K. Konishi, K. Nakano, T. Uto, D. Adachi, M. Kanematsu, H. Uzu, K. Yamamoto, Nat. Energy. 2 (2017) 17032.

[30] K. Li, R. van Deun, ACS Sustain Chem. Eng. 7 (2019) 16284–16294.

[31] H. Ahmed, J. Doran, S.J. McCormack, Solar Energy. 126 (2016) 146–155.

[32] G. Griffini, F. Bella, F. Nisic, C. Dragonetti, D. Roberto, M. Levi, R. Bongiovanni, S. Turri, Adv. Energy Mater. 5 (2015) 1–9.

[33] F. Bella, G. Griffini, M. Gerosa, S. Turri, R. Bongiovanni, J. Power Sources 283 (2015) 195–203.

[34] J.A. Luceño-Sánchez, A.M. Díez-Pascual, R.P. Capilla, Int. J. Mol. Sci. 20 (2019) 976.

[35] X. Li, J.D. Budai, F. Liu, J.Y. Howe, J. Zhang, X. Wang, Z. Gu, C. Sun, R.S. Meltzer, Z. Pan, Light Sci. Appl. 2 (2013) e50.

[36] Y. Gao, S. Murai, K. Shinozaki, J. Qiu, K. Tanaka, ACS Appl. Electron. Mater. 1 (2019) 961–971.

[37] Z. Xia, Y. Zhang, M. S. Molokeev, V. V. Atuchin, J. Phys. Chem. C 117 (2013) 20847–20854.

[38] F. Kang, Y. Zhang, M. Peng, Inorg. Chem. 54 (2015) 1462–1473.

[39] G. Zhu, Z. Ci, Y. Shi, M. Que, Q. Wang, Y. Wang, J. Mater. Chem. C 1 (2013) 5960–5969.

[40] V.R. Bandi, B.K. Grandhea, K. Jang, D.-S. Shin, S.-S. Yi, J.-H. Jeong, Mater. Chem. Phys. 140 (2013) 453–457.

[41] Y. Gao, B. Wang, L. Liu, K. Shinozaki, J. Lumin. 238 (2021) 118235.

[42] Y. Gao, J. Qiu, D. Zhou, J. Am. Ceram. Soc. 100 (2017) 2901–2913.

[43] B. Valeur, M. Ario, N. Berberan-Santos, J. Chem. Educ 88 (2011) 731–738.

[44] C.R. Ronda, Luminescence - From Theory to Applications, Wiley-VCH, India, 2007.

[45] A. Kitai, Luminescent Materials and Applications, John Wiley & Sons Ltd, England, 2008.

[46] K.N. Shinde, S.J. Dhoble, H.C. Swart, K. Park, Phosphate Phosphors for Solid-State Lighting, Springer Series in Materials Science, vol 174. Springer, Berlin, Heidelberg. (2012).

[47] L.U. Khan, Z.U. Khan, Handbook of Materials Characterization (2018) 345–404.

[48] N. Deopa, A.S. Rao, J. Lumin. 192 (2017) 832–841.

[49] K. Jha, A.K. Vishwakarma, M. Jayasimhadri, D. Haranath, J. Alloys Compd. 719 (2017) 116–124.

[50] G. Blasse, B.C. Grabmaier, Luminescent Materials, Springer-Verlag, Germany, 1994.

[51] S. Gai, C. Li, P. Yang, J. Lin, Chem. Rev. 114 (2014) 2343–2389.

[52] W.T. Carnall, P.R. Fields, K. Rajnak, J. Chem. Phys. 49 (2003) 4447.

[53] A. Bednarkiewicz, K. Trejgis, J. Drabik, A. Kowalczyk, L. Marciniak, ACS Appl. Mater. Interfaces 9 (2017) 43081–43089.

[54] W.T. Carnall, P.R. Fields, K. Rajnak, J. Chem. Phys. 49 (2003) 4424.

[55] W. M. Yen, S. Shionoya, H. Yamamoto, Fundamentals of Phosphors,1st ed. CRC Press, Boca Raton, 2007.

[56] M.K. Sahu, M. Jayasimhadri, K. Jha, B. Sivaiah, A.S. Rao, D. Haranath, J. Lumin. 202 (2018) 475–483.

[57] B. v Ratnam, M.K. Sahu, A.K. Vishwakarma, K. Jha, H.J. Woo, K. Jang, M. Jayasimhadri, J. Lumin. 185 (2017) 99–105.

[58] J.G. Sole, L.E. Bausa, D. Jaque, An Introduction to the Optical Spectroscopy of Inorganic Solids, John Wiley & Sons Ltd, England, 2005.

[59] W.M. Yen, S. Shionoya, H. Yamamoto, Phosphor Handbook, 2nd ed., CRC Press Taylor & Francis Group, New York, 2003

[60] A. Kitai, Luminescent Materials and Applications, John Wiley & Sons Ltd, England, 2008.

[61] X. Chen, P. Dai, X. Zhang, C. Li, S. Lu, X. Wang, Y. Jia, Y. Liu, Inorg. Chem. 53 (2014) 3441–3448.

[62] Z. Zhang, W. Tang, J. Lumin. 169 (2016) 367–373.

[63] G. Blasse, Philips Res. Rep. 24 (1969) 131–144.

[64] D.L. Dexter, J.H. Schulman, J. Chem. Phys. 22 (1954) 1063–1070.

[65] L.G. van Uitert, J. Electrochem. Soc. 114 (1967) 1048–1053.

[66] Y. Tian, B. Chen, B. Tian, R. Hua, J. Sun, L. Cheng, H. Zhong, X. Li, J. Zhang, Y. Zheng, T. Yu, L. Huang, Q. Meng, J. Alloys Compd. 509 (2011) 6096–6101.

[67] B. Tian, B. Chen, Y. Tian, X. Li, J. Zhang, J. Sun, H. Zhong, L. Cheng, S. Fu, H. Zhong, Y. Wang, X. Zhang, H. Xia, R. Hua, J. Mater. Chem. C 1 (2013) 2338–2344.

[68] S. Kaur, A.S. Rao, M. Jayasimhadri, Ceram. Int. 43 (2017) 7401–7407.

[69] A.K. Vishwakarma, K. Jha, M. Jayasimhadri, B. Sivaiah, B. Gahtori, D. Haranath, Dalt. Trans. 44 (2015) 17166–17174.

[70] C.S. McCamy, Color Res. Appl. 17 (1992) 142–144.

[71] C. Strümpel, M. McCann, G. Beaucarne, V. Arkhipov, A. Slaoui, V. Švrček, C. del Cañizo, I. Tobias, Sol. Energy Mater Sol. Cells. 91 (2007) 238–249.

[72] B.M. van der Ende, L. Aarts, A. Meijerink, Phys. Chem. Chem. Phys. 11 (2009) 11081–11095.

[73] S. Liu, J. Cui, J. Jia, J. Fu, W. You, Q. Zeng, Y. Yang, X. Ye, Ceram. Int. 45 (2019) 1–10.

[74] X. Li, J. Cao, Y. Wei, Z. Yang, H. Guo, J. Am. Ceram. Soc. 98 (2015) 3824–3830.

[75] W. Xu, Z. Zhang, W. Cao, Opt. Lett. 37 (2012) 4865.

[76] I.E. Kolesnikov, E. v. Golyeva, M.A. Kurochkin, E. Lähderanta, M.D. Mikhailov, Sens. Actuators B Chem. 235 (2016) 287–293.

[77] J. Cao, X. Li, Z. Wang, Y. Wei, L. Chen, H. Guo, Sens. Actuators B Chem. 224 (2016) 507–513.

[78] A.F. Silva, F. Elan, E.L. Falcão-Filho, L.J.Q. Maia, C.B. de Araújo, J. Mater Chem. C. 5 (2017) 1240–1246.

[79] J.F. Tao, H. Cai, Y.D. Gu, J. Wu, A.Q. Liu, IEEE Photonics Technol. Lett. 27 (2015) 767–769.

[80] H. Zhou, N. An, K. Zhu, J. Qiu, L. Yue, L.G. Wang, L. Ye, J. Lumin. 229 (2021) 117656.

[81] A. Pandey, V.K. Rai, V. Kumar, V. Kumar, H.C. Swart, Sens. Actuators B Chem. 209 (2015) 352–358.

[82] S.S. Shinde, P.S. Shinde, Y.W. Oh, D. Haranath, C.H. Bhosale, K.Y. Rajpure, Appl. Surf. Sci. 258 (2012) 9969–9976.

[83] G.C. Righini, F. Enrichi, L. Zur, M. Ferrari, J. Phys. Conf. Ser. 1221 (2019) 012028.

[84] N. Yao, J. Huang, K. Fu, X. Deng, M. Ding, X. Xu, RSC Adv. 6 (2016) 17546–17559.

[85] X. Huang, S. Han, W. Huang, X. Liu, Chem. Soc. Rev. 42 (2013) 173–201.

[86] M.K. Sahu, J. Mula, J. Am. Ceram. Soc. 102 (2019) 6087–6099.

[87] C.C. Lin, Z.R. Xiao, G.-Y. Guo, T.-S. Chan, R.-S. Liu, J. Am. Chem. Soc. 132 (2010) 3020–3028.

[88] Y.C. Liao, C.H. Lin, S.L. Wang, J. Am. Chem. Soc. 127 (2005) 9986–9987.

[89] C. Qin, Y. Huang, L. Shi, G. Chen, X. Qiao, H.J. Seo, J. Phys. D Appl. Phys. 42 (2009) 185105.

[90] P.P. Sahoo, T.N. Guru Row, Inorg. Chem. 49 (2010) 10013–10021.

[91] X. Zou, L. He, R. Li, Q. Zheng, Y. Liu, C. Xu, D. Lin, J. Mater. Sci.: Mater. Electron. 28 (2017) 2826–2832.

[92] M. Jiao, N. Guo, W. Lü, Y. Jia, W. Lv, Q. Zhao, B. Shao, H. You, Dalt. Trans. 42 (2013) 12395–12402.

[93] Q. Liu, Y. Liu, Y. Ding, Z. Peng, X. Tian, Q. Yu, Ceram. Int. 40 (2014) 10125–10129.

[94] N. Guo, Y. Huang, Y. Jia, W. Lv, Q. Zhao, Z. Xia, H. You, Dalt. Trans. 42 (2013) 941–947.

[95] M. Jayachandiran, S.M.M. Kennedy, J. Alloys Compd. 775 (2019) 353–359.

[96] Y. Guo, S.H. Park, B.C. Choi, J.H. Jeong, J.H. Kim, J. Alloys Compd. 742 (2018) 159–164.

[97] X. Chen, P. Dai, X. Zhang, C. Li, S. Lu, X. Wang, Y. Jia, Y. Liu, Inorg. Chem. 53 (2014) 3441–3448.

[98] D. Yu, Y. Liang, M. Zhang, M. Tong, Q. Wang, J. Zhao, J. Wu, G. Li, C. Yan, J. Mater. Sci.: Mater. Electron. 25 (2014) 3526–3531.

[99] N. Renuka, N. Vijayan, B. Rathi, R.R. Babu, K. Nagarajan, D. Haranath, G. Bhagavannarayana, Optik (Stuttg.) 123 (2011) 4–7.

[100] D. Haranath, P. Sharma, H. Chander, J. Phys. D Appl. Phys. 38 (2005) 371–375.

[101] B.P. Singh, a K. Parchur, R.K. Singh, a a Ansari, P. Singh, S.B. Rai, Phys. Chem. Chem. Phys. 15 (2013) 3480–9.

[102] J.R. Lakowicz, Principles of Fluorescence Spectroscopy, 3rd ed., Springer Science Business Media, LLC, Singapore, 2006.

[103] D. Haranath, N. Gandhi, S. Sahai, M. Husain, V. Shanker, Chem. Phys. Lett. 496 (2010) 100–103.

[104] V. Dubey, R. Tiwari, M. Pradhan, G. Rathore, C. Sharma, R. Tamrakar, Journal of Luminescence and Applications 1 (2014) 30–39.

[105] M.K. Mahata, T. Koppe, T. Mondal, C. Brüsewitz, K. Kumar, V.Kr. Rai, H. Hofsäss, U. Vetter, Phys. Chem. Chem. Phys. 17 (2015) 20429–20430.

[106] G. Li, Y. Tian, Y. Zhao, J. Lin, Chem. Soc. Rev. 44 (2015) 8688–8713.

[107] Y. Chen, J. Wang, M. Gong, Q. Su, J. Solid State Chem. 180 (2007) 1165–1170.

[108] R.K. Tamrakar, D.P. Bisen, N. Bramhe, J. Radiat. Res. Appl. Sci. 7 (2014) 550–559.

[109] P. Godlewska, A. Matraszek, L. Macalik, K. Hermanowicz, M. Ptak, P.E. Tomaszewski, J. Hanuza, I. Szczygieł, J. Alloys Compd. 628 (2015) 199–207.

[110] D. Jugović, D. Uskoković, J. Power Sources. 190 (2009) 538–544.

[111] R.K. Tamrakar, D.P. Bisen, K. Upadhyay, I.P. Sahu, J. Phys. Chem. C 119 (2015) 21072–21086.

[112] N. Jain, N. Marwaha, R. Verma, B.K. Gupta, A.K. Srivastava, RSC Adv. 6 (2016) 4960–4968.

[113] X. Li, T. Odoom-Wubah, Z. Chen, B. Zheng, J. Huang, Ceram. Int. 40 (2014) 16317–16321.

[114] B.D. Cullity, Elements of X-Ray Diffraction. 2nd ed., Addison-Wesley Publishing Company Inc., Phillippines, 1978.

[115] L. Alexander, H.P. Klug, J. Appl. Phys. 21 (1950) 137–142.

[116] A. Khorsand Zak, W.H. Abd. Majid, M.E. Abrishami, R. Yousefi, Solid State Sci. 13 (2011) 251–256.

[117] C.S. Pappas, P.A. Tarantilis, P.C. Harizanis, M.G. Polissiou, Appl. Spectrosc. 57 (2003) 23–27.

[118] B. C. Smith, Fundamentals of Fourier Transform Infrared Spectroscopy, 2nd ed., CRC Press, 2016.

[119] R.E. Hummel, Encyclopedia of Analytical Chemistry John Wiley & Sons, Ltd., 2003.

[120] R. Lopez, R. Gomez, J. Solgel Sci. Technol. 61 (2012) 1–7.

[121] D. Xu, Z. Yang, J. Sun, X. Gao, J. Du, J. Mater. Sci.: Mater. Electron. 27 (2016) 8370–8377.

[122] J. Zhou, Z. Xia, M. Yang, K. Shen, J. Mater Chem. 22 (2012) 21935–21941.

[123] K. Akhtar, S.A. Khan, S.B. Khan, A.M. Asiri, Handbook of Materials Characterization, Springer Nature Switzerland (2018) 113–145.

[124] S.K. Sharma, D.S. Verma, L.U. Khan, S. Kumar, S.B. Khan, Handbook of Materials Characterization (2018) 1–613.

[125] J.-C. G. Bünzli, S. V. Eliseeva Basics of Lanthanide Photophysics, Lanthanide Luminescence, Springer, Berlin, 2010.

[126] S. Shionoya, Photoluminescence, Luminescence of Solids, Springer New York, 1998, 95-133.

[127] K. Wakabayashi, Y. Yamaguchi, T. Sekiya, S. Kurita, J. Lumin. 112 (2005) 50–53.

[128] K. Suhling, D. M. David, D. Phillips, J. Fluoresc.12 (2002) 91-95.

[129] K. Li, X. Liu, Y. Zhang, X. Li, H. Lian, J. Lin, Inorg. Chem. 54 (2015) 323–333.

[130] K. Jha, M. Jayasimhadri, J. Am. Ceram. Soc. (2017) 1402–1411.

[131] J. Sun, X. Zhang, Z. Xia, H. Du, Mater. Res. Bull. 46 (2011) 2179–2182.

[132] R. Bajaj, A.S. Rao, G.V. Prakash, J. Alloys Compd. 885 (2021) 160893.

[133] K. Li, M. Shang, H. Lian, J. Lin, Inorg. Chem. 54 (2015) 7992–8002.

[134] P. Li, M. Peng, X. Yin, Z. Ma, G. Dong, Q. Zhang, J. Qiu, Opt. Express. 21 (2013) 18943–18948.

[135] M.-H. Fang, C. Ni, X. Zhang, Y.-T. Tsai, S. Mahlik, A. Lazarowska, M. Grinberg, H.-S. Sheu, J.-F. Lee, B.-M. Cheng, R.-S. Liu, ACS Appl. Mater. Interfaces. 8 (2016) 30677–30682.

[136] G. Li, D. Geng, M. Shang, C. Peng, Z. Cheng, J. Lin, J. Mater Chem. 21 (2011) 13334–13344.

[137] S. Liang, P. Dang, G. Li, Y. Wei, Y. Wei, H. Lian, J. Lin, Adv Opt. Mater. 2 (2018) 1–11.

[138] S. Liao, X. Ji, Y. Liu, J. Zhang, ACS Appl Mater Interfaces. 10 (2018) 39064–39073.

[139] L.R. Moorthy, T.S. Rao, M. Jayasimhadri, A. Radhapathy, D.V.R. Murthy, Spectrochim. Acta A Mol. 60 (2004) 2449–2458.

[140] X. Huang, H. Guo, B. Li, J. Alloys Compd. 720 (2017) 29–38.

[141] V.R. Bandi, M. Jayasimhadri, J. Jeong, K. Jang, H.S. Lee, S.S. Yi, J.H. Jeong, J. Phys. D Appl. Phys. 43 (2010).

[142] K. Park, D.A. Hakeem, Ceram Int 43 (2017) 4725–4729.

[143] K. Park, D.A. Hakeem, J.W. Pi, G.W. Jung, J Alloys Compd 772 (2019) 1040–1051.

[144] S. Kaur, A.S. Rao, M. Jayasimhadri, B. Sivaiah, D. Haranath, J. Alloys Compd. 802 (2019) 129–138.

[145] D. Chen, W. Xiang, X. Liang, J. Zhong, H. Yu, M. Ding, H. Lu, Z. Ji, J. Eur. Ceram. Soc. 35 (2015) 859–869.

[146] W. Liu, Q. Liu, J. Ni, Z. Zhou, G. Liu, RSC Adv. 8 (2018) 20781–20789.

[147] G. Zhu, Z. Li, C. Wang, X. Wang, F. Zhou, M. Gao, S. Xin, Y. Wang, Dalton. Trans. 48 (2019) 1624–1632.

[148] D. Haranath, S. Mishra, S. Yadav, R.K. Sharma, L.M. Kandpal, N. Vijayan, M.K. Dalai, G. Sehgal, V. Shanker, Appl. Phys. Lett. 101 (2012) 1–6.

[149] S. Zhang, W. Lin, Q. Li, Z. Mu, W. Li, Y. Li, Y. Li, F. Wu, Spectrochim. Acta A Mol. 219 (2019) 110–120.

[150] H.F. Folkerts, J. Zuidema, G. Blasse, Chem. Phys. Lett. 249 (1996) 59–63.

[151] C. H. Arbiba, B. Elouadid, , J. Darrieta, A, Mater. Res. Bull. 35 (2000) 761–773.

[152] H. Guo, X. Huang, Y. Zeng, J. Alloys Compd. 741 (2018) 300–306.

[153] K. Jha, M. Jayasimhadri, D. Haranath, K. Jang, J. Alloys Compd. 789 (2019) 622–629.

[154] Y. Liu, G. Liu, J. Wang, X. Dong, W. Yu, Inorg. Chem. 53 (2014) 11457–11466.

[155] X. Huang, S. Wang, B. Li, Q. Sun, H. Guo, Opt. Lett. 43 (2018) 1307–1310.

[156] A.K. Vishwakarma, K. Jha, M. Jayasimhadri, a. S. Rao, K. Jang, B. Sivaiah, D. Haranath, J. Alloys Compd. 622 (2015) 97–101.

[157] P. Balakrishnan, M. Jayachandiran, S.M.M. Kennedy, J. Lumin. 215 (2019) 116649.

[158] R. Cao, G. Quan, Z. Shi, Z. Luo, Q. Hu, S. Guo, J. Lumin. 181 (2017) 332–336.

[159] Q. Sun, T. Sakthivel, B. Devakumar, S. Wang, L. Sun, J. Liang, S.J. Dhoble, X. Huang, J. Lumin. 222 (2020) 117127.

[160] G. Annadurai, L. Sun, H. Guo, X. Huang, J. Lumin. 226 (2020) 117474.

[161] Q. Wu, Q. Zhao, P. Zheng, W. Chen, D. Xiang, Z. He, Q. Huang, J. Ding, J. Zhou, Ceram. Int. 46 (2020) 2845–2852.

[162] R.J. Xie, N. Hirosaki, N. Kimura, K. Sakuma, M. Mitomo, Appl. Phys. Lett. 90 (2007) 191101.

[163] T. Pulli, T. Dönsberg, T. Poikonen, F. Manoocheri, P. Kärhä, E. Ikonen, Light Sci. Appl. 4 (2015) e332.

[164] J. Chen, Y. Liu, L. Mei, H. Liu, M. Fang, Z. Huang, Sci. Rep. 5 (2015) 9673.

[165] P. Dai, J. Cao, X. Zhang, Y. Liu, J. Phys. Chem. C. 120 (2016) 18713–18720.

[166] S.E. Brinkley, N. Pfaff, K.A. Denault, Z. Zhang, H.T.B. Hintzen, R. Seshadri, S.P. Denbaars, Appl. Phys. Lett. 99 (2011) 241106.

[167] R. Shrivastava, J. Kaur, V. Dubey, J. Fluoresc. 26 (2016) 105–111.

[168] Y. Zhang, W. Gong, J. Yu, H. Pang, Q. Song, G. Ning, RSC Adv. 5 (2015) 62527–62533.

[169] B. V. Ratnam, M. Jayasimhadri, K. Jang, H.S. Lee, J. Am. Ceram. Soc. 93 (2010) 3857–3861.

[170] R.K.D. and S.K.S. S. Som, Subrata Das, S. Dutta, Hendrik G. Visser, Mukesh Kumar Pandey, Pushpendra Kumar, RSC Adv. 5 (2015) 70887–708898.

[171] H. Chander, Mater. Sci. Eng. R Rep. 49 (2005) 113–155.

[172] J. Barbier, J. Solid State Chem. 101 (1992) 249–256.

[173] S. Som, S.K. Sharma, J. Phys. D Appl. Phys. 45 (2012) 415102.

[174] A. Nakrela, N. Benramdane, A. Bouzidi, Z. Kebbab, M. Medles, C. Mathieu, Results Phys. 6 (2016) 133–138.

[175] K. Rawat, P.K. Shishodia, Adv. Powder Technol. 28 (2017) 611-617.

[176] G.K. Williamson, W.H. Hall, Acta Metallurgica. 1 (1953) 22.

[177] B.S. Barros, P.S. Melo, R.H.G.A. Kiminami, A.C.F.M. Costa, G.F. de Sá, S. Alves, J. Mater Sci. 41 (2006) 4744–4748.

[178] S. Fujihara, A. Suzuki, T. Kimura, J. Appl Phys. 94 (2003) 2411–2416.

[179] A.C. Chapman, L.E. Thirlwell, Spectrochim. Acta. 20 (1964) 937–947.

[180] C.M. Julien, A. Mauger, K. Zaghib, R. Veillette, H. Groult, Ionics 18 (2012) 625–633.

[181] Y. Huang, X. Wang, H.S. Lee, E. Cho, K. Jang, Y. Tao, J. Phys. D Appl. Phys. 40 (2007) 7821–7825.

[182] S.L. Reddy, G.S. Reddy, Spectrochim. Acta A Mol. 65 (2006) 1227–1233.

[183] W.T. Carnall, P.R. Fields, K. Rajnak, J. Chem. Phys. 49 (1968) 4424–4442.

[184] P.P. Pawar, S.R. Munishwar, S. Gautam, R.S. Gedam, J. Lumin. 183 (2017) 79–88.

[185] Q. Su, Z. Pei, L. Chi, H. Zhang, Z. Zhang, F. Zou, J. Alloys Compd. 192 (1993) 25–27.

[186] J. S. Kumar, K. Pavani, A. M. Babu, N. K. Giri, S.B. Rai, L.R. Moorthy, J. Lumin. 130 (2010) 1916–1923.

[187] Sanju, Ravina, Anu, A. Kumar, V. Kumar, M. K. Sahu, S. Dahiya, Nisha Deopa, R. Punia d, A.S. Rao, Opt. Mater. 114 (2021) 110937

[188] Z. Yang, D. Xu, J. Sun, Opt. Express 25 (2017) A391–A400.

[189] R.V. Yadav, R.S. Yadav, A. Bahadur, A.K. Singh, S.B. Rai, Inorg. Chem. 55 (2016) 10928–10935.

[190] J. Zheng, H. Mehrvarz, C. Liao, J. Bing, X. Cui, Y. Li, V.R. Goncąles, C.F.J. Lau, D.S. Lee, Y. Li, M. Zhang, J. Kim, Y. Cho, L.G. Caro, S. Tang, C. Chen, S. Huang, A.W.Y. Ho-Baillie, ACS Energy Lett. 4 (2019) 2623–2631.

[191] J. Li, L. Chen, Z. Hao, X. Zhang, L. Zhang, Y. Luo, J. Zhang, Inorg. Chem. 54 (2015) 4806–4810.

[192] A. Mathur, P. Halappa, C. Shivakumara, J. Mater. Sci.: Mater. Electron. 29 (2018) 19951–19964.

[193] C. Zhang, H. Liang, S. Zhang, C. Liu, D. Hou, L. Zhou, G. Zhang, J. Shi, J. Phys. Chem. C. 116 (2012) 15932–15937.

[194] M.K. Sahu, M. Jayasimhadri, J. Lumin. 227 (2020) 117570.

[195] Z. Yang, D. Xu, J. Sun, Opt. Express 25 (2017) A391–A401.

[196] N. Chander, S.K. Sardana, P.K. Parashar, A.F. Khan, S. Chawla, V.K. Komarala, IEEE J. Photovolt. 5 (2015) 1373–1379.

[197] B.P. Kore, A. Kumar, A. Pandey, R.E. Kroon, J.J. Terblans, S.J. Dhoble, H.C. Swart, Inorg. Chem. 56 (2017) 4996–5005.

[198] S. Bishnoi, G. Swati, P. Singh, V. v. Jaiswal, M.K. Sahu, V. Gupta, N. Vijayan, D. Haranath, J. Appl. Crystallogr. 50 (2017) 787–794.

[199] X. Min, Z. Huang, M. Fang, Y. Liu, C. Tang, X. Wu, Inorg. Chem. 53 (2014) 6060–6065.

[200] L. Wang, H.M. Noh, B.K. Moon, S.H. Park, K.H. Kim, J. Shi, J.H. Jeong, J. Phys. Chem. C. 119 (2015) 15517–15525.

[201] Y. Gao, S. Murai, K. Fujita, K. Tanaka, Opt. Mater (Amst.) 86 (2018) 611–616.

[202] K. Jha, M. Jayasimhadri, J. Lumin. 194 (2018) 102–107.

[203] D.L. Dexter, J. Chem. Phys. 21 (1953) 836–850.

[204] Z. Yang, H. Dong, X. Liang, C. Hou, L. Liu, F. Lu, Dalt. Trans. 43 (2014) 11474–11477.

[205] A. Huang, Z. Yang, C. Yu, Z. Chai, J. Qiu, Z. Song, J. Phys. Chem. C. 121 (2017) 5267–5276.

[206] S.G. Menon, A.K. Kunti, D.E. Motaung, H.C. Swart, New J. Chem. 43 (2019) 17446–17456.

[207] G. Annadurai, B. Devakumar, H. Guo, R. Vijayakumar, B. Li, L. Sun, X. Huang, K. Wang, X.W. Sun, RSC Adv. 8 (2018) 23323–23331.

[208] K. Li, H. Lian, R. van Deun, Dalt. Trans. 47 (2018) 2501–2505.

[209] C.S. Kamal, T.K. Visweswara Rao, T. Samuel, P.V.S.S.S.N. Reddy, J.B. Jasinski, Y. Ramakrishna, M.C. Rao, K. Ramachandra Rao, RSC Adv. 7 (2017) 44915–44922.

[210] P. Halappa, A. Mathur, D. Marie-Helene, C. Shivakumara, J. Alloys Compd. 740 (2018) 1086–1098.

[211] R.A. Talewar, S. Mahamuda, K. Swapna, A.S. Rao, J. Alloys Compd. 771 (2019) 980–986.

[212] Z. Xia, S. Miao, M.S. Molokeev, M. Chen, Q. Liu, J. Mater Chem. C 4 (2016) 1336–1344.

[213] H. Tang, X. Zhang, L. Cheng, L. Jiang, X. Mi, Q. Liu, J. Xie, Y. Wang, J. Lumin. 214 (2019) 116532.

[214] B. Ma, X. Ma, T. Xu, K. Su, Q. Zhang, RSC Adv. 8 (2018) 14164–14170.

[215] Q. Li, S. Zhang, W. Lin, W. Li, Y. Li, Z. Mu, F. Wu, Spectrochim. Acta A Mol. 228 (2020) 117755.

[216] J. Brübach, C. Pflitsch, A. Dreizler, B. Atakan, Prog. Energy Combust Sci. 39 (2013) 37–60.

[217] R. Vaz, M.F. Frasco, M.G.F. Sales, Nanoscale Adv. 2 (2020) 5106–5129.

[218] J. Zhou, Q. Liu, W. Feng, Y. Sun, F. Li, Chem. Rev. 115 (2014) 395–465.

[219] J. Zhou, J.L. Leaño, Z. Liu, D. Jin, K.-L. Wong, R.-S. Liu, J.-C.G. Bünzli, Small 14 (2018) 1801882.

[220] C. Zhang, J. Lin, Chem. Soc. Rev. 41 (2012) 7938–7961.

[221] Z. Feng, L. Lin, Z. Wang, Z. Zheng, Opt. Commun. 491 (2021) 126942.

[222] B. Hou, M. Jia, P. Li, G. Liu, Z. Sun, Z. Fu, Inorg. Chem. 58 (2019) 7939–7946.

[223] N. Wang, Z. Fu, Y. Wei, T. Sheng, J. Alloys Compd. 772 (2019) 371–380.

[224] R. Ao, L. Xing, W. Yang, Opt. Commun. 492 (2021) 126967.

[225] D. Chen, Z. Wan, Y. Zhou, X. Zhou, Y. Yu, J. Zhong, M. Ding, Z. Ji, ACS Appl Mater Interfaces. 7 (2015) 19484–19493.

[226] X. Wang, Q. Liu, Y. Bu, C.S. Liu, T. Liu, X. Yan, RSC Adv. 5 (2015) 86219–86236.

[227] A.K. Soni, A. Kumari, V.K. Rai, Sens Actuators B Chem. 216 (2015) 64–71.

[228] E. Cortés-Adasme, M. Vega, I.R. Martin, J. Llanos, RSC Adv. 7 (2017) 46796–46802.

[229] R. Bajaj, M. Gupta, R. Nagarajan, A.S. Rao, G.V. Prakash, Dalt. Trans. 49 (2020) 10058–10068.

[230] M. Jayasimhadri, L.R. Moorthy, K. Kojima, K. Yamamoto, N. Wada, N. Wada, J. Condens. Matter Phys. 17 (2005) 7705.

[231] N. Deopa, A.S. Rao, Opt. Mater (Amst.) 72 (2017) 31–39.

[232] A. Pandey, V.K. Rai, Journal of the Chemical Society. Dalt. Trans. 42 (2013) 11005–11011.

[233] P. Du, L. Luo, X. Huang, J.S. Yu, J. Colloid Interface Sci. 514 (2018) 172–181.

[234] M.A. Antoniak, S.J. Zelewski, R. Oliva, A. Żak, R. Kudrawiec, M. Nyk, ACS Appl Nano Mater. 3 (2020) 4209–4217.

[235] Y. Liu, G. Bai, E. Pan, Y. Hua, L. Chen, S. Xu, J. Alloys Compd. 822 (2020) 153449.

[236] R. Dey, V.K. Rai, Dalt. Trans. 43 (2014) 111–118.

[237] C. Han, J. Tan, A. Xiong, T. Yuan, Opt. Mater (Amst.) 118 (2021) 111232.

[238] R. Wei, J. Guo, K. Li, L. Yang, X. Tian, X. Li, F. Hu, H. Guo, J. Lumin. 216 (2019) 116737.

[239] S. Pradhan, H. Kaur, M. Jayasimhadri, Ceram. Int. 47 (2021) 27694–27701.

[240] Z. Feng, L. Lin, Z. Wang, Z. Zheng, Opt. Commun. 491 (2021) 126942.

[241] R. Shi, L. Ning, Y. Huang, Y. Tao, L. Zheng, Z. Li, H. Liang, ACS Appl Mater Interfaces. 11 (2019) 9691–9695.